On the Large-eddy Simulation of Coupled Flows in Air-Water Systems

By
Santiago López Castaño
Dept. of Engineering & Architecture – DIA

A Dissertation for the partial fulfillment
of the requirements for the degree of
Doctor of Philosophy (PhD)

The University of Trieste
May 2018

Abstract

The objective of this work is to develop an efficient domain decomposition method for the simulation of multiple fluid flows, of interest in geophysical and environmental fluid mechanics, using non-overlapping grids. An explicit sub-structuring domain decomposition method that enforces the compatibility conditions present between non-miscible fluid flows is shown. The current methodology is used for the study of coupled canonical co-current, and counter-current, flows for low *Reynolds* Numbers. Additionally, the study around immersed obstacles in coupled Poiseuille-Couette flows is made.

An incremental-pressure correction method for the numerical integration of the semi-discrete projection dual of the Navier-Stokes equations is implemented, replacing the one implemented originally in the present code [52], LES-COAST. The inclusion of the pressure gradient in the predictor step of the solution method guarantees a higher-order of convergence in the $\mathbf{L}_2$ space, while dispensing of the *deferred-correction* needed at the boundaries for the fluxes in the pressure Poisson equation. For LES modelling, the method explicitly guarantees that inertia should balance with the gradient of pressure in the momentum equation, for sufficiently small time steps, hence the increase in convergence rate.

A large-eddy simulation of a counter-current gas-liquid flow is performed. At the flat interface where the different fluids meet, continuity of momentum and momentum fluxes are enforced following the proposed coupling strategy. The increase in vertical vorticity fluctuations near the interface increases mixing, reducing the thickness of the inner region of the boundary layer. Such increase reduces shear while allowing for more frequent backflow motions in the inner region, being this phenomenon stronger on water. Due to the higher inertia of water these backflow motions are ultimately responsible for the streaky structure of shear stresses seen along the interface. By extracting the motions that are relevant for fluid Reynolds stress coupling [29], such motions reveal a bimodal behavior of streamwise velocities that are only weakly related to its vertical counterparts. The present study shows that such bimodality in the streamwise velocities is also seen in the angle distribution of vorticity relative to the interface, where such angles are linked to the presence of interface-connected and quasi-streamwise vortex cores. Finally, it is shown that backflow events on

the interface shear stresses correlate with *coupled* 'strong' ejections in the near interface region despite the disparagingly different near-interface streamwise velocity distributions on the near interface boundary layers.

The problem of a low-Reynolds number wind-driven Couette flow on water is computed by solving the spatially filtered Navier-Stokes equations, where the flow of the wind is also solved numerically and coupled to the lower shallow whater channel. The unresolved, sub-grid scales are modelled via a *Dynamic* Smagorinsky model. The present work emphasize on the results obtained for the water phase of the system, while for the air phase some first-order statistics are shown. Results of the simulation indicate that the flow in the shallow channel shares some similarities with classical Couette flows, nevertheless the new boundary condition allows for the increase in intermittency of the flow variables and of horizontal turbulent mixing which render a thinner boundary layer near the interface. The now thinner interface boundary layer is more dependent on outer region motions, where inclined vortex structures impinge the near-interface sub-layer. Unlike Couette flows the peak of Reynolds stress is no more at the centreline of the channel, instead the maximum is located on the buffer region of the interface boundary layer breaking the skew-symmetry present in classical Couette flows.

Finally, the influence of a row of circular cylinders immersed in the turbulent boundary layers formed across the interface between two highly stratified, non-miscible fluids is investigated numerically using LES. A co-current Poiseuille-Couette flow is generated on the binary fluid system, and is used as inflow for the current flow study. The interaction between the flows is enforced via the implemented coupling strategy, where each subdomain passes to the other either the kinematic or the dynamic interface conditions. It is found that for low-Re the structure acts partly a modulator of the incoming turbulent structures in the lighter fluid side, while at the heavier fluid side the maxima of TKE are found on the interface. Also, it is shown that the coupling induces an inclination on the near-interface coherent structures generated on the heavier fluid flow.

Acknowledgements

I'd like to thank Prof. Vincenzo Armenio for having let me continue my lifelong educational journey under his supervision, it has been nothing but enriching and positive in all aspects. Both his financial and intellectual support have been critical in my academic development. I also thank the computing time and technical support given by CINECA, and finally thank the fruitful conversations I've had with Dr. Andrea Petronio and Dr. Federico Roman.

Should I haven't met so wonderful people here in Italy, the experience of a PhD must have proven to be extraneous. The friends I have met in Trieste have made the time spent worthwhile. I must thank all of you for the incredible resilience that must imply bearing with me all these years. You know who you are so I'll dispense the reader from a detailed list.

Nothing has been more fulfilling than finding that, at the end of the day, life shouldn't be taken so seriously. At least that I learnt after all these years, and from *Le pètit Prince* of course. In this line of work, it is really easy to succumb to Ego: a false sense of superiority given by the rather arbitrary moral upbringing of graduate studies, and academia in general. Being here has shown me the doors of humility, and *You, Blakas,* helped me reach to the knob. I hope having the courage to open that door.

At last, I think after all these nomad years I will be able to come to my Mother and answer the question she made before I left: 'What will you do next?'

Contents

List of Figures

Chapter 1

Introduction

Liquid-gas interfacial turbulence is a topic of chief interest among researchers in several fields, including those in engineering practice [25]. In this respect, momentum and scalars transport phenomena across gas-liquid interfaces have been the focus of several studies [21, 28, 29, 46] in order to understand the underlying mechanisms of, say, CO_2 sequestration in the ocean, the evolution of a chemical spill patch in a bay or harbor, or the enhancement of surface-renewal motions in lakes that, by corollary, may enhance interfacial mass transfer or mixing in the water column.

Important to the concept of surface-water renewal in lakes and oceans are the results obtained in the pioneering works of [25, 29], where it is argued that the shear rate is the main trigger for the formation of low-speed streaks close to the interface which are maintained by stream-wise vortices formed by inviscid instability mechanisms [19, 41]. Furthermore, the work of Guo and Shen [16] indicates that nonlinear surface waves have a negligible effect on the tilting of stream-wise vortices due to the competing effects of turbulent velocity fluctuations and the wave strain rate.

The increased predictive power of Direct Numerical Simulation (DNS) has shown to be useful for gaining insight on the complex turbulent structures formed closed to the highly-sheared interface, but renders too expensive for complex flow simulations. Despite its importance, modelling of these flows is limited due to the heightened (compared to one-phase DNS) demands on computational resources and complexity on the topological/geometrical features in flows of engineering interest. Thus, most Direct Numerical Simulations or RANS/LES simulations have been confined in the resolution of one of the phases while parametrizing the other phase as a boundary condition. In the case of flows in the ocean, using prescribed sea-surface motions from inviscid water wave theory has proven to be useful as long as low air-sea interactions are expected; also in an attempt to obtain more realistic wave representations, the so-called Large-Wave Simulation (LWS) described by Dimas and Fialkowski [10]

has proven efficient in modelling the effects of non-breaking waves in the long wavenumber regime. Yet other researchers [22, 25, 46] opted to parametrize the effect of wind as a constant shear over one of the boundaries in an attempt to interpret its mean effects; a great body of literature has been made upon this approach. Incidentally, several of the so-called hydrostatic (or shallow-water) ocean models parametrize air-sea interaction in an attempt to reproduce its effects over the liquid phase either by enforcing the dynamic condition (continuity of normal stresses and pressure) or the no-slip condition (a prescribed wind velocity according to some correlation law) over the upper rigid surface.

More recently, three-dimensional Large-eddy Simulations are being carried out to study complex geophysical flows where one of the boundaries uses a parametrization of the effect of either the ocean or the atmosphere. For instance, in the case of offshore wind farm engineering, Yang et al. [50] parametrized the gas-liquid interaction by modelling the wave motion via non-linear wave theory model, and using a wall model for the stresses transferred from the interface. Also, Sullivan et al. [42] performed wind-wave, high-resolution LES to investigate near-wave interaction of the turbulent field on the atmosphere, they found that long surface waves on the atmosphere bottom boundary produce a low-level jet that reduces shear over the apparent wall. Moreover, the work of Liu et al. [28] reported that despite the fact that the features of the boundary layer formed by the coupled interaction between atmosphere and ocean resembles that of a wall for the air side, the near-interface coherent structures are still controlled by water motions which, in turn, are responsible for scalar mixing and interfacial transport across the interface. In fact, Komori et al. [21, 22] concluded that the main mechanisms of scalar transfer across a highly stratified interface are the streamwise vortical structures related to the bursting motions on the denser fluid. Thus the overall impact of disregarding this complex interplay of mass transport and liquid-side coherent phenomena lead to a possible misinterpretation of, say, local heat fluxes across the gas-liquid interface. To the authors' knowledge, no LES involving a air-sea, two-way coupling has been performed for configurations different from those related to horizontally-periodic channels; thus by incorporating simple geometries which render complex turbulent structures and scalar transport processes, yet generic enough to be of engineering interest, could elucidate complex mechanisms that otherwise would be absent using parametrized models.

Apart from the aforementiones studies about boundary-layer flows over sheared interfaces, the rapid increase in demand of offshore wind-generated power promises to affect considerably the atmospheric flow on large scales due in part to the increased roughness caused by offshore and continental wind farms, which demands for high-resolution simulations for its study. Unfortunately, little is known on the air-ocean dynamics of flows around obstacles

crossing the interface between the systems. On this respect, recent works [37, 47, 50] on large-eddy simulation of wind farms and its interaction with the Atmospheric Boundary Layer (ABL) has provided important information regarding the optimization of turbine arrangement for energy production, and its consequences in the wind-power meteorology. In particular, these studies show important discrepancies in the momentum fluxes and turbulent kinetic energy with respect to the undisturbed ABL, which are a strong function of the farm layout. Although it is mentioned, not much was dedicated on studying the effect that these farms have on the ABL, particularly on the extent on which it perturbs the flow or on how the down-wash of the wake could potentially affect the upper atmosphere. Incidentally, much of the work in LES has been dedicated on the validation of wind-farm parametrization models (WFM) for arrays of wind turbines, either on land or in the ocean considering the lower boundary as a no-slip wall, where the subtleties given by these high-resolution models are qualitatively analyzed. Such high-resolution models do not resolve directly the effect of rough surfaces but parametrize them via wall models according to some reference roughness height. Among this lines, the work of Barthelemie et al. [4] shows that no particular WFM has superior predictability over the velocity deficit seen in the wake of wind farms, instead, numerical results obtained with these models do not compare well within each other. B. and W. [3] noticed that not accounting for isolated- and arrayed roughness elements in Global Climate Models (GCM) under-predicts momentum mixing in the ABL, having profound effects in large-scale tropospheric winds and, disparagingly enough, on local temperature fluxes. Thus, it concluded that the addition of surface roughness via isolated roughness elements modeled as momentum sinks imposed in the solution of the background wind lead to wind anomalies associated with wave patterns of convergence and divergence in the local scale that ultimately affects large-scale wind patterns. However, no clear distinction is made between roughness elements located offshore or in continental land nor of its interaction with the initially undisturbed ABL. Additionally, the experiments of Castro et al. [8] of ABL flow over urban canopies show that a significant amount of scatter in the mean velocity and turbulent stress profiles is present and extends vertically up to 1.8 times the height of the canopy in a neutrally stable ABL. In the same work, a comparison with the canopy model of MacDonald [31] shows a notable discrepancy respect to the aforementioned experimental results.

Various studies [8, 35, 39, 45] have sought to understand the interplay of roughness elements immersed in the boundary layer over smooth surfaces, with its effects on the coherent motions of the undisturbed flow. Surface mounted obstacles immersed within the log-layer in otherwise undisturbed boundary layer flows disrupt the self-sustaining turbulence cycle present in wall-bounded turbulence. This disruption, depending on geometrical and spatial

arrangement of the obstructing elements, may increase or decrease drag as a consequence. Many of these works report that the perturbation caused by these roughness do not extend vertically to the wake region of the boundary layer, but deficits in both velocity and turbulent kinetic energy profiles are sought as far as 10 times the effective diameter of the protruding characteristic element in the streamwise direction. Particularly, time frequency spectra for isolated elements show no particular dominant frequency behind the elements thus indicating that the local lenght- and time-scales of the flow behind the obstacle can be still given by the incoming, undisturbed flow structures; these structures, nevertheless, are reduced in size when passing behind the cylinder. These studies suggest that neither Kàrmàn shedding nor tip-vortex shedding play an important role in the evolution of boundary-layer flow around isolated, finite cylinders. On the other hand, root-mean-square measurements of streamwise velocities and pre-multiplied energy spectra downstream of the obstacles show an increase in near-wall behavior that might imply that horseshoe vortices do play a role in wake interaction between obstacle arrays. Furthermore it was found that perturbations, for densely-packed obstacles and urban canopies immersed within the log-layer, scale with the height of the roughness elements; by contrast for sparsely packed and isolated elements it was found that inner turbulent structures scale well with the effective diameter of the obstacle.

The numerical techniques herein used, namely, the Navier-Stokes solution method [52], and the treatment of complex boundary conditions [38] have been studied and used extensively for quite a long time. Nevertheless, in the cases of interest in this particular work a more precise account of the dynamic pressure is important for the accurate imposition of the kinematic and dynamic constraints set by the interface between two non-miscible fluid flows. The current projection method reduces the order of approximation of the pressure term to $\mathcal{O}(\Delta x, \Delta y)$, which can be corrected enforcing a second-order time projection of the pressure as well.

The objectives of the present dissertation are to: (1) The study of highly stratified non-miscible canonical and/or geophysical flows, (2) and the study of flows around immersed arrays of obstacles in coupled air-water systems.

1.1 Summary

For the fulfilling of the aforementioned objectives, the following items were conducted as part of the current research:

1. To improve the current Navier-Stokes equation solution algorithm for a more precise account of pressure and associated boundary conditions.

2. The development of a non-iterative sub-structuring technique for multi-domain, and multi-physics, simulations focused on the solution of non-miscible sheared fluid flows across interfaces.

3. The physics of interface-sheared boundary layers are revisited under the current framework using subgrid-scale models. The degree of turbulence coupling and increased mixing are studied.

4. The physics of sheared, non-miscible gas-liquid boundary layers around immersed obstacles are investigated.

Chapter 2

Navier-Stokes Solver

Our objective in this chapter is to design an efficient and accurate improvement of the algorithm proposed by Zang et al. [52], with the addition of the appropriate modifications for the solution of coupled, highly-stratified flows. Therefore, this chapter is comprised of three main parts: (1) mathematical description of the governing equations for a single fluid and compatibility conditions for the treatment of coupled flows, (2) a discrete approximation of the aforementioned items, and (3) the validation of the *incremental-pressure* projection and coupling algorithms. However, it is not the objective of this chapter to make a rigorous description of the discrete approximation of the governing equations nor of the coupling strategy or the mathematics within, since these are well described in literature [29, 44, 52]; rather, an intuitive reasoning for the modifications will be presented.

On the first part of this chapter, a general description of the governing equations of fluid motion and jump conditions for treating coupled flows are given. Then, the second part aims to give a description of the semi-discrete system of equations obtained via *incremental-pressure* projection which are amenable for numerical computations. Furthermore, an algebraic representation of the finite-difference system is briefly described, and the solution algorithm is proposed. Finally, the last part presents a validation for the proposed coupling algorithm. Note that for the validation we will limit ourselves to the solution of laminar flows in the case of the coupled solver, an appropriate validation for turbulent flows will be done in Chapter 3. Finally, the equations herein shown will be written in either vector or indicial form, depending on which offers more clarity in the exposition.

2.1 Governing Equations

The conservative form of the governing equations for incompressible, laminar flow of liquids and gases can be written in index $(i, j, k = 1, 2, 3)$ notation as follows:

$$\frac{\partial u_j}{\partial t} + \frac{\partial (u_j u_i)}{\partial x_i} = -\frac{1}{\rho}\frac{\partial P}{\partial x_j} + \nu \frac{\partial^2 u_j}{\partial x_k \partial x_k} + f_j \tag{2.1}$$
$$\frac{\partial u_j}{\partial x_j} = 0$$

Where u_i, P, and f_i correspond to a velocity component, dynamic pressure ($= \rho U^2 Lp$), and a body force component, respectively; the parameters ρ and ν are the density and the kinematic viscosity. These equations represent an accurate continuum model for the flow of Newtonian fluids and are named the Navier-Stokes equations (NSE). Note that one can also normalize equations 2.1, using the following characteristic scales $(U, L, \nu/L^2)$, and obtain the following system:

$$\frac{\partial u_j}{\partial t} + \frac{\partial (u_j u_i)}{\partial x_i} = -\frac{\partial \tilde{p}}{\partial x_j} + \frac{1}{Re}\frac{\partial^2 u_j}{\partial x_i \partial x_i} + \frac{1}{Fr^2}\tilde{f}_j \tag{2.2}$$
$$\frac{\partial u_j}{\partial x_j} = 0$$

Where Re is the *Reynolds Number*, $\tilde{p}$ is the kinematic pressure, $\tilde{f}_j$ a scaled bodyforce, and $Fr^2 = U/(\sqrt{f_k f_k} L)$. In the bodyforce term, the effects of buoyancy, Langmuir circulations, and rotation can be lumped. In addition, one could also consider the case where an active/passive scalar is present. In the latter case, an additional transport equation must be solved:

$$\frac{\partial C}{\partial t} + u_j \frac{\partial C}{\partial x_j} = \frac{1}{Re\, Sc}\frac{\partial^2 C}{\partial x_j \partial x_j} \tag{2.3}$$

Where C represents the scalar being transported, and Sc represents the ratio between the viscous time scales of the fluid and the diffusion of the scalar; such ratio bears the name of *Schmidt* Number in the case of gas transfer, and in the case of heat transfer is known as the *Prandtl* Number, Pr.

2.1.1 Interface conditions and solution of coupled flow

The normalized jump conditions for equations 2.2 for a flat interface are expressed as follow:

$$\frac{1}{Re}\left((\tau_{liquid} - \tau_{gas}) \cdot \mathbf{n}\right) \cdot \mathbf{n} + p_{gas} - p_{liquid} = 0 \tag{2.4}$$

$$u_{gas} = \frac{1}{\mathcal{R}} u_{liquid} \tag{2.5}$$

$$\mathcal{R} = \sqrt{\frac{\rho_{liquid}}{\rho_{gas}}} \tag{2.6}$$

Where τ is the normalized stress tensor on either side of the interface, $\mathbf{n}$ the face normal vector to the interface, ρ density, and p the pressure on either side of the interface. On the other hand, the jump conditions for equation 2.3 are:

$$\left.\frac{\partial C}{\partial \mathbf{n}}\right|_{gas} = -\alpha \frac{Sc_{gas} Re_{gas}}{Sc_{liquid} Re_{liquid}} \frac{1}{\mathcal{R}} \left.\frac{\partial C}{\partial \mathbf{n}}\right|_{liquid} \tag{2.7}$$

$$C_{gas} = C_{liquid} \tag{2.8}$$

The only new parameter is α, and its exact definition varies according to the properties of the scalars being studied. For instance, in the case of gas transfer, this term is known as the *Ostwald solubility ratio.*

2.2 Semi-discrete Governing equations: Projection Methods

A semi-implicit, time-discrete, first-order accurate in time form of the governing equations 2.1 can be written as:

$$\frac{\mathbf{u}^{n+1} - \mathbf{u}^n}{\Delta t} + \nabla P^{n+1/2} = -[\nabla \cdot (\mathbf{uu})]^{n+1/2} + \frac{\nu}{2} \Delta(\mathbf{u}^{n+1} + \mathbf{u}^n) \tag{2.9}$$

$$\nabla \cdot \mathbf{u}^{n+1} = 0 \tag{2.10}$$

with the boundary conditions

$$\mathbf{u}^{n+1}|_{\partial\Omega} = \mathbf{u}_b^{n+1}$$

The spatial discretization of the system of equations just shown is not ideal to solve directly since equation 2.10 is more a kinematic constraint imposed on the resulting vector field, additionally neither the governing equations nor the theory of incompressible flows offer an independent equation for P. Thus, by the use of the projection method pioneered by Yanenko [49] the numerical integration of equations 2.1 can be achieved: it is based on a simple use of the Hodge decomposition theorem in which the non-divergent (or rotational) part of equations 2.1 is written as:

$$\mathbf{u}_t = \mathbf{P}\left[-\nabla \cdot (\mathbf{uu}) + \nu \Delta \mathbf{u}\right] \tag{2.11}$$

Where $\mathbf{P}$ is an application that projects the vector field onto a non-divergent space, with the appropriate boundary conditions. Notice that in equation 2.11 no assumption on the

time-discretization of equation 2.9 is considered, in order to stress the continuous character of the decomposition.

2.2.1 A pressure-increment projection method

Using equation 2.11 as a starting point, a fractional step procedure can be used to approximate the governing equations, by disregarding the incompressibility constraint when solving the momentum equation and then correcting the otherwise rotational velocity field by projecting it over a divergence-free space. In other words:

(1) Solve for an intermediate field $\mathbf{u}^*$

$$\frac{\mathbf{u}^* - \mathbf{u}^n}{\Delta t} + \nabla \tilde{P} = -[\nabla \cdot (\mathbf{uu})]^{n+1/2} + \frac{\nu}{2} \Delta(\mathbf{u}^* + \mathbf{u}^n) \tag{2.12}$$

$$BC(u^*) = 0 \tag{2.13}$$

Where $\tilde{P}$ and $BC(u^*)$ are approximations made on the pressure and on the boundary condition for the *intermediate velocity* u^*, respectively. Depending on how these approximations are made, different families of fractional step algorithms are obtained.

(2) Project the rotational vector field

$$\mathbf{u}^* = \mathbf{u}^{n+1} + \Delta t \, \nabla \phi^{n+1} \tag{2.14}$$

$$\nabla \cdot \mathbf{u}^{n+1} = 0 \tag{2.15}$$

And, again, using boundary conditions consistent with $\mathbf{u}^*$ and $\mathbf{u}_b$.

(3) Update the pressure

$$P^{n+1/2} = \tilde{P} + \mathcal{F}(\phi^{n+1})$$

where $\mathcal{F}$ is some function relating P and ϕ.

An expression for $\mathcal{F}$ can be obtained by combining equations 2.12 and 2.14, and then comparing it with equation 2.9. From this observation:

$$\frac{\mathbf{u}^{n+1} - \mathbf{u}^n}{\Delta t} + \nabla \left(\tilde{P} + \phi^{n+1} - \frac{\Delta t}{2} \Delta \phi^{n+1} \right) = -[\nabla \cdot (\mathbf{uu})]^{n+1/2} + \frac{\nu}{2} \Delta(\mathbf{u}^{n+1} + \mathbf{u}^n)$$

It is obvious that:

$$P^{n+1/2} = \tilde{P} + \phi^{n+1} - \frac{\Delta t}{2} \Delta \phi^{n+1} \tag{2.16}$$

The method proposed in the seminal paper of Chorin [9], that serves as base for the algorithm in Zang et al. [52] and implemented in the current code, considers $\tilde{P} = 0$. This approximation however, by direct consequence of equation 2.14, complicates the definition of an appropriate boundary condition for the intermediate velocity $\mathbf{u}^*$ since ϕ^{n+1} is not known by the time the boundary conditions need to be updated. Thus, the solution may degrade at the boundaries whenever the intermediate velocity differs significantly from the velocity itself.

A more consistent treatment of the pressure and intermediate velocities at the boundaries can be achieved [7, 15] if an extrapolation on the "intermediate" pressure is made:

$$\tilde{P} = P^{n-1/2} + \phi^n$$

Consequently, the corrector step 2.14 becomes:

$$\mathbf{u}^* = \mathbf{u}^{n+1} - \frac{1}{2}\Delta t \, \nabla(\phi^{n+1} - \phi^n)$$

And the pressure update is:

$$P^{n+1/2} = P^{n-1/2} + \phi^{n+1}$$

With this approximation it is clear that the use of the corrector step over the boundaries will yield an intermediate velocity that will not differ much from the velocity itself, thus a boundary condition $BC(\mathbf{u}^*) = (\mathbf{u} - \mathbf{u}^*)|_{\partial\Omega} = 0$ can be easily written. It can be demonstrated [7, 13, 15, 44] that under the L-2 norm a higher order of convergence on the velocity and pressure are obtained, compared to the current non-incremental projection.

Boundary Conditions for Pressure

When applying the incompressibility constraint over the corrector step 2.14 one can come up with an expression for the pressure, namely:

$$\frac{1}{2}\Delta t \; \Delta(\phi^{n+1} - \phi^n) = -\nabla \cdot \mathbf{u}^*$$

The laplace operator, in order to be solved numerically, requires the specification of boundary conditions for $\delta\phi$. Although the necessary boundary conditions for the poisson operator have been analyzed [13, 14, 44] and proposed in order to guarantee regularity of the numerical solution at all times, there still seem to be some confusion on how these boundary conditions should be interpreted. In general, the poisson equation for pressure is an equation derived from the momentum equation, and as such its boundary conditions should be derived from it as to guarantee the well-posedness of the system at all times; this is due to the fact that pressure is more of a mathematical artifice (lagrange multiplier in

optimization problems) in incompressible flows, but interestingly enough its gradient has a physical interpretation: that of a bodyforce. In general, a Neumann problem for the pressure at the boundary with face-normal $\mathbf{n}$ has to be enforced in the poisson equation:

$$\mathbf{n} \cdot \nabla\phi = \nu \, \Delta \mathbf{u}_n - (\mathbf{u}_t + \mathbf{u} \cdot \nabla \mathbf{u}_n)$$

Thus, we can make the following claim:

$$\mathbf{n} \cdot \nabla(\phi^{n+1} - \phi^n) \approx 0$$

Where $\delta\phi = \phi^{n+1} - \phi^n$ is the appropriate term for which the gradient is calculated in the corrector step. It is important to note that this constraint only applies when solving the poisson equation: boundary conditions for the gradient of pressure on the predictor step do not fall into this characterization.

2.2.2 LES Framework

The governing equations for just presented are unsuited for the simulation of *high-Reynolds* number flows over complex domains since is too computationally demanding to resolve all energy-containing events on such flows. Instead, a form of these equations can be obtained in which the high-wavenumber signals are smoothed out using a low-pass filter. Thus, by using such filter on equations 2.1, the corresponding non-dimensional space-filtered governing equations are, in coordinate-free form:

$$\overline{\mathbf{u}}_t - \frac{1}{Re}\Delta\overline{\mathbf{u}} + \nabla \cdot (\overline{\mathbf{u}}\,\overline{\mathbf{u}}) + \nabla\overline{p} + \nabla \cdot (\overline{\mathbf{u}\mathbf{u}} - \overline{\mathbf{u}}\,\overline{\mathbf{u}}) = \frac{1}{Fr^2}\overline{\mathbf{f}} \tag{2.17}$$

$$\nabla \cdot \overline{\mathbf{u}} = 0 \tag{2.18}$$

In which the only physically relevant parameter for describing turbulence is the *Reynolds number*, $Re = UL/\nu$, where U and L are the relevant velocity and length scales, respectively. Also, the operator $\overline{(\cdot)}$ denotes the space convolution using some filter, which forms the core of what is known as *Large Eddy Simulation*, or LES [40].

Modeling of subgrid-scale (SGS) terms: Dynamic Smagorinsky model

The system given by equation 2.17 is underdetermined: a mathematical formulation for the SGS term $\tau_{\text{sgs}} = \overline{\mathbf{u}\mathbf{u}} - \overline{\mathbf{u}}\,\overline{\mathbf{u}}$ is sought in order to close it. The Smagorinsky model [40] proposes the use of Boussinesq's analogy of eddy viscosity, thus making the assumption that production and dissipation of turbulent kinetic energy balance each other at the "small" scales of turbulent fluctuations. This yields:

$$\tau_{\text{sgs}} = -2\nu_{\text{sgs}}\overline{\mathbf{S}} \tag{2.19}$$

$$\nu_{\text{sgs}} = (C_s\overline{\Delta})^2|\overline{\mathbf{S}}| \tag{2.20}$$

Where $|\overline{\mathbf{S}}| = (\overline{\mathbf{S}} : \overline{\mathbf{S}})^{1/2}$, and the strain-rate tensor $\mathbf{S}$ is defined as the symmetric part of the velocity gradient tensor $\nabla\mathbf{u}$. Also, the term C_s is often referred as the Smagorinsky constant, and $\overline{\Delta}$ is the filter width. This model, as it stands, is too dissipative in the turbulent transition regime and does not allow for energy transfer from smaller-to-bigger events on the flow. The former drawback can be overcome by introducing a space-time dependence on the Smagorinsky constant, $C_s = C_s(\mathbf{x}, t)$. The Dynamic Smagorinsky Model proposed by Germano et al. [40] filters again the flow field using a larger filter width, commonly defined as $\widehat{\overline{\Delta}} = 2\overline{\Delta}$, in order to come with an expression for C_s. In principle, one can solve in a least-square sense the overdetermined system for C_s on the test grid and the original system yielding an "optimal" C_s. However, by assuming that the SGS Reynolds stress tensor has the same orthonormal basis with the strain-rate tensor the "optimization" problem can be skipped. Furthermore, information provided by these two filters are valid as long as statistical self-similarity can be assumed true in the inertial range of the turbulent spectrum. Finally, the use of the second filter and the aforementioned assumptions yields:

$$C_d = \frac{(\alpha - \widehat{\beta}) : \mathbf{L}^d}{(\alpha - \widehat{\beta}) : (\alpha - \widehat{\beta})} \tag{2.21}$$

Where

$$\mathbf{L} = \widehat{\overline{\mathbf{u}}\overline{\mathbf{u}}} - \widehat{\overline{\mathbf{u}}}\,\widehat{\overline{\mathbf{u}}} \tag{2.22}$$

$$\alpha = -2\widehat{\overline{\Delta}}^2|\widehat{\overline{\mathbf{S}}}|\widehat{\overline{\mathbf{S}}} \tag{2.23}$$

$$\beta = -2\overline{\Delta}^2|\overline{\mathbf{S}}|\overline{\mathbf{S}} \tag{2.24}$$

The superscript d denotes the deviatoric part of the tensor, and the symbol $\widehat{(\cdot)}$ denotes the application of the second filter. In the current framework, a box filter is used, since it can be easily implemented under the Finite-Difference/Volume framework.

Subgrid-scale fluxes for scalar transport equation

By filtering the transport equation 2.3, one gets the following:

$$\frac{\partial C}{\partial t} + u_j\frac{\partial C}{\partial x_j} = \frac{1}{Re\ Sc}\frac{\partial^2 C}{\partial x_j \partial x_j} - \frac{\partial \eta_j}{\partial x_j} \tag{2.25}$$

In which, analogously to the eddy-viscosity assumption made for the equations of motions, the SGS fluxes for the turbulent scalar diffusivity are written as follows:

$$\eta_j = -\frac{\nu_{\text{sgs}}}{Sc_{\text{sgs}}}\frac{\partial C}{\partial x_j} \tag{2.26}$$

The turbulent diffusivity length Sc_{sgs}, as in the case of fluid motion, can be either set constant or calculated dynamically. The dynamic procedure of Armenio and Sarkar [2] is implemented in the present code.

2.2.3 Numerical Approximation of the Navier-Stokes equations

The numerical integration used in this work extends that of Zang et al. [52] where the governing equations are expressed in a generalized coordinate form, by including the adjustments proposed in section 2.2.1 and the coupling strategy that will be described in 2.2.4. To write the algebraic form of the momentum equation, the convective and the off-diagonal components of the viscous term are split using a second-order Adams-Bashford algorithm, whereas the diagonal components of the viscous term are integrated using a Crank-Nicolson scheme. An ADI factorization is used on the right-hand-side discrete implicit predictor term in order to yield a tridiagonal matrix system. Finally, to guarantee a coupling between pressure and velocity a projection of the fluxes over the cell faces is done and used for the poisson solver for pressure. The individual terms of the discrete momentum equation in indicial form are the following:

$$D_\alpha(\cdot) = \frac{\Delta t}{2|J|^{-1}}\frac{\delta}{\delta\xi_\alpha}\left[\nu|J|^{-1}G^{\alpha\alpha}\frac{\delta}{\delta\xi^\alpha}(\cdot)\right] \tag{2.27}$$

$$D_E(\cdot) = \frac{\delta}{\delta\xi_\alpha}\left[\nu|J|^{-1}G^{\alpha\beta}\frac{\delta}{\delta\xi^\beta}(\cdot)\right]_{\alpha\neq\beta} \tag{2.28}$$

$$D_I(\cdot) = \frac{\delta}{\delta\xi_\alpha}\left[\nu|J|^{-1}G^{\alpha\beta}\frac{\delta}{\delta\xi^\beta}(\cdot)\right]_{\alpha=\beta} \tag{2.29}$$

$$B_i(\cdot) = -\frac{\delta}{\delta\xi_\alpha}\left[|J|^{-1}\frac{\delta\xi_\alpha}{\delta x_i}(\cdot)\right] \tag{2.30}$$

$$C_i = -\frac{\delta}{\delta\xi_\alpha}\left[|J|^{-1}U^\alpha u_i\right] \tag{2.31}$$

The indices in greek letters are taken as summation indices, whereas the lowercase latin letters mean free indices. The physical variables u_i, U^q, and ν are the velocities at the control-volume centroids, the momentum flux defined on the control-volume faces ($= [\delta\xi_\alpha/\delta x_i]\widetilde{u}_i$), and viscosity, respectively. The geometrical variables J, G^{ij}, ξ_i, and x_q are the transformation Jacobian ($= \delta x_i/\delta\xi_q$), mesh skewness tensor ($= [\delta\xi_i/\delta x_\alpha]\,\delta\xi_q/\delta x_\alpha$), the local coordinate

system ($= \xi_i(x_j)$), and the physical coordinate system, respectively. The spatially discrete representation of the fractional step method described earlier is as follows:

- Predictor Step:

$$\left(I - \frac{\Delta t}{2|J|^{-1}} D_I^{n+1}\right)(u_i^* - u_i) = F_i$$

An ADI factorization leads to:

$$(I - D_1^{n+1})(I - D_2^{n+1})(I - D_3^{n+1})(u_i^* - u_i) = F_i \tag{2.32}$$

Where the source term is:

$$F_i = \frac{\Delta t}{|J|^{-1}} \left\{ \frac{3}{2}[C_i^n + D_E(u_i^n)] - \frac{1}{2}[C_i^{n-1} + D_E(u_i^{n-1})] + D_I(u_i^n) + B_i(P^n) \right\}$$

- Pressure-Poisson equation:

$$\frac{\delta}{\delta \xi_\alpha}\left[|J|^{-1} G^{\alpha\beta} \frac{\delta(\delta P^{n+1})}{\delta \xi^\beta}\right] = \frac{|J|^{-1}}{2\,\Delta t} \frac{\delta U_\alpha^*}{\delta \xi_\alpha} \tag{2.33}$$

$$U_\alpha^* = [\delta \xi_\alpha / \delta x_i]\widetilde{u^*}_i \tag{2.34}$$

Where the tilde denotes interpolation. A major difference of the present algorithm with that of Zang et al. [52] is the calculation of the *pressure increment* δP instead of the so-called *computational pressure* ϕ; notice that the arrangement of variables related to pressure are slightly different from those shown in section 2.2.1, but is nonetheless equivalent. Thus:

$$P^{n+1} = P^n + \delta P^{n+1} \tag{2.35}$$

- Corrector steps:

  (a) for the velocities at the centroids:

$$u_i^{n+1} = u_i^* + \frac{\Delta t}{2\,|J|^{-1}} B_i(\delta P^{n+1}) \tag{2.36}$$

  (b) for the momentum fluxes:

$$U_i^{n+1} = U_i^* + \frac{\Delta t}{2}\left[G^{i\alpha} \frac{\delta(\delta P^{n+1})}{\delta \xi_\alpha}\right] \tag{2.37}$$

Solution Procedure

To summarize, the numerical integration of the governing flow equations follow the steps described below:

1. Update boundary conditions for the primitive variables u_i, P. When the solid boundaries are complex, when required, an *Immersed Boundary* technique described in Roman et al. [38] is used.

2. Calculate the intermediate velocity u_i^* at the cell centers using equation 2.32; in which the coefficients of the resulting linear system $A\,\mathbf{x} = \mathbf{b}$ form a tridiagonal matrix.

3. Calculate the right hand side of equation 2.33 by interpolating the intermediate velocities as described in equation 2.34.

4. Solve equation 2.33. In the current work, an algebraic V-Multigrid solver is used.

5. Calculate u_i^{n+1} and U_i^{n+1} using equations 2.36 and 2.37. Additionally, calculate P^{n+1} using equation 2.35 to finish one time step.

For the sake of brevity, the validation of this algorithm is put forth in Appendix A, where the study on turbulent flows using the LES model just described is made on some benchmark cases.

2.2.4 Gas-liquid coupling Strategy

A so-called fractional-step coupling strategy [29] is implemented in order to satisfy, up to first order in time, the momentum and mass continuity at the two-fluid flow interface. This procedure is roughly equivalent to what it is known in DDM community as a non-iterative substructuring method, which simply and exclusively imposes either the Dirichlet (velocity) or Neumann (momentum flux) at each respective interface over two disjoint domains. This method, although unstable, poses great ease in the implementation and is not as CPU demanding as other, more accurate, methods. Also, due to the characteristics of the method itself, it is a more natural approach when it comes to the study of air-sea interface interactions where it is assumed that the gas side imposes the boundary momentum fluxes (shear stresses) while the liquid side imposes the boundary velocity to the gas side in the near region of the interface.

The proposed coupling (or interface enforcing condition) procedure is as follows:

1. At a certain time step, the flow field is solved for one of the subdomains (in this case, the gas side) and the interface momentum fluxes (stresses) are stored, as shown in equation 2.4.

2. At the same time step, use the already stored boundary stresses as non-homogeneous Neumann boundary condition at the interface for the opposing subdomain (in this case, the liquid side) and solve the flow field. With the newly calculated field, extract and store the interface velocities as described in equation 2.6.

3. At the following time step, use the calculated interface velocity from step (2) to solve the flow field in the gas subdomain.

4. Repeat (1).

For the typical scenarios modeled using LES-COAST, mass and face normal momentum transfer across the interface can be considered negligible due to the high stratification between the comprising fluids. This reduces the local constraints in mass and momentum conservation across the interface.

Although it is tempting to argue that the corrector step is not needed at the interface when running simulations with negligible convective accelerations, given the implementation nature of the governing differential equations [52], a computational pressure term is always present at the ghost cells beyond the physical boundaries which imposes the need of the pressure corrector in order to guarantee zero divergence of the intermediate fluxes of momentum.

2.3 Validation Results

For each of the cases shown in this section a comparison between numerical results and analytic solutions is made, when the latter is available. Thus, every subsection contains the simplified governing equations and its corresponding analytic solution and these are contrasted with the results obtained numerically. Also, only unconditionally stable shear flows are considered for the validation of the coupling.

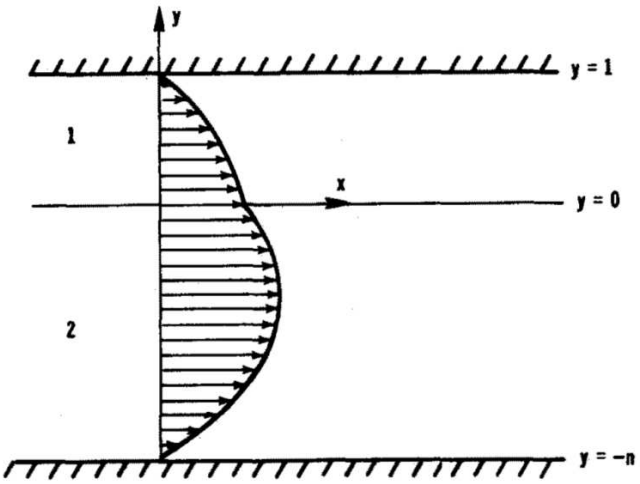

Figure 2.1: Velocity profile for two superposed plane poiseuille flows. Taken from [51].

2.3.1 Co-current plane laminar Flow induced by a body force

The time evolution equations of the flow between two stably stratified fluids ($k = 1, 2$) subjected to a horizontal reference body force are written as:

$$\begin{cases} \dfrac{\partial u_j^k}{\partial t} = \nu \dfrac{\partial^2 u_j^k}{\partial x_i^k \partial x_i^k} \delta_{3\,i}^{j\,1} + \delta_1^j f_j^k & \text{in } \Omega^k \\ \dfrac{\partial u_i^k}{\partial x_j^k} \delta_1^j = 0 & \text{in } \Omega^k \\ (u_j^2)_\Gamma = (u_j^1)_\Gamma & \text{in } \partial\Omega^1 \cap \partial\Omega^2 = \Gamma \\ \left(\nu^2 \dfrac{\partial u_i^2}{\partial x_j^2}\right)_\Gamma \delta_{3\,i}^{j\,1} = \left(\nu^1 \dfrac{\partial u_i^1}{\partial x_j^2}\right)_\Gamma \delta_{3\,i}^{j\,1} & \text{in } \partial\Omega^1 \cap \partial\Omega^2 = \Gamma \end{cases} \tag{2.38}$$

Where it has been assumed that the horizontal body force f_j runs parallel to one of the horizontal axes. Notice that the presence of a constant body force in a Poiseuille-type flow has the same effect of having a constant pressure gradient and makes the flow independent of the density stratification, as long as the body force is equal in both fluids. Note that the convective acceleration is not present in our formulation; due to mass conservation, this term disappears identically.

The analytical solution of the time independent Poiseuille flow of two superposed fluids, sketched in figure 2.1, can be expressed as follows :

$$\begin{cases} U_1 = U_\Gamma + \dfrac{A}{\nu_1} y - \dfrac{1}{2}\dfrac{\mathcal{F}}{\nu_1} y^2 \\ U_2 = U_\Gamma + \dfrac{A}{\nu_2} y - \dfrac{1}{2}\dfrac{\mathcal{F}}{\nu_2} y^2 \\ U_\Gamma = \dfrac{1}{2} H^2 \mathcal{F} \dfrac{f(1-f)}{\nu_1(1-f) + \nu_2 f} \\ A = \dfrac{1}{2} H \mathcal{F} \dfrac{\nu_1(1-f)^2 - \nu_2 f^2}{\nu_1(1-f) + \nu_2 f} \end{cases} \tag{2.39}$$

Where the variables correspond to those usual in fluid dynamics: u for horizontal velocity, f for vertical phase fraction (h/H), interfacial velocity U_Γ, $\mathcal{F}$ for the bodyforce, and kinematic viscosity ν. Please note that equations 2.39 can also be made valid in the case of superposed plane Poiseuille and Couette flow, just by dropping the second order polynomial in either of the phases and interchanging kinematic viscosity by the dynamic viscosity.

As mentioned earlier, density stratification does not play a role in superposed plane Poiseuille flows (see equation 2.38) and only the kinematic viscosity plays a differentiating role between the phases when it comes to express the analytic solution. On the other hand, density stratification does play a role when superposed Couette/Poiseuille flows are being modelled since the forcing for one of the flows is a momentum flux. This complicates the search for a universal set of non-dimensional parameters related to the friction velocity, that are valid for these kinds of flows. Note that the common kinematic variable characteristic of the superposed flows is the *interfacial velocity*, U_Γ. Given the formulation of the problem at hand, the scaling parameter chosen is the *interfacial Reynolds Number*, defined as:

$$\mathbf{Re} = \frac{U_\Gamma \, h}{\nu} \tag{2.40}$$

Co-current plane Poiseuille/Couette Flow induced by a body force

The geometry selected for this case is the same to the one picked in section 2.3.1. A high density stratification was chosen ($\rho_1/\rho_2 = 1000$) and different interfacial Reynolds Number was chosen in order to test for bugs in the code. As reported earlier, the error reduction over successively refined grids is of order $p \approxeq 1$ near the interface boundary. Numerical instability appears when the density ratio is close to 1; a result expected in lieu of the theory of linear stability of Kelvin-Helmholtz waves. The solution for a grid partitioned in 32^3 elements is shown in figure 2.2.

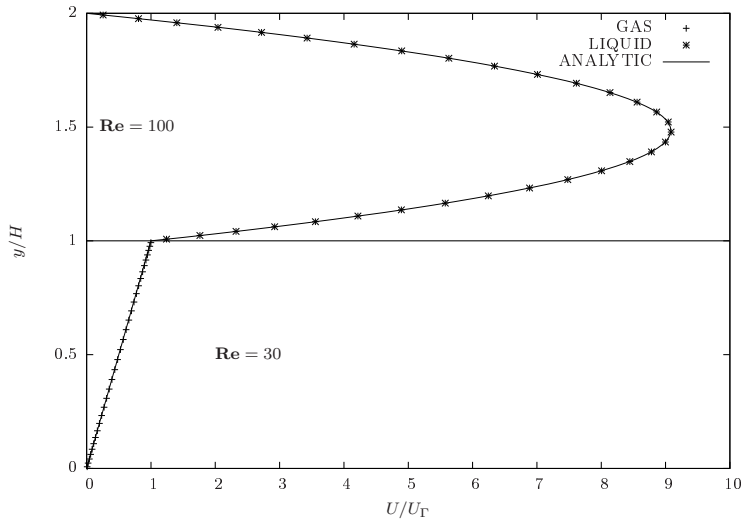

Figure 2.2: Solution of superposed Poiseuille/Couette flows acted by a bodyforce.

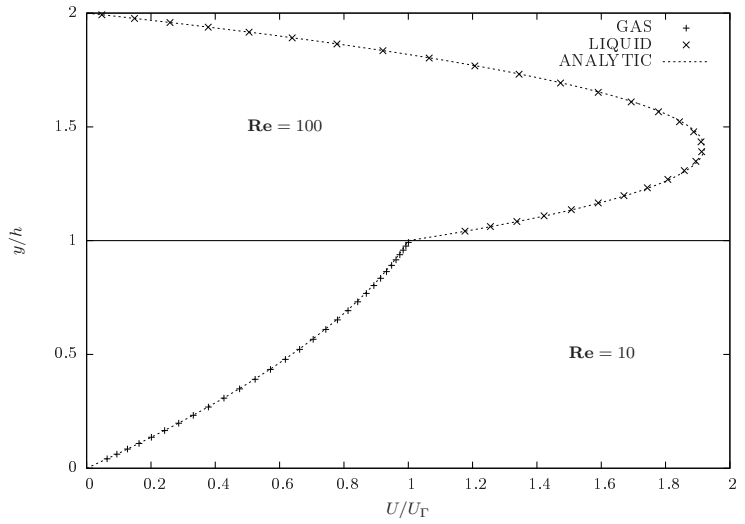

Figure 2.3: Solution of two superposed Poiseuille flows acted by a bodyforce.

Error analysis: grid convergence study

The geometry of the domain herein used corresponds to one of a unitary cube for each of the two subdomains, i.e. liquid and gas phase. Each direction is partitioned in 32 equidistant stripes in the streamwise and wall-normal direction, while for the spanwise direction 16 partitions were made, forming a hexahedral pattern of 32-by-32-by-32 cubes.

A comparison of the numerically obtained solution with its corresponding analytical counterpart should shed some light on the order of approximation imposed by the proposed coupling methodology, as it can be seen in figure 2.4. By calculating the maximum relative error over 3 domains refined by a ratio of 2 which its corresponding solution has reached the steady-state, at a time $t = 180\,s$, an error reduction of order $p \approxeq 1.6$ is found. The

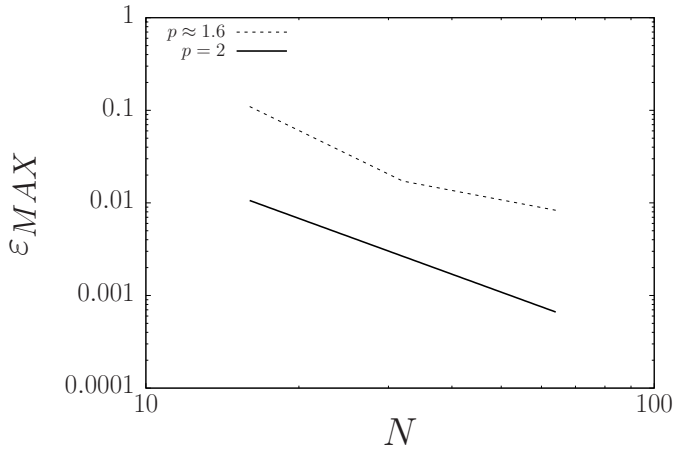

Figure 2.4: Maximum relative error over succesively refined grids.

maximum relative error is found to lie on the the physical boundary where the coupling is made. Previous error studies made on the numerical method without coupling (see [52]) claim an error reduction of order $p \approxeq 2$. The order reduction due to the implementation itself was expected, and is well documented in the literature (see [29]). The corresponding solution is shown in figure 2.3.

Chapter 3

Large-eddy simulation validation of Coupling Strategy

This chapter is a follow-up of section 2.3, where the study of two types of laminar interfacial flows were carried out as validation for the *incremental pressure-correction* algorithm using the *Picard-iteration* strategy for the coupling. There, the objective was to give a first glimpse on the overall behaviour of the proposed coupling, at the same time serving as a means to determine the order reduction of the solution close to the interface. On the other hand, this chapter serves to establish how appropriate the coupling method is when used in conjunction with a no-model approach for turbulence. Note that close to the interface the domain will be refined in a way that will allow for the viscous sub-layer to be *well-resolved*, thus not allowing for under-resolution of turbulent scales that would otherwise be misrepresented and could lead to numerical instability.

In the following section, an introduction on the numerical simulation of sheared interfaces between non-miscible fluids is made. A wide range of literature is presented, and brief descriptions are made. In section 3.2, a basic exercise on the scaling is made where some subtle, but essential, steps in the scaling of the sub-domains are highlighted. The rest of the chapter will be dedicated to describe a canonical type of flow best described as *counter-current*, fully developed boundary-layer flow. More precisely, a counter-current flow driven by opposing pressure gradients [29] will be revisited and results compared with DNS data. Such validation will include first- and second-order moments of the statistics obtained from its simulation, and qualitative assessments of different turbulence features will also be made.

3.1 Introduction

Most numerical simulationsfor boundary-layer flows around sheared gas-liquid interfaces has been confined to DNS. Specifically, the work of Lombardi et al. [29] focused on turbulent counter-current flows driven by a pressure gradient. There it was found that the boundary layer characteristics on the gas side (specifically air) are much similar to that of a bounded channel, whereas for the liquid side velocity correlations have its peak closer to or at the interface thus significantly altering all statistical quantities. Significant coupling of the *Reynolds stresses* across the interface were reported.

Later works [21, 22, 25, 28] focused on mass transfer over sheared, deformable interfaces. More precisely, these works focused on the effect of waves in the transfer of passive scalars enhanced by wind-driven turbulence, using a *Schmidt* Number of order unity. It was found that gas-to-liquid mass transfer was controlled by streamwise eddies producing ejections on the liquid side. Unfortunately, these works cannot directly depict gas-liquid mass transfer of interest in Oceanography because the scales required for accurately represent for such transfer are of several orders of magnitude smaller than the scales of turbulent fluid motion, thus rendering DNS unsuitable for highly dispersive scalars (i.e. for CO_2 in water $Sc = 600$). Note that the "small" eddies in isotropic flow turbulence scale with $1/Re^{3/4}$, whereas for turbulent scalar transport it scales as $1/\sqrt{Sc}$. To circumvent this limitation, Takagaki et al. [43] used an *Approximate Deconvolution Method* (ADM) on the scalar equation to study mass transfer across gas-liquid deformable interfaces, where the gas side is driven by a pressure gradient. Such work is an extension of the research made by Komori et al. [21]. In the latter, was shown that higher *Schmidt* numbers confine the scalar boundary layer closer to the interface thus increasing the vertical concentration gradient, at the same time enhancing mass transfer while diminishing mass entrainment into the liquid column. More importantly, across a wide range of Sc it was shown that the scalar transfer rate is only weakly correlated to wave motion, due to the already mentioned fact that the main mechanism of mass transfer is imposed in the liquid side.

Given that geophysical flows are highly turbulent, the subject of this chapter is to study fully developed boundary-layer flows over sheared interfaces.

3.2 Scaling for boundary-layer flows over coupled interfaces

A scaling over the domains that comprise the different fluids is necessary whenever a numerical experiment is sought. This scaling is carried out in a way that guarantees that the

size of the sub-domains, here Ω_1 and Ω_2, remain invariant (more on this point later) and, by corollary, preserves the viscous lengths equal. For the sake of simplicity, the discussion will be held assuming that the comprising domains, where the numerical simulation is carried out, are horizontally periodic boxes of size (pL, mL, nL); where $p, m, n \in \mathbb{Z}$ and L a length-scale, and x, y, z correspond to the stream-wise, span-wise, and vertical directions. Lastly, we will refer to the interface as the non-empty intersection of the sub-domains as $\Gamma = \partial\Omega_1 \cap \partial\Omega_2$, having in mind that always $\Omega_1 \cap \Omega_2 = \emptyset$.

In the case when one is interested of studying near-interface turbulence [25, 29], the velocity, time, and length scales $(\mathbf{u}_*^e, \nu/(\mathbf{u}_*^e)^2, h)$ do not necessarily correspond to those of a classic channel flow. In specific, the effective shear velocity $\mathbf{u}_*^e$ is highly dependent on the momentum-density ratio condition $\mathcal{R} = \sqrt{\rho_1/\rho_2}$; it should be noted that when the system is highly stratified the interfacial shear velocity approaches to that of a channel flow, in other words $\mathbf{u}_*^e \to \mathbf{u}_*$ if $\mathcal{R} \to \infty$.

Depending on the scenario, one may be interested in having a frame of reference that advects at a velocity roughly equal to that of the interface, in other words, a flow that goes to a near-zero velocity at the interface so vortex structures product of the interface interaction convects at a near-zero velocity. In other cases, a stationary frame of reference will be adopted without needing much change over the initial conditions. Regardless of the case,this work will be limited to the study of turbulent boundary layers with the same *Reynolds Number*. For this, the following condition arises if we want to preserve the same viscous length scale for both domains, i.e. for $h^+ = h\mathbf{u}_*^e/\nu$ and h to remain invariant, which stems from the Neumann condition enforced at the interface:

$$\frac{\mu_{gas}(\mathbf{u}_\Gamma)_{gas}}{h}\left(\frac{\partial u}{\partial z}\right)_{gas} = \frac{\mu_{liquid}(\mathbf{u}_\Gamma)_{liquid}}{h}\left(\frac{\partial u}{\partial z}\right)_{liquid}$$

then

$$\frac{\mu_{gas}}{\mu_{liquid}}\sqrt[2]{\frac{\rho_{liquid}}{\rho_{gas}}}\left(\frac{\partial u}{\partial z}\right)_{gas} = \left(\frac{\partial u}{\partial z}\right)_{liquid}$$

Thus, for h^+ to remain invariant, the following constraint has to hold:

$$\frac{\mu_{gas}}{\mu_{liquid}}\sqrt[2]{\frac{\rho_{liquid}}{\rho_{gas}}} = 1 \tag{3.1}$$

Also, one can find an integral relation for the interfacial shear velocity $\mathbf{u}_\Gamma$ and $\mathbf{u}_*^e$ by equilibrium considerations, assuming that for each sub-domain h is half the total depth. In channel flows we have an effective shear velocity is described by:

$$(\mathbf{u}_*^e)^2 = \Pi h$$

and, in the case of interfacial flows:

$$\tau_\Gamma/\rho = (\mathbf{u}_\Gamma)^2 = 2\Pi h$$

thus,

$$\mathbf{u}_\Gamma = \sqrt{2}\mathbf{u}_*^e$$

This scaling will be standard in this work, and can also serve as reference for interpreting the results often seen in literature.

3.3 Domain Configuration and fluid Properties

As described in the previous section, the idea of having equal viscous heights allow for a more homogeneous set of properties that serve as input for the simulation. That is, by maintaining the *Reynolds Number* equal for both sub-domains, the grid needed for the simulation of each phase can conserve the stretching and dimensions of the other. However this condition imposes certain qualities on the properties of the fluids that, if one is interested to draw a direct comparison with real-life scenarios, are somewhat stringent. This caveat is mathematically expressed in Equation 3.1.

Table 3.1: Fluid and sub-domain properties of the simulations. Note that the height of the lower subdomain changes for the case used for validation.

	Grid Dimensions	Fluid Properties at Temperature $T = 320K$		
		Density (m^3/s)	Kin. Viscosity $(\times 10^{-6}\, m^2/s)$	Dyn. Viscosity $(\times 10^{-6}\, kg/m \cdot s)$
Air (Upper)	$4\pi \times 2\pi \times 1$	1.08	18.11	19.62
Water (Lower)	$4\pi \times 2\pi \times 2(1)$	988.92	0.57	56.60

The *Reynolds Number* expressed in terms of the scales described in section 3.2, chosen for all simulations, is equal to $Re = 60.47$. Instead, if the *interfacial* velocity is used as characteristic scale, one obtains instead $Re = 171$. Each domain is constructed using a distribution of $128 \times 96 \times 64$ centroids in the streamwise, spanwise, and vertical directions, respectively. Vertical stretching using arc-tangent functions is performed on both domains in order to guarantee the resolution necessary to capture the viscous layer close to the wall. Finally, by setting the momentum-density ratio described in Equation 2.6 equal to $\mathcal{R} = 29.94$, one is are effectively setting a binary flow comprised of water and air, where its characteristics are described in Table 3.1.

3.4 Counter-Current Boundary-layer flow: Validation

Here, the canonical case considered by Lombardi et al. [29] is reproduced in order to validate the use of LES under the coupled framework. Again, the properties of the fluids and the dimensions of the subdomains are given in 3.1 with the only difference that the height of the lower subdomain is equal to that of the upper subdomain. Since the case under consideration is comprised by the turbulent boundary layers generated at the interface between the comprising counter-current flows, the total height of the subdomain can be considered as the height of the boundary layer itself, or δ_{99}. Thus, the interest is only on the coherent turbulence generated by the interface interaction and the boundaries parallel and opposite to the interface should convey a zero-stress tensor field by imposing a free-slip condition on such boundaries. Furthermore, the system is considered horizontally periodic.

3.4.1 Results: flow statistics

The statistically steady flow fields are averaged in time using 75 flow snapshots, and then spatial averaging over homogeneous directions is performed. Each snapshot is taken every 1.1 eddy-turnover times L/U_{bulk} of each comprising subdomain; in this particular scenario, the time scales should be similar, not equal, in either domain. In the case where condition 3.1 is not met, disparate time scales will be present and the time averaging process should be made differently for each case; typically, time scales in the air are much shorter than for water, requiring a much smaller timestep for integration in the air side and at the same time a much longer simulation time to arrive to a steady state in the water side.

Figure 3.1 show the velocity profiles and RMS of the velocity fluctuations, after normalization. General agreement is seen for the velocity profiles shown in Figures 3.1a and 3.1b, where given the higher inertia of water the velocity profile in the air side behaves similar to a wall bounded boundary layer; this latter assertion is further supported by Figure 3.1c. The reason for the variations on the velocity profile in the waterside are seen more evident in Figure 3.1d, where the RMS fluctuations passed by the air side (28.8 times as strong) do influence the boundary layer by making it thinner. Finally, a comparison of the present results with data obtained from a simulation where no model is used for the determination of the SGS fluxes is presented in the aforementioned figure. Such comparison elucidates the rather weak effect of the SGS fluxes in the flow, as expected for such a low Reynolds number. Nevertheless, a slightly higher state of streamwise turbulent fluctuations is captured using the LES model consequence of the use of the Boussinesq hypothesis for the linearization of the SGS stresses.

For the non-dimensional Reynolds shear stresses $\overline{uv}/u_\tau^2$, plotted in Figures 3.1e and 3.1f,

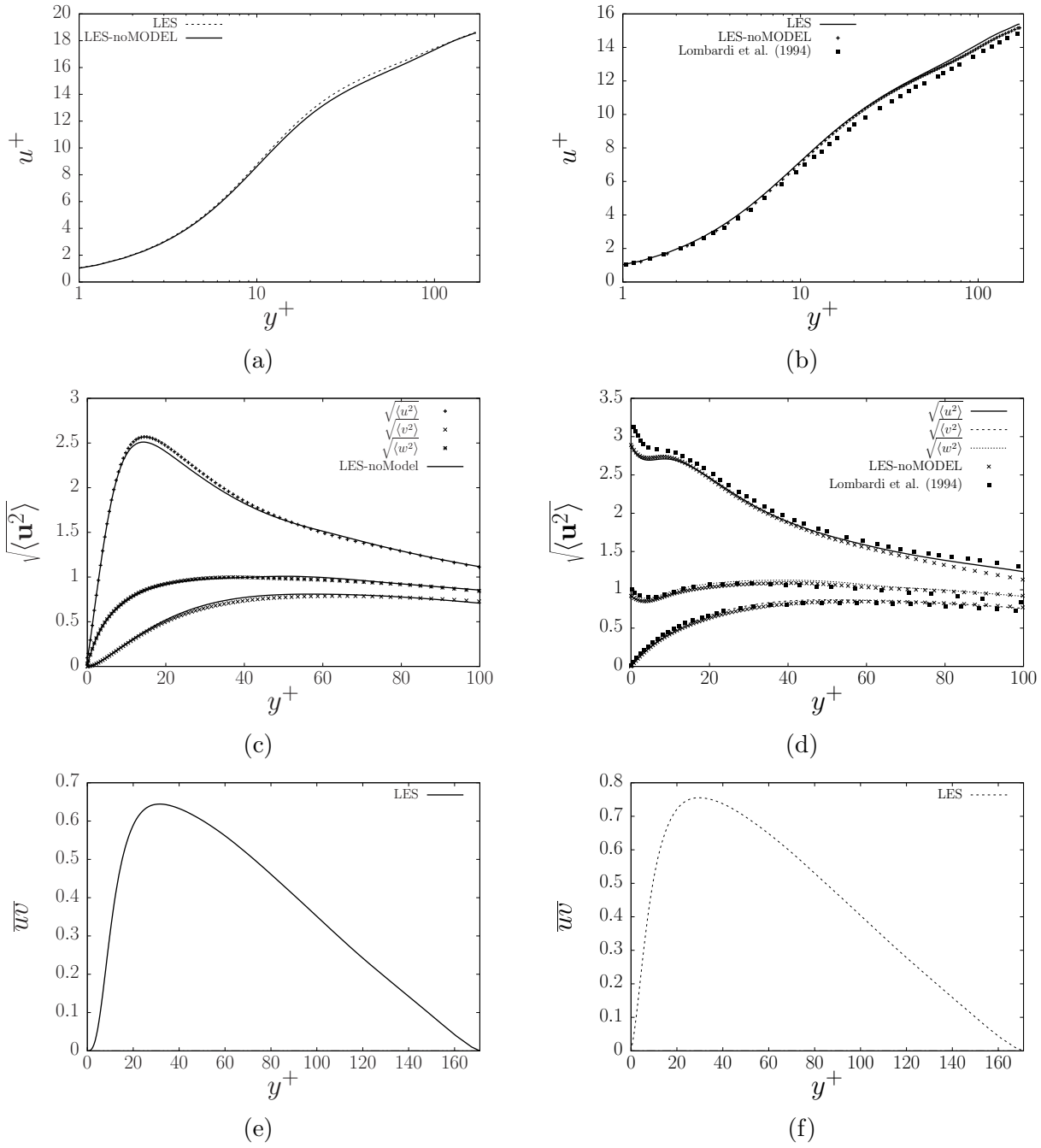

Figure 3.1: Mean vertical velocity and RMS profiles for the air and water sub-domain. (a) semilog chart of mean vertical velocity profile of the air and (b) water parts of the sub-domain; (c) RMS velocity fluctuations for the air sub-domain and (d) water sub-domain; (e) mean Reynolds stress profiles for the air domain, and (f) the water domain.

results are qualitatively similar to those of wall-bounded turbulent channel flows. Nevertheless, in the region $20 < y^+ < 40$ the peak of $\overline{uv}/u_\tau^2$ is higher on the water side compared to the air side which confirms the higher RMS intensities mentioned earlier. These quantitative differences reveal that the near interface region on the water side of the system is 'better'

mixed compared to its air counterpart.

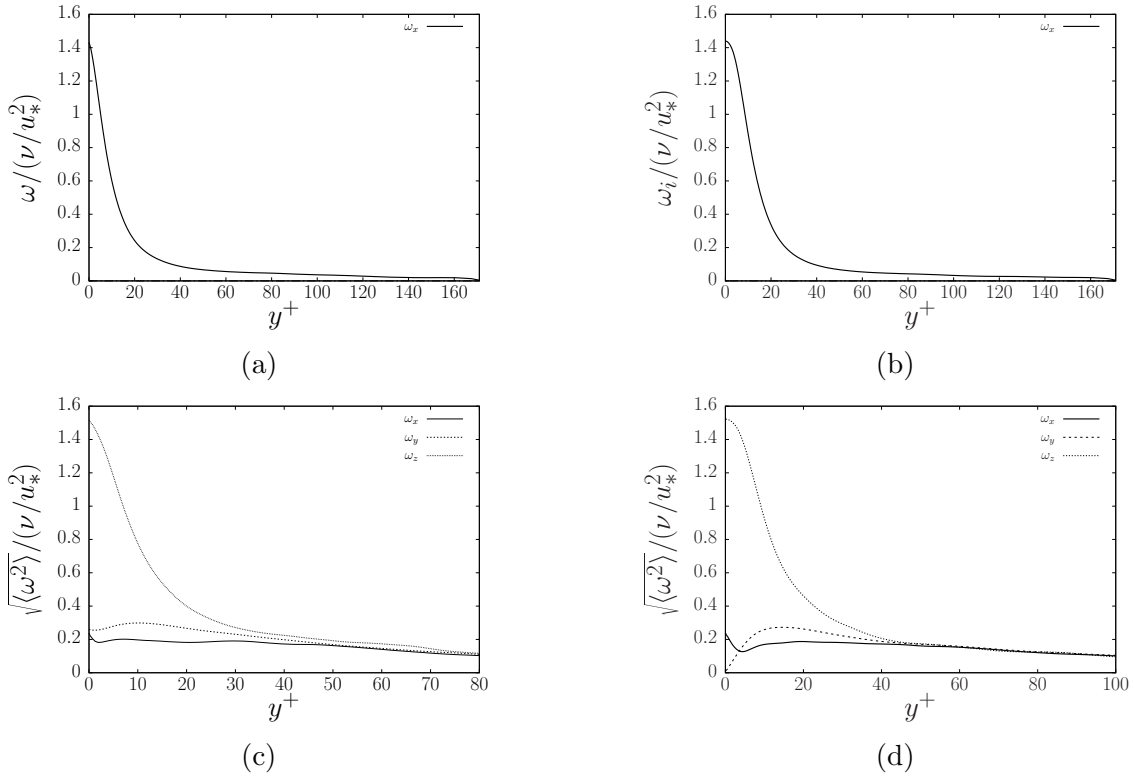

Figure 3.2: Mean vertical vorticity profiles and RMS profiles for the air and water sub-domain. (a) chart of mean vertical velocity profile of the air and (b) water parts of the sub-domain; (c) RMS of vorticity fluctuations for the air sub-domain and (d) water sub-domain.

3.4.2 Mean vorticity and intensities

Important properties on the behavior of vorticity close to the interface can be deduced from the interface conditions described in the previous chapter. Specifically, the spanwise vorticity must be continuous across the interface and the structure of the vorticity correlation tensor should remain invariant (more on this later). By applying the curl on Equations 2.6 and 2.4 we obtain the following relations, for the air side:

$$\omega_3\big]_{\Gamma,air} = \frac{1}{\mathcal{R}}\left[\frac{\partial u_3}{\partial x_1} - \frac{\partial u_1}{\partial x_3}\right]_{\Gamma,water} \tag{3.2}$$

$$\frac{\partial \omega_3}{\partial x_3}_{\Gamma,water} = \frac{h^+_{water}\mu^2_{air}}{h^+_{air}\mu^2_{water}}\left\{\frac{\partial}{\partial x_1}\frac{\partial u_3}{\partial x_2} - \frac{\partial}{\partial x_3}\frac{\partial u_1}{\partial x_2}\right\}_{\Gamma,air} \tag{3.3}$$

Vorticity fluctuations and profiles are shown in Figure 3.2. From Figures 3.2a and 3.2b is clear that the spanwise vorticity is equal at either side of the interface, and from the

RMS profiles 3.1c and 3.1d on the airside and on the waterside a rather slight bump close to the interface on the streamwise component of vorticity RMS fluctuations is seen. This phenomenon is reported in wall bounded flows [20], where it is attributed to the appearance of streamwise vortices close to the wall. In any case, given that horizontal motions are not constrained by the interface such bump is detected in Figures 3.2c and 3.2d although in a lesser intensity in the waterside given the higher inertia of the fluid.

3.4.3 Near-interface streaks and vortex visualization

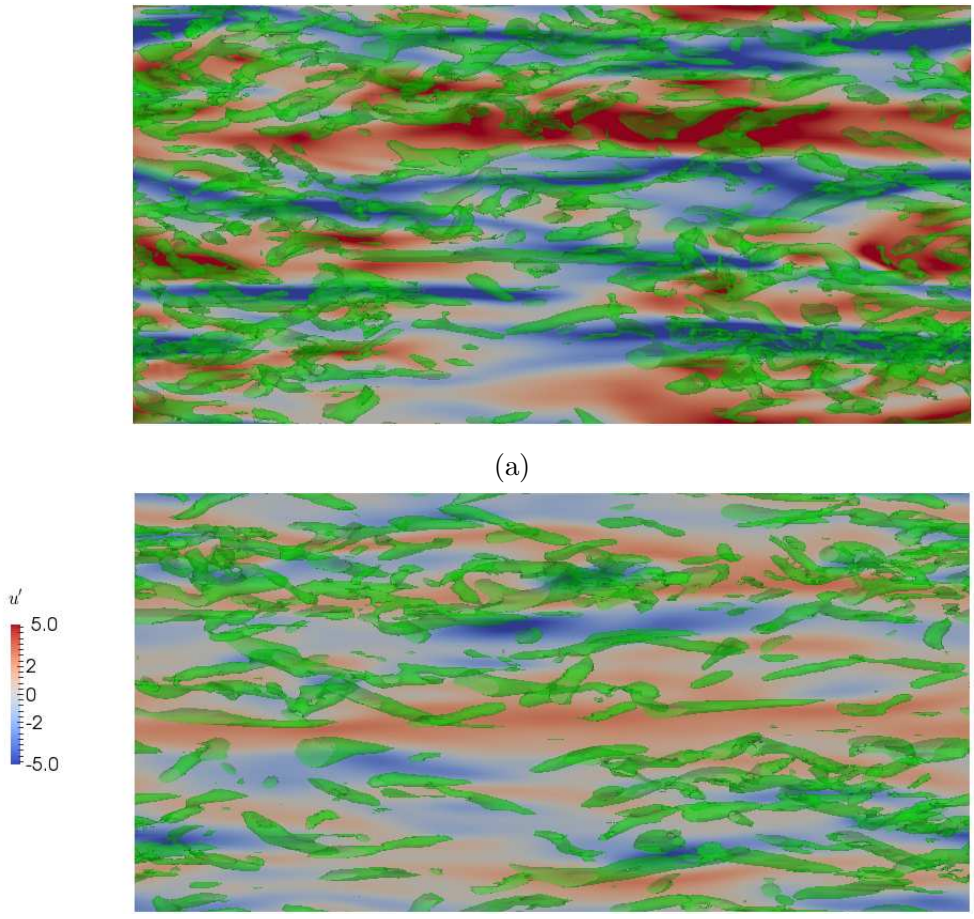

(a)

(b)

Figure 3.3: Plane contours of streamwise velocity fluctuations at height $y^+ = 4.22$ off the interface, and vortex cores educed using the $\lambda 2$ criterion.

Figure 3.3 show the low-speed streaks that are present near the interface, at either side. In general the streaky structures presented seem to be more persistent in the vertical on the airside (Figs. 3.3b and 3.3a) than on the waterside, as pointed out by [29]. Surprisingly, the average and spacing length of the streaks are higher ($\Delta x^+ = 1100, \Delta z^+ = 130$) than those

normally described in literature [20, 23, 29], thus it is expected to see an artificial reduction of the friction coefficient close to the interface.

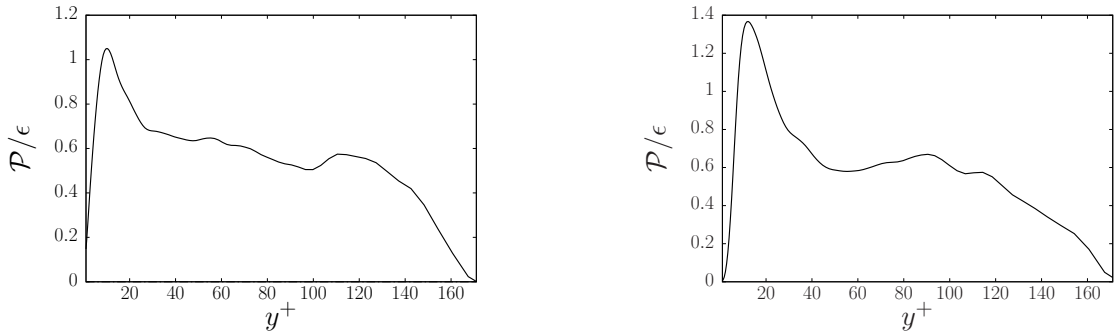

Figure 3.4: Mean vertical production-to-dissipation ratio profiles for the (a) upper and (b) lower sub-domains. Note that low-speed streaks are colored in red (velocity fluctuations on the opposite direction of the flow).

As mentioned before, this increased persistence of the streaks is theorized to be caused by the higher shear rate present in the airside. This idea was put forth by Lam and Banerjee [25], where the parameter $S = (\partial\overline{u_1}/\partial x_2)|\overline{u_1' u_2'}|/\epsilon$ was proposed as a measure for determining the existence and persistence of streaks. For our case in question, it simply means that whenever the ratio of production and dissipation of TKE at a certain height is of order $\mathcal{O}(1)$ or higher streaks can be sustained. Note that the parameter is unable to predict whether streaks will be generated. More specifically, a direct comparison between Figs. 3.4a and 3.4b show that the ratio $S = \mathcal{P}/\epsilon$ reaches a maximum value below $y^+ = 20$ on both phases, nonetheless on the airside it remains close to unity up to a height of $y^+ \approx 34$.

Vortex inclination

The population of vortices present in the near-interface region can be classified into three types [28]: interface-attached, quasi-streamwise, and hairpin. The second type of these list is common in wall-bounded turbulence, while the other two are common to slip-bounded turbulence. Given that the interface possesses a behavior in between the limiting states mentioned, these three classes inhabit the near-interface region. The probability distributions of the vortex inclination angles observed in Figure 3.5(a)-(d) in the near interface region confirm the observations made previously. It is confirmed that quasi-streamwise vortices populate mainly the region on the air side of the interface, since the pdf of θ_{yx} in Figure 3.5(c) centers around 90° and 270° indicating negative and positive streamwise structures. In regions where vortices have roughly such angles, high modulus shear is prevalent, thus it is expected

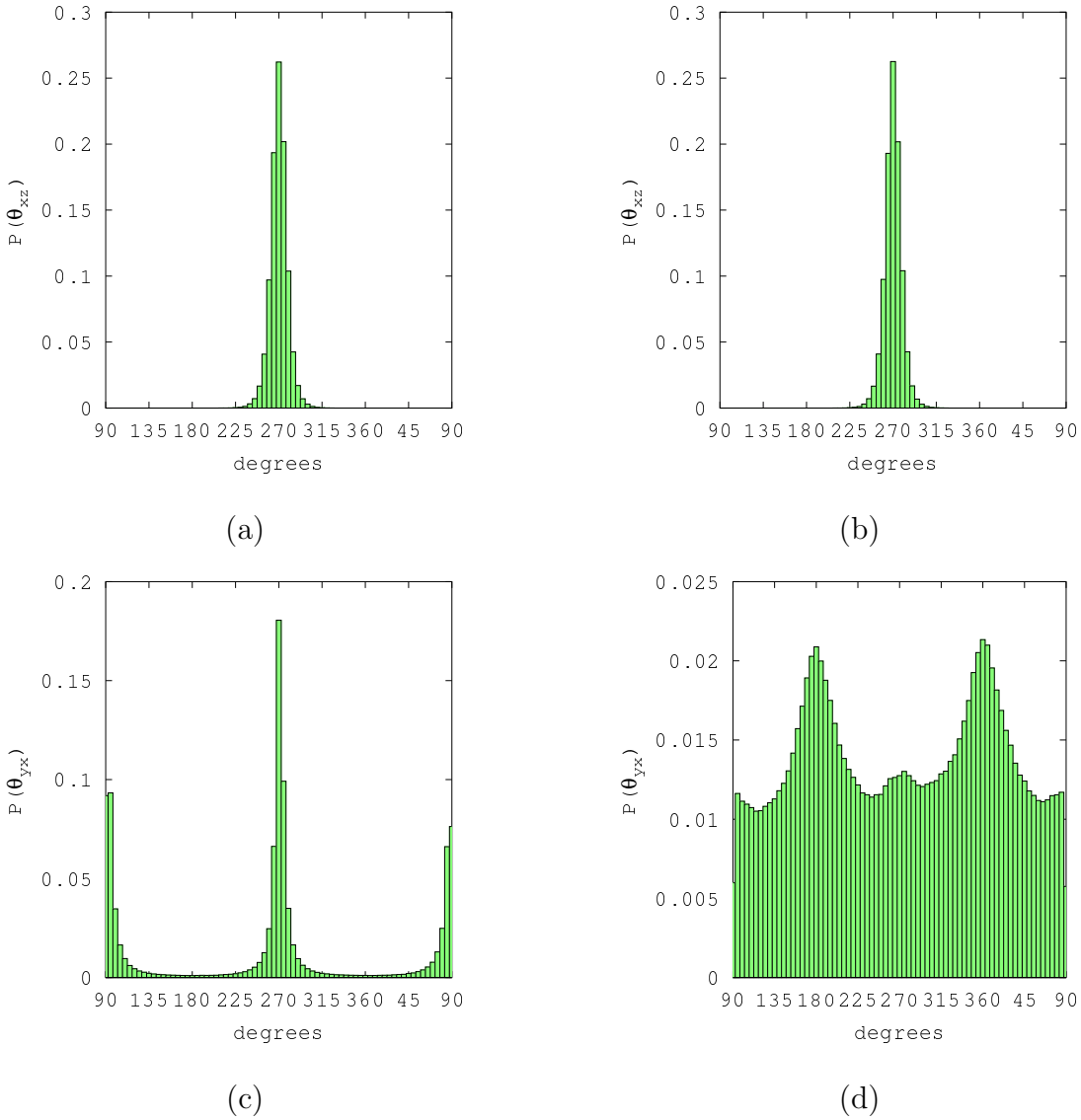

Figure 3.5: pdf of vortex inclination angles $(\theta_{xz}, \theta_{yx})$ taken at $y^+ = 0.7$ away from the interface in –(a) and (c)– the air side, and –(b) and (d)– the water side. The angles are measured clockwise starting from the interface-normal axis, y, pointing into the domain, or the streamwise axis, x.

that as highly positive shear events may induce to the generation of streamwise vortices it is expected that the less probable negative streamwise vortices are generated by negative shear events. On the water side, Figure 3.5(c), the θ_{yx} reveal the presence of the legs of hair-pin vortices of angles spanning $(135°, 180°)$ and $(315°, 360°)$ ranges, where the peak values indicate these vortices to be interface-connected as well.

3.4.4 Turbulent kinetic energy budget

Now, the different terms in the turbulent kinetic energy, $k = \sqrt{u_i' u_i'}$ (TKE) evolution for the resolved scales can be written in the following manner:

$$\left\langle \frac{Dk}{Dt} \right\rangle = \langle P + \Pi_k + T_k + D_k + \epsilon \rangle = 0, \quad t \to \infty$$

$$\begin{aligned}
P &= \overline{u_i' u_j'} \frac{\partial \overline{u_i'}}{\partial x_j} \\
\Pi_k &= -\frac{1}{\rho} \frac{\partial \overline{p' \, u_i'}}{\partial x_i} \\
T_k &= -\frac{1}{2} \frac{\partial \overline{u_i' u_i' u_j'}}{x_j} \\
D_k &= \frac{1}{2} \frac{\partial^2 \overline{u_i' u_i'}}{\partial x_k \partial x_k} \\
\epsilon &= -(\nu + \nu_{\text{sgs}}) \overline{\frac{\partial u_i'}{\partial x_j} \frac{\partial u_i'}{\partial x_j}}
\end{aligned}$$

These terms, in the order presented above, receive the name of production, pressure diffusion, turbulent transport, turbulent diffusion, and dissipation of TKE. In Figure 3.6, the vertical profiles for the different terms involved in the TKE equation are presented. Although the results cannot be directly compared with DNS data, it is expected that a vis-a-vis comparison of the budget terms should throw similar results. In particular, production is slightly higher and closer to the interface in the water side when compared to the air side, and dissipation is partially balanced by turbulent diffusion and viscous transport.

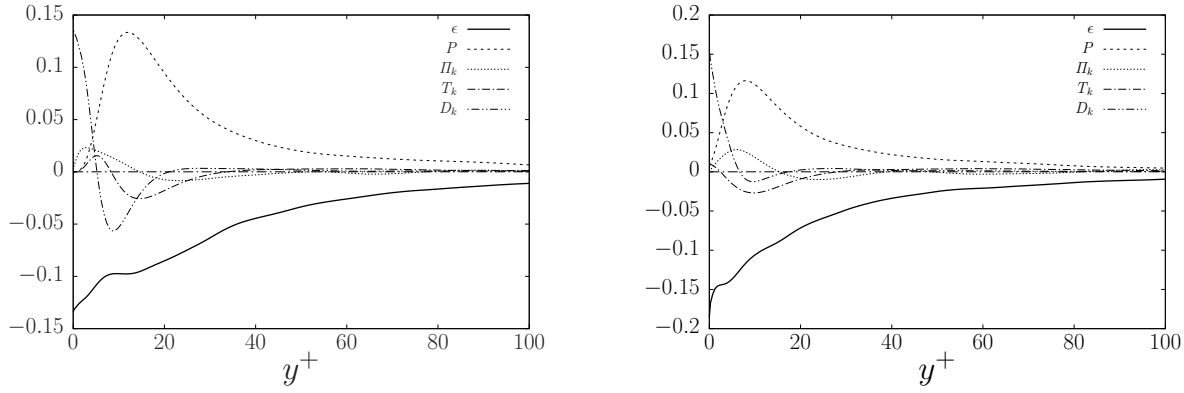

Figure 3.6: Mean vertical TKE profiles for the (a) air and (b) water sub-domains.

3.4.5 Turbulent Reynolds stress budget

The transport equations for the resolved Reynolds stresses are derived from the incompressible Navier-Stokes equations. The generic transport equation can be written as:

$$\frac{D\overline{u_i'u_j'}}{Dt} = -\left(\overline{u_i'u_k'}\frac{\partial U_j}{\partial x_k} + \overline{u_j'u_k'}\frac{\partial U_i}{\partial x_k}\right) - \frac{1}{\rho}\left(\overline{u_i'\frac{\partial p}{\partial x_j} + u_j'\frac{\partial p}{\partial x_i}}\right) - \frac{\partial}{\partial x_k}\overline{u_i'u_j'u_k'} + \nu\frac{\partial^2}{\partial x_k^2}\overline{u_i'u_j'} - 2\nu\overline{\frac{\partial u_i'}{\partial x_k}\frac{\partial u_j'}{\partial x_k}} \tag{3.4}$$

In Equation 3.4, the terms on the right hand side are respectively named as production, pressure diffusion, turbulent transport, viscous diffusion, and dissipation. An important term is the pressure diffusion, which acts both as a source of energy and redistributes it. Such term can be further decomposed as follows:

$$\Pi_{ij} = \overline{\frac{p'}{\rho}\left(\frac{\partial u_i'}{\partial x_j} + \frac{\partial u_j'}{\partial x_i}\right)} - \frac{\partial}{\partial x_k}\left[\overline{\frac{p'}{\rho}(u_i'\delta_{jk} + u_j'\delta_{ik})}\right] = \mathcal{R}_{ij} - \frac{\partial}{\partial x_k}\mathcal{T}_{ijk} \tag{3.5}$$

Where the leftmost term in the right-hand side $\mathcal{R}_{ij}$ indicates the pressure-rate-of-strain tensor which serves as a redistribution of energy towards the isotropy of turbulence. The pressure-transport term, $\mathcal{T}_{ijk}$ constitutes a source of kinetic energy. Notice that due to the horizontal homogeneity of the flow, the transport equation for $\overline{uv}$ reduces to $\Pi_{12} - \epsilon_{12} = 0$. In Figure 3.7(a)-(b) it is shown that the reduction on the resolved cross dissipation, ϵ_{12}, on the near-interface region on the water side is balanced by an increase of Π_{12} through pressure.

A means of understanding the redistribution of energy along the cartesian directions can be devised by noting that the trace of $\mathcal{R}_{ij}$ is zero, due to conservation of mass. Thus, the resulting term called pressure-strain correlation can be written as:

$$\mathrm{PS}_i = \frac{1}{\rho}\overline{p'\frac{\partial u_i'}{\partial x_i}} \tag{3.6}$$

where a positive value of PS_i implies a transfer of energy to component i from the other components, and vice versa. In Figure 3.8a, energy in the streamwise and the spanwise direction are redistributed to the vertical direction in the near-interface region on the air side, which is qualitatively similar to wall-bounded turbulent flows. On the other hand, Figure 3.8b shows that energy is only drained from the spanwise direction and, contrary to the air side, the direction which benefits the most from such redistribution is the streamwise direction which justifies the increment in turbulent transport seen in TKE budget on the water side.

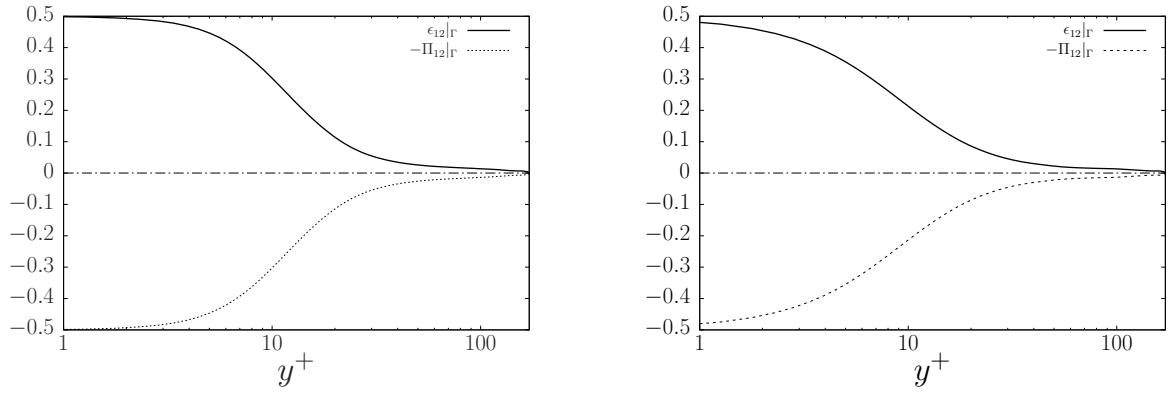

Figure 3.7: Mean vertical profiles of the $\overline{uv}$ budget for the (a) air and (b) water domains.

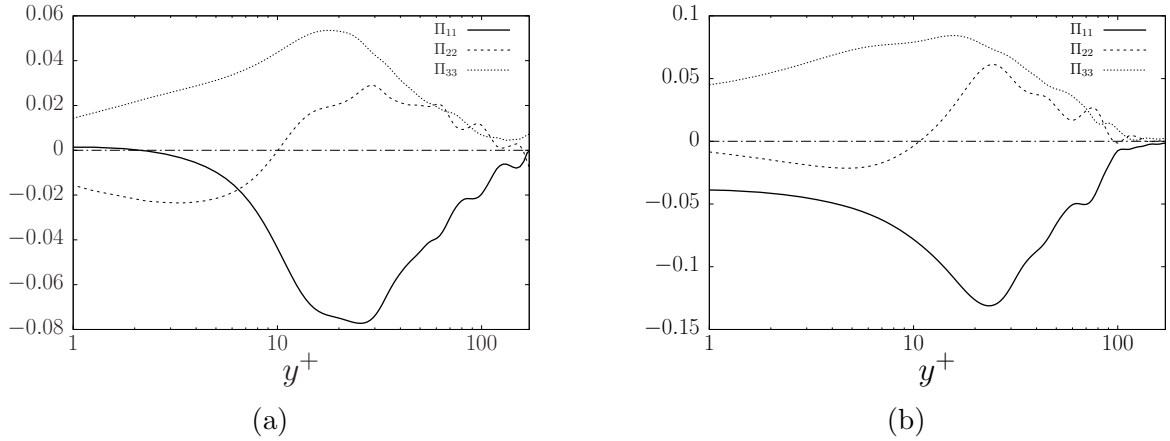

Figure 3.8: Mean vertical profiles of the velocity-pressure gradient tensor Π_{ij} for the (a) air and (b) water domains.

3.4.6 Reynolds Stress Analysis: Anisotropy Invariant Maps (AIM)

The so-called Lumley map for the different boundary layers is shown in Figure 3.9. The Reynolds stress structure depicted in Figure 3.9a qualitatively resembles that of wall-bounded channels, where the streamwise Reynolds stress $\langle\overline{(u')^2}\rangle$ becomes much higher than the other components of the diagonal as one gets closer to the wall, where this rod-like shape of the Reynolds stress tensor is very common. On the other hand, the boundary layer on the water side has a somewhat different state of Reynolds stresses, as shown in Figure 3.9b. The most salient feature is the absence of the one-component "tail" in the profile, indicating that the intensity of the rod-like shape of turbulence is not as high as in the other boundary layer.

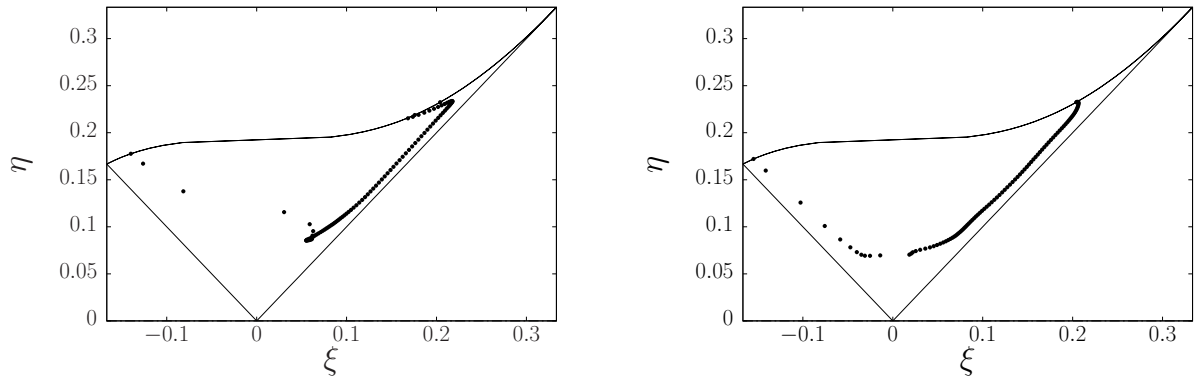

(a) (b)

Figure 3.9: Mean vertical profiles of the Reynolds stress AIM for the (a) air and (b) water sub-domains.

3.4.7 Quadrant analysis over strong realizations of flow

Having the necessity of understanding the physics behind the production of Reynolds shear stress and turbulent kinetic energy, here we make use of the quadrant analysis in order to unveil the differences between the boundary layers being studied. Note that the events herein described are relative to the direction of the imposed pressure gradient. Figure 3.10 shows that the two quadrants associated with the self-sustaining mechanisms of wall turbulence, sweeps (Q4) and ejections (Q2), behave similarly except for a vertical offset in the profiles for the water side (Figure 3.10(b)). Also, the Q2-Q4 crossing at $y^+ \approx 10$ typically associated to the intersection between the inner and outer layers in wall turbulence is present in both boundary layers. This location is also where the peak of production of turbulent kinetic energy is present. Note that no crossing between the interaction quadrants (Q1-Q3) is present in the near-interface region, instead it happens at $y^+ \approx 45$.

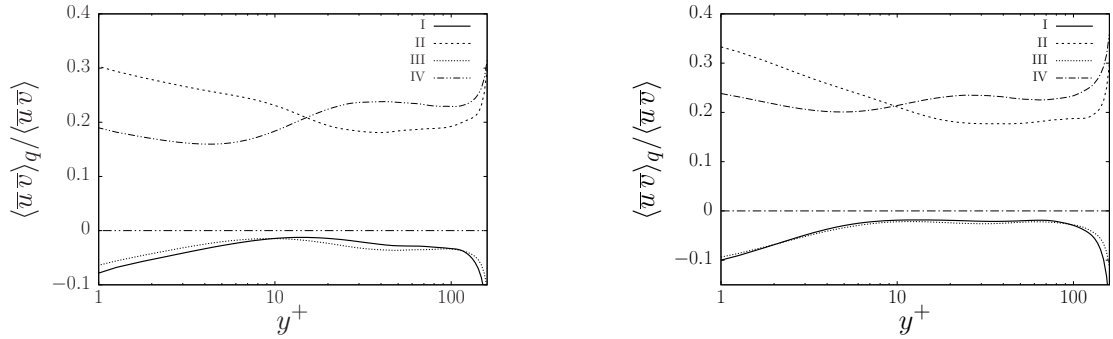

(a) (b)

Figure 3.10: Quadrants contribution to the resolved Reynolds shear stresses on (a) the air and (b) on the water.

A technique similar to that by Lombardi et al. [29] is proposed in to extract physically relevant near-interface, and possibly coupled, quadrant motions corresponding to high/low interface shear stress events. By using this technique, one could extract spatial information that is otherwise absent in the averaging process used to prepare Figure 3.10. The interesting feature of extracting only signals that are considered "strong" is that one can, to a certain degree, associate extreme interface/wall backflow events [27] to topological turbulent features of turbulence. Thus, the method proposes to:

- Select three equally spaced probes on the vertical, for every (x, z) location, in the near interface region ($y+ < 10$) on either side of the interface
- Whenever the velocity fluctuations on all three probes lay on the same quadrant, record the "Strong" event, along with the fluctuating velocities on the probe farthest from the interface, and record the corresponding interfacial shear stress in the (x, z) location.

From the method just described, the three monitor probes used are located at $y^+ =$ 1.0, 2.0, 3.0, and the statistics used a total of four horizontal plane (3 probes and the interface) samples for each of the 150 instantaneous realizations of the flows, spanning a viscous time of 165 units.

Figure 3.11 is the result of selecting only the signals considered "strong" for the coupled interaction of the fluid flows, taken at a viscous length $y^+ = 3.0$ off the free surface.The joint probability functions shown in Figures 3.11(a) and (c) show a bi-modal behavior on the streamwise velocities which seem to be weakly correlated with the vertical velocities. As it is shown in section 3.4.2, bi-modality of horizontal velocity fluctuations are due to the co-existence of streamwise and hairpin vortices in the near interface region. Furthermore, rare backflow (negative u) events correlate with extreme splat events (velocities toward the interface) in the case of water. This is further confirmed in Figure 3.11(d) where it is seen the prevalence of rare Q2 events over the rest. Instead, rare positive streamwise velocities correlate with rare splats which indicates a prevalence of Q4 events as seen also in Figure 3.11(b).

3.5 Instantaneous interfacial shear stresses and velocities

In Figure 4.13 large regions of negative fluctuating shear velocities are seen, thus indicating large regions of backflow velocities at the interface. Lenaers et al. [27] determined that for wall-bounded channel flows such regions of negative shear at the wall had a diameter of

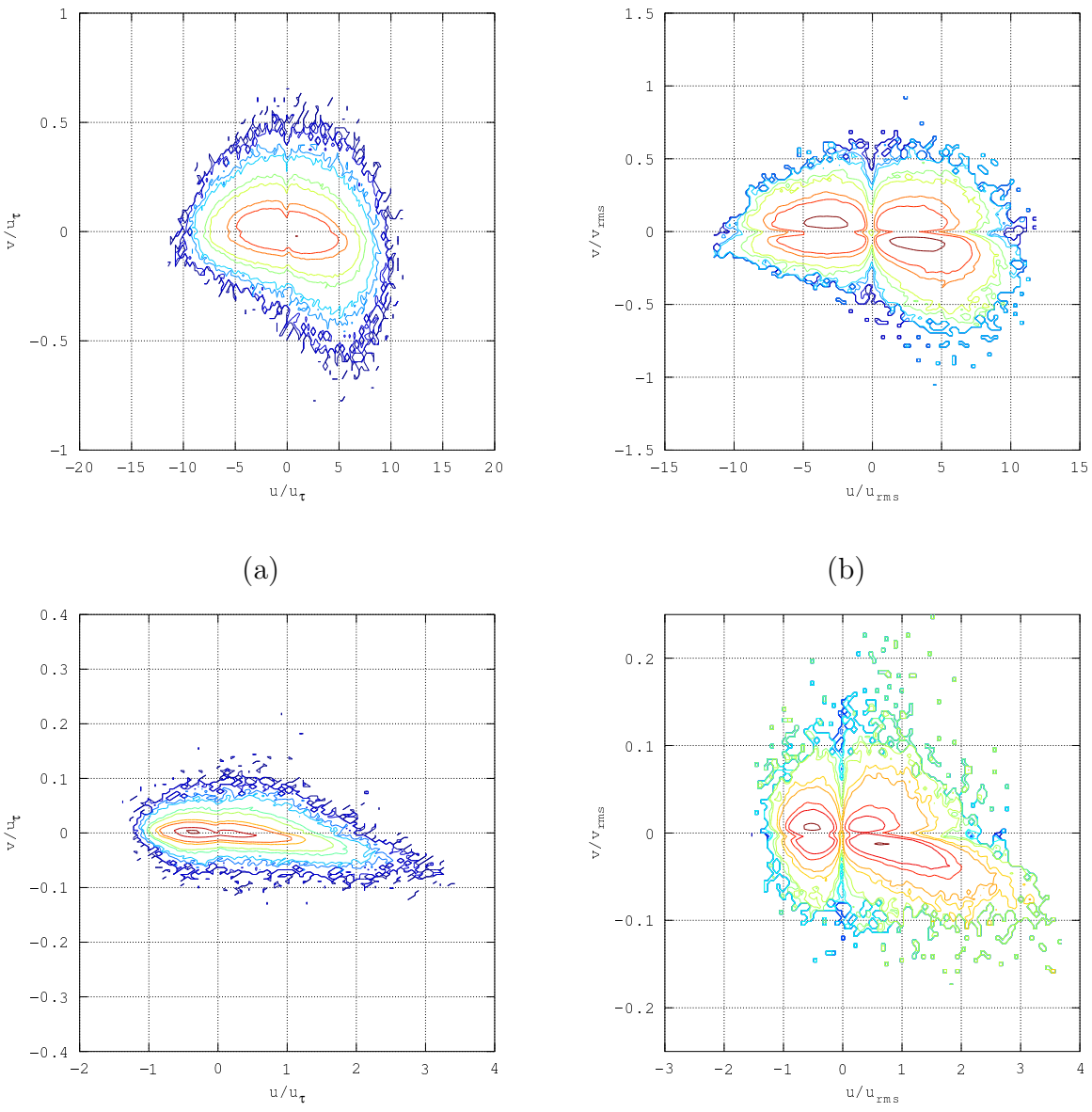

Figure 3.11: Joint probability distribution, plates (a)-air- and (c)-water-, and covariant integrand distribution, plates (b)-air- and (d)-water-, of velocity distributions associated with strong quadrant events at height $y^+ = 3.0$. The contours are log-scaled ranging from 10^{-7} to 1.

$l^+ = 20$ and were independent of the Reynolds Number, furthermore, these regions were induced by oblique vortices that are seldom shed from the wall, and the reason for the existence of such vortices is attributed to secondary instabilities in the self-sustaining cycle of wall-bounded turbulence [36]. Here, it has been shown that other types oblique vortices are present mainly due to the increased enstrophy generated at the interface. Furthermore,

Table 3.2: Skewness, flatness and RMS of instantaneous shear stress on the interface. Data used for comparison corresponds to DNS measures over a wall.

Re_τ	$\tau_{\Gamma\,\mathrm{rms}}^+$	$S(\tau_\Gamma^+)$	$F(\tau_\Gamma^+)$
Present			
171	0.166	0.0313	3.067
Lenaers et al. [27]			
180	0.367	0.930	4.257

the regions of negative shear stress possess a streaky shape indicating its relation with elongated and, possibly oblique, vortices.

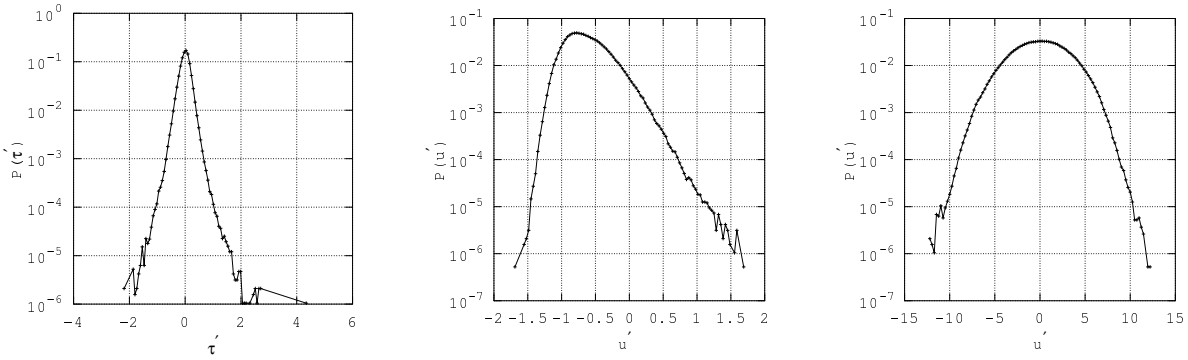

(a) (b) (c)

Figure 3.12: Probability distribution of (a) τ' events over the interface, and of streamwise fluctuating velocities at $y^+ = 1.26$ off the interface on (b) air, (c) water.

To study the frequency over which negative shear stress events happen over the interface, a PDF of $\tau' = \nu(\partial u/\partial y)$ is shown in Figure 3.12. However, not so infrequent negative events are seen, in spite the low convection of the interface due to the counter-current nature flows which for the air side should render a behavior similar to that of Lenaers et al. [27]. On the contrary, the present results disagree quite considerably from literature as it can be seen in Table 3.2. The salient exception of this disagreement is the flatness which, roughly speaking, indicates that high fluctuations of shear are present along the interface although the distribution of these is almost symmetric (low skewness) and, in general, a resemblance to a normal distribution is clear.

The quasi-normal distribution of interfacial stresses are indication of frequent backflow events close to the interface which by consequence reduce drag, as opposed to the much more infrequent events that normally occur in wall-bounded flows. These drag reducing events are being controlled by the water side, as it seems from Figure 3.12(c) where a large

portion of the velocity fluctuations are negative. In contrast, Figure 3.12(b) resembles to a wall bounded case where a positively skewed distribution is present and backflow events are less likely.

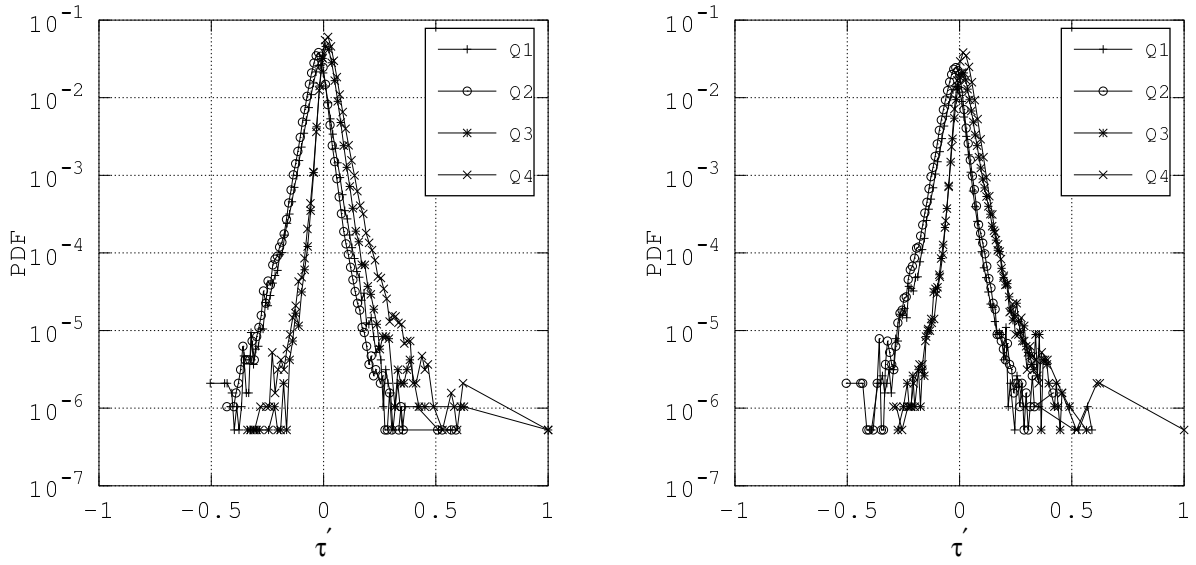

(a) (b)

Figure 3.13: Probability distribution functions of "strong" quadrant events on (a) the air side, and on the (b) water side.

Information about the strong quadrant events and its relation with shear backflow regions at the interface is presented in Figure 3.13(a) and (b), where a PDF of each quadrant versus τ' is plotted at either side of the interface. On the air side shown in Figure 3.13(a), strong events comprise 23.8% of all events present in the near interface region. From these events 30.9% correspond to ejections (Q2), 27.9% to sweeps(Q4), 21.8% to counter-gradient interactions (Q3), and 19.4% to interactions (Q1). Furthermore, events of type Q3 and Q4 contribute positively to the fluctuations of shear stress and both are positively skewed producing a tail of rare positive events, $P(\tau') > 10^{-6}$. On the other hand, events of the type Q1 and Q2 contribute negatively in the mean of shear stress fluctuations and no strong skewness is seen. A comparison with Figure 3.13(b) show a similar behavior to the one just described. Notice that the rare events shown are relative to the local frame of reference of each flow, thus a positive rare event should be read as an event in the same direction of the imposed pressure gradient.

3.6 Coupled quadrant events and instantaneous interface stresses

From previous sections, it was seen that the largest contributions to $\overline{uv}$ near the interface come from sweep and ejection events. Also, it was shown that strong ejection events contribute to along-the-gradient instantaneous shear stresses whereas ejections produce counter-gradient events that lead to backflows and, consequently, separated flows, on either sides of the interface. The latter results are rather unexpected, thus a different and, probably, coupled mechanism must be responsible for the separation and backflows in the near interface region.

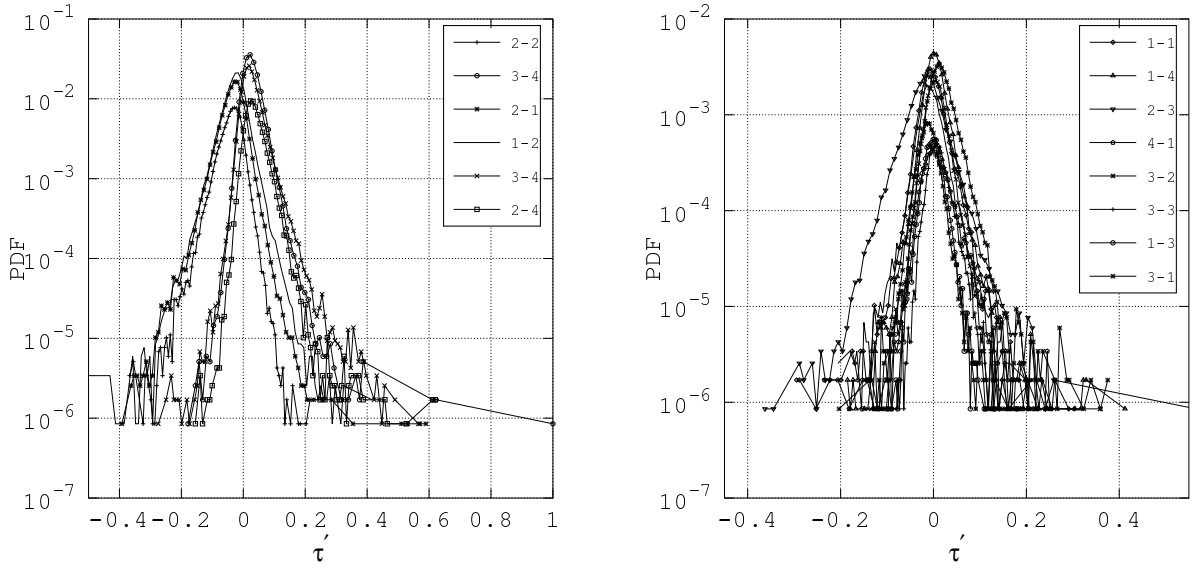

(a) (b)

Figure 3.14: Probability distribution functions of coupled events as function of the instantaneous interface stress, separated into (a) high-probability and (b) low probability events.

An analysis of the "strong", coupled events using the technique mentioned earlier is shown in Figure 3.14. The nomenclature referring to the coupled events will be presented just as the number of the quadrants separated by a hyphen, where the first digit refers to the air phase whereas the second refers to the water phase. By extracting those quadrant events that are considered not only as "strong" but also those that happen simultaneously at some (x, z) on the near interface region at either side, as described previously, one gets an account for the 16 possible coupled events that could contribute to the negative counter-gradient motions at the interface. Furthermore, by isolating the high probability signals from the low ones one could consider only those events relevant under the framework of LES. In

this case, all distributions with a mode lower that 0.005 are considered as low probability events. Under such conditions, it follows that ejection events on the air side contribute to negative events except when coupled with sweeps on the water phase. Sweeps are more prominent in the water side of the system where they always contribute positively to the generation of instantaneous shear stresses. Notice that all high probability coupled events always involve either Q2 or Q4 events, and on the low probability side such events produce skewed distributions.

Chapter 4

Couette flow in a channel driven by a Poiseuille flow above

We consider the canonical case of a turbulent Couette boundary layer generated by the transient traction generated by a Poiseuille turbulent boundary layer at the interface between two fluids, as seen in Figure 4.1. Similar cases have been studied [28, 29], but for boundary layers of the same class, whereas this case is an in-between the simulations usually performed in literature and what it can be found in applied disciplines. This particular configuration is more likely to be of interest in physical oceanography and limnology, and physical meteorology, since it represents a large class of flows that interact through a sheared interface between the two component fluids object of such disciplines: water, and air. To give examples, near-surface mixing and stratification in pre-Alpine lakes are mainly driven by winds, or the turbulent Ekman layer in the ocean is driven by the shear stress imposed by the wind, also Langmuir circulations are formed by the interaction between elongated coherent structures in the upper ocean layer and the ABL, and the feedback mechanisms responsible of cooling the Earth's surface are due to local heat, and water vapor, exchange mechanisms between the ocean and the atmosphere. Furthermore, it is well known that the self-sustaining turbulent mechanisms in Couette flows generate more elongated coherent structures [5] compared to wall-bounded flows at the same *Reynolds Number*, thus its use for the study of turbulence may offer information only obtainable in wall-bounded channel flows at higher *Reynolds Numbers*.

Simulations of coupled air-water systems have been conducted mainly for the study of heat/scalar transfer accross its interface, always over low Reynolds number regimes. The most recent account of wind-driven coupled air-water DNS is the work of Kurose. et al. [24], where wind-generated waves are resolved directly using an *Arbitrary Lagrangian Eulerian* technique. Although only phase-averaged statistics of turbulent flow quantities are

presented, the results show that the wavy boundary layer developed in the air side is similar to that of an open channel boundary layer. Although the waves result of wind traction for the Reynolds number considered, $Re_\tau = 171$, are well within the capillary regime, the wavy boundary layer developed on the water side is accompanied by Langmuir circulations, with a Langmuir number of $La = \sqrt{u_s/u_\tau} \approx 1/300$. A more exhaustive description of the statistics for turbulent flow quantities under a coupled wavy system is presented by Fulgosi et al. [12], although for a counter-current Poiseuille-Poiseuille air-water domain. This work focuses on the statistics on the gaseous side, where a $Re_\tau = 171$ is set for the whole system, in which waves again fall into the capillary range as the wave slope falls in $a\,k = 0.01$. There, first- and second-order statistical moments show that the gaseous boundary layer is again similar to that of an open channel flow where the interface is seen as a 'ductile' solid surface: elastic tangential deformations account for the reduction in overall drag in the wavy interface. In general, the interface acts as a dampener of the intensity of the various turbulent quantities, which reduces dissipation. A recent work of the Authors [30] has extended the previous study not only to second- but to higher statistical moments, where damping becomes more evident. Besides that, it was shown that the near-interface state of fluctuations in the water side is responsible of the occurence of so-called backflow, or separation, regions across the interface which alone reduces drag, without having capillary waves at the interface.

In the present study the flow in the bottom domain, or the water shallow channel, resembles, in principle, that of a Couette flow. The literature on direct numerical simulation of Couette flows, and its physics, is not as abundant as for wall-bounded channel flows. One salient work made by [5], studies the structure of near-wall turbulence suing DNS and laboratory experiments. There, it was shown that the structure of turbulence in the moving wall presents large differences on the shape of the Reynolds stresses when compared with wall-bounded channels. In fact, although the coherent structures generated in the near (moving) wall region are quite similar to its zero-velocity counterpart, the fact that the maximum of Reynolds stress is not located in the buffer region leads to a contradiction in the accepted notion that turbulence generation mechanisms cohabit in regions of high Reynolds stress. Instead, the maximum is located in the centreline of the channel which explains the stronger influence of the outer region on the boundary layer, by enhancing the contribution of sweeping events and concurrently diminishing ejection motions in the near wall. Incidentally, this work has shown that due to the different symmetries present in Couette flows, two possible realizations on the flow are possible depending on the domain dimensions: a 'periodic', and a 'disordered' state where large-scale vortical motions can develop due to the larger dimensions of the domain.

Literature on coupled Couette flows is even more scarse [24, 28], and is mostly focused on

the study of passive scalar transfer. Specifically, the work of Liu et al. [28] studies coupled air-water Couette-Couette systems in which ambient temperatures are used leading to different Reynolds numbers on the comprising flows, that is, where $Re_\tau^{\text{air}} = 272$ and $Re_\tau^{\text{water}} = 120$. The study claims that due to the presence of larger and more persistent streaky structures on the water side, the intensity and state of turbulent fluctuation quantities in the near interface region on either side of it is dominated by the liquid. The question of whether these structures are longer and more persistent due to the rather low Re_τ or to the thinner interface-bound boundary layer present in the water side remains open. At present, no numerical studies concerning coupled Poiseuille-Couette flows have been made, to the Authors' knowledge.

The present work concerns the study of the boundary layers formed on a coupled air-water Poiseuille-Couette system, where the shear Reynolds number is kept equal and the interface between the comprising flows kept flat. Departing from previous studies, special attention will be given to the boundary layers formed on the shallow water domain, where statistics on the turbulent flow quantities are made. Additionally, a study of interface flow separation is made via the extraction of strong backflow events present in the near-interface region of both flows. Finally, an examination of the relation between separation regions and the production of near interface positive vertical vorticity is made using conditional-averaging.

The chapter is organized as follows: Section 4.1 introduces the description of the problem and the mathematical approach used to attack the problem numerically. Section 4.2 presents the low- and high-order statistics of the flow, as well as the visualization of vortex structures, quadrants, and TKE budgets. Section 4.3 concerns the study of backflow events, and the conditional averaging via VISA technique.

4.1 Mathematical and Numerical approach

4.1.1 Problem description and Mathematical approach

This works considers a turbulent Poiseuille-Couette flow bounded by a lower wall and an upper slip boundary separated a height of 3δ, as depicted in Figure 4.1. All vertical boundaries are considered to be periodic. The flow in the Couette flow is driven by the interface interaction with the Poiseuille flow atop, where the interface will be reffered with the symbol Γ. Here, the interface will be considered horizontal which corresponds to cases where wave interaction can be considered negligible, the example of gravity waves with very low wave slope, or cases of developed surface waves. Other cases, as very high surface tension between the fluids are not considered valid as suppositions.

The lower of the subdomains, that corresponding to the shallow water channel, has

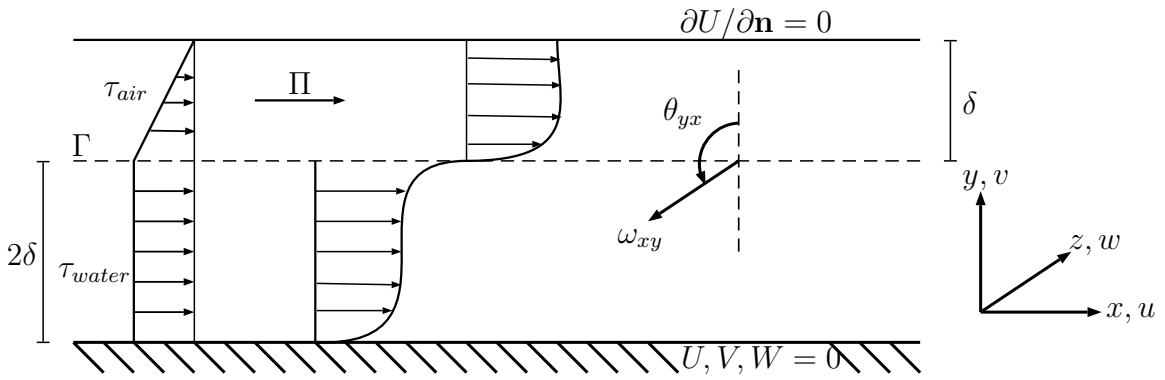

Figure 4.1: Definition sketch of the coupled Poiseuille-Couette flow. The Poiseuille flow is driven by a constant pressure gradient Π. The non-empty intersection between the subdomains, Γ, represent the flat interface.

dimensions of $4\pi \times 2 \times 2\pi$, and the grid is vertically refined near the interface as to guarantee enough resolution of all relevant scales. In the upper subdomain, or the air side, the domain has dimensions of $4\pi \times 1 \times 2\pi$. The viscous lengths of both channels are chosen to be equal, thus the shear based *Reynolds* number is set to be $Re_\tau = u_\tau \delta/\nu = 171$ on both subdomains. Setting Re_τ equal on both subdomains have implications on the properties of the comprising fluids if one wants to draw a direct comparison with real-case scenarios. In Table 4.1, the properties of the comprising fluids as needed for the assumption made to be true are shown. Such conditions on the properties of air and water are not limiting since one is not bound to interpret the results solely based on the properties of the comprising fluids, but turbulent features common to *sheared flows*.

Table 4.1: Properties at $T = 320\,K$ for the comprising fluids.

	Grid Dimensions	Density (m^3/s)	Kin. Visc. $(\times 10^{-6}\, m^2/s)$	Dyn. Visc. $(\times 10^{-6}\, kg/m \cdot s)$
Air (Upper)	$128 \times 96 \times 96$	1.08	18.11	19.62
Water (Lower)	$128 \times 96 \times 96$	988.92	0.57	56.60

The numerical approach followed for this kind of flow seeks to solve the incompressible Navier-Stokes equations numerically, where the compatibility conditions between the comprising Couette-Poiseuille flows are enforced explicitly. The detailed description for the numerical integration of the governing equations were given in Chapter 2.

4.2 Mean Features of the flow

4.2.1 Mean velocities, Reynolds Stress, and TKE Budget

The statistics herein obtained are made over a time of 159.5 eddy-turnover periods, where samples are taken every 1.1 periods. After reaching convergence and before taking samples the simulation is let to run for 10 turnover times. The averaging process, given the horizontal spatial homogeneity of the flows, will imply an ensemble averaging in the (x, z) directions and in time, unless otherwise indicated. Thus, the fluctuating variables will be described as

$$u'(x, z, y) = \overline{u}(x, z, y) - \langle \overline{u} \rangle (y)$$

A sum total of three boundary layers are formed in this case, which allow for a comparison that elucidates the role of the interface on defining the thickness of such layers. Two of these boundaries are contained in the lower sub-domain, where a Couette-type flow is expected. Figure 4.3b has the classic 'S' shape expected in these kinds of flows, although some differences are present. One such difference, also seen in Figure 4.3a, is the thinning of the boundary layers as a consequence of the increase on dissipation, due to the non-zero interface velocities, imposed by the upper subdomain. Such increase in dissipation can only be balanced by an increase in $\langle u'v' \rangle$ given that the production of turbulent kinetic energy should remain roughly similar to the one of a classic boundary layer. To show this, the integral balance of total shear stresses along the water column is written in the following form

$$\frac{\tau}{\rho} = \left(\frac{1}{\mathrm{Re}} \right) \frac{d\langle \overline{u} \rangle}{dy} - \overline{u'v'} \tag{4.1}$$

And is plotted in Figure 4.2b. Although qualitatively similar to canonical turbulent Couette flows, it has distinctive features not previously reported for this kinds of flows. In general, the cross axial Reynolds stress profile is not symmetric about the mid axis of the profile. Instead, due to the higher mixing the $\overline{u'v'}$ peak is slightly closer to the interface.

On the air side the total stress balance shown in Equation 4.1 is different. For the shallow channel, it is clear that $\tau = \langle \tau_\Gamma \rangle = \Pi_{\mathrm{air}}$. In other words, the pressure gradient driving the wind, by Newton's second law, must enter in balance with the total stresses in the water column. In Figure 4.2a, the integral balance is roughly equivalent to the balance found in literature for wall-bounded channels.

These redistribution of the Reynolds stresses are the main responsible for the increased mixing across the interface and, as it will be shown later, of the coupling of sweep-ejection

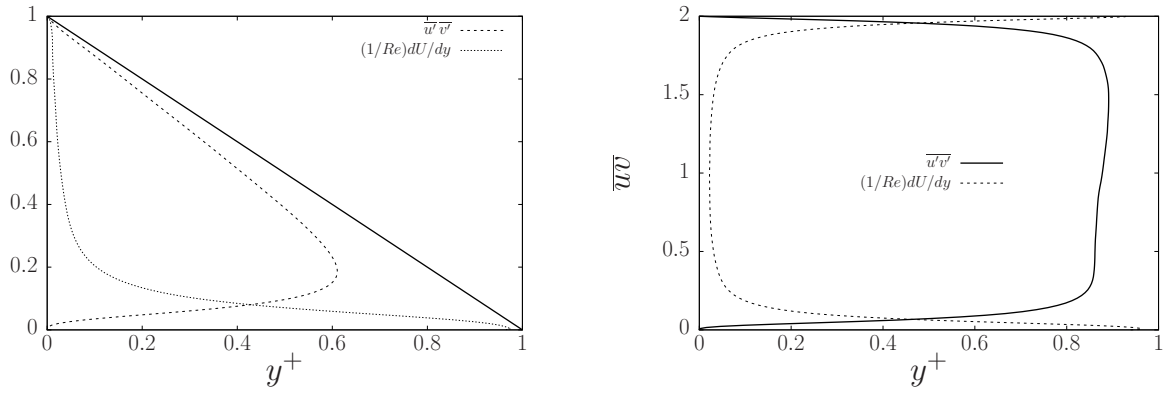

(a) (b)

Figure 4.2: Mean vertical Reynolds stress, $\overline{uv}$, profiles for the (a) air sub-domain, and (b) for the shallow channel.

events caused by near-interface coherent structures. It is important to note that the boundary layers have different thickness, being the boundary layer at the interface thinner, causing the profile to be non-symmetric at mid-height. Also, the streamwise velocity RMS although qualitatively similar to the results obtained by Liu et al. [28], Figures 4.3c and 4.3d show that the state of fluctuations are higher and slightly closer to the interface indicating an even higher degree of mixing on the shallow channel either close to the wall or close to the interface. Except for the near-interface/wall vertical RMS fluctuations, horizontal mixing is enhanced along the water column.

Additionally, the velocity fluctuation profiles here shown do not compare well with the ones obtained by Lombardi et al. [29] on the interface boundary layer on the shallow channel side, suggesting that turbulent mixing on the flow in the denser fluid is dependent on how it is driven and what boundary conditions are imposed to it. Note that the streamwise velocity fluctuations on the case of the shallow channel lack the plateau present in the canonical Poiseuille-Poiseuille or Couette-Couette case [21, 22, 28, 29], where its location indicates the separation between the viscous and the buffer layer.

However, the mean velocity profile and RMS of velocity fluctuations on the upper subdomain are quantitatively similar to wall-bounded flows. The velocity profile shown in Figure 4.3e, when made relative to the interface velocity U_Γ, is similar to canonical wall-bounded flows. On the other hand, Figure 4.3f is clear in showing that just slight quantitative differences are present in the air subdomain.

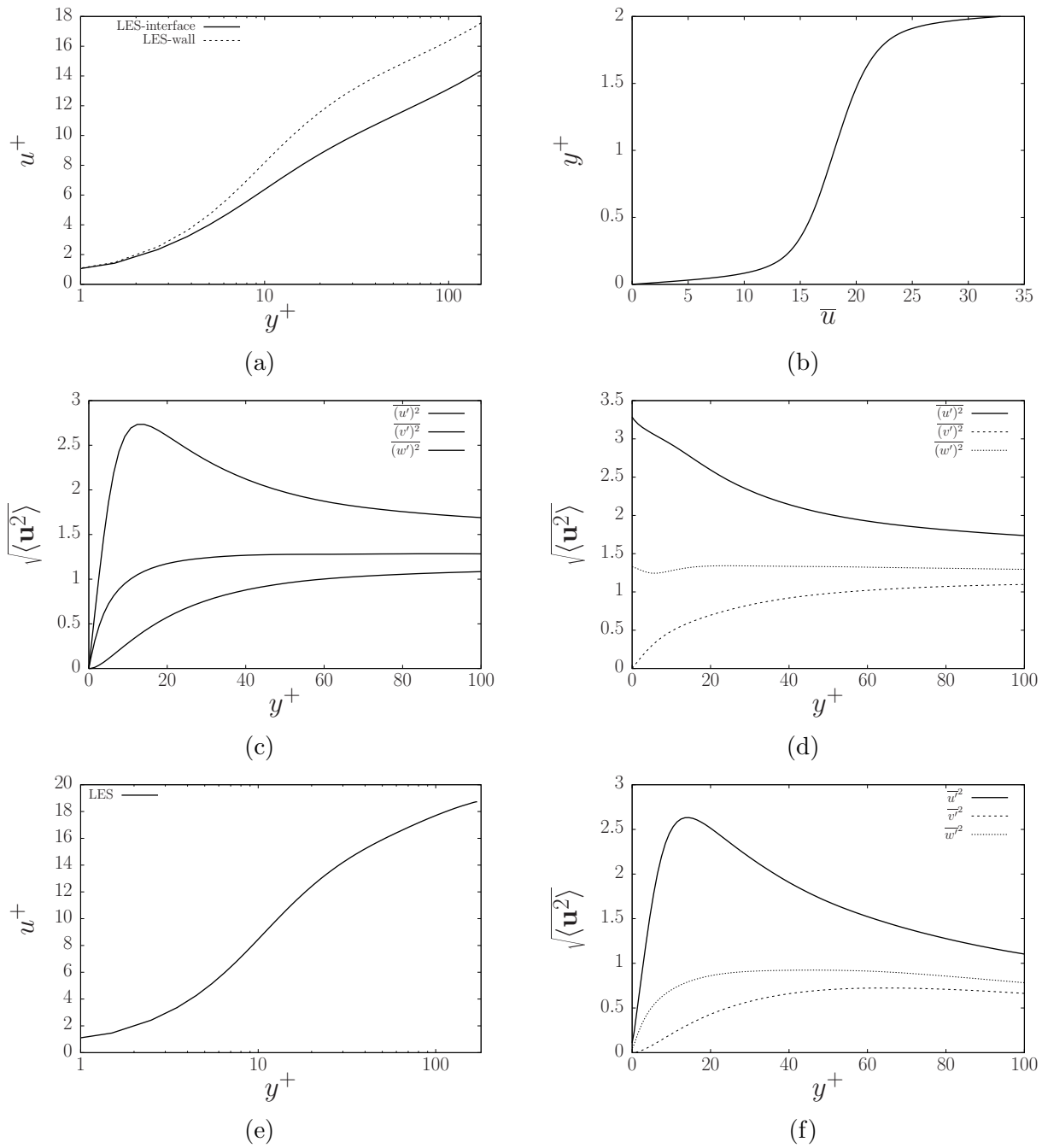

Figure 4.3: Mean vertical velocity and RMS profiles for the shallow channel and the air sub-domain. (a) semilog chart of mean vertical velocity profile of the upper and lower halves of the shallow channel, where the wall-like boundary layer correspond to the bottom half; (b) vertical velocity profile of the whole depth; (c) RMS velocity fluctuations for the upper half of the shallow channel; (d) RMS velocity fluctuations of the lower half of the shallow channel; (e) mean velocity profile in semilog chart for the air sub-domain, and (f) RMS velocity fluctuations in the air subdomain.

Turbulent kinetic energy budget

Now, the different terms in the turbulent kinetic energy, $k = \sqrt{u_i' u_i'}$ (TKE) evolution for the resolved scales can be written in the following manner:

$$\left\langle \frac{Dk}{Dt} \right\rangle = \langle P + \Pi_k + T_k + D_k + \epsilon \rangle = 0, \quad t \to \infty$$

$$\begin{aligned} P &= \overline{u_i' u_j'} \frac{\partial \overline{u_i}}{\partial x_j} \\ \Pi_k &= -\frac{1}{\rho} \frac{\partial \overline{p'\, u_i'}}{\partial x_i} \\ T_k &= -\frac{1}{2} \frac{\partial \overline{u_i' u_i' u_j'}}{x_j} \\ D_k &= \frac{1}{2} \frac{\partial^2 \overline{u_i' u_i'}}{\partial x_k \partial x_k} \\ \epsilon &= -(1/Re) \overline{\frac{\partial u_i'}{\partial x_j} \frac{\partial u_i'}{\partial x_j}} \end{aligned}$$

These terms, in the order presented above, receive the name of production, pressure diffusion, turbulent transport, turbulent convection, and dissipation of TKE.

In Figure 4.4, the kinetic-energy balance profiles are shown for the different boundary layers present in the system. In the shallow channel side, Figure 4.4a shows that near the interface dissipation is not only balanced by viscous diffusion, like in channel flows, but it is also balanced by the turbulent convection term. The similar contributions of the near-interface turbulent transport terms, which are the viscous diffusion and turbulent convection, mark a departure from canonical wall-bounded turbulence and indicate a heightened mixing on a thinner boundary layer, due to the rather short span in which these two terms vary ($y^+ < 2$). Compared to Figures 4.4b and 4.4c, the peak of TKE production and viscous dissipation are slightly closer to the origin, and dissipation shows a peak at $y^+ \approx 3$.

4.2.2 First and second order statistics for Vorticity

The coupled interaction between the fluid flows have as a consequence a non-zero contribution of interface-normal (vertical in this case) vorticity, by virtue of the kinematic condition described in Equation 2.6. In Figures 4.5c and 4.5d, a discontinuity in the mean spanwise vorticity component at the interface is present, and vorticity on the boundary is higher on the air side. The RMS of vorticity fluctuations are shown in Figures 4.5a and 4.5b, where after normalization by ν/u_*^2 show a slight discontinuity at the interface berween the shallow channel and the air side. The interface on the air acts similar to a wall-bounded case and

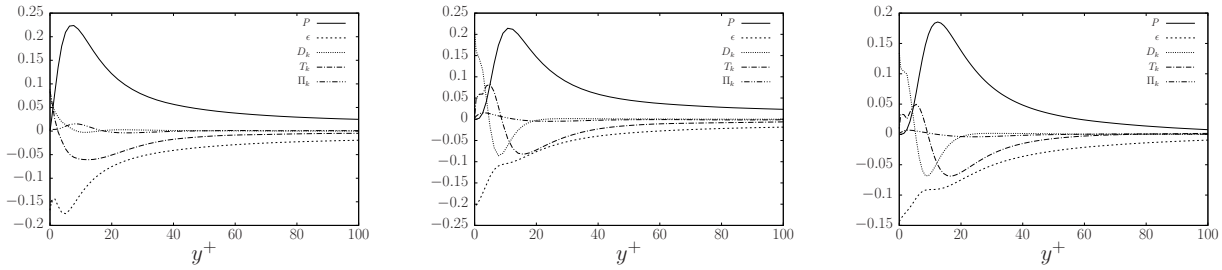

(a) (b) (c)

Figure 4.4: Profiles of TKE in the shallow channel for (a) the interface boundary layer, (b) the wall boundary layer, and (c) the interface boundary layer on the air side.

can be verified in Figure 4.5a. As in the case of a turbulent Poiseuille flow, the streamwise vorticity shows a local maximum at the boundary from where it decreases to a minimum near $y^+ \approx 10$. The pioneering work of [20] theorized a streamwise vortex model as to the responsible of such variation. In the opposite side of the interface, as seen in Figure 4.5b, both the streamwise and the vertical vorticity fluctuations show the aforementioned behavior suggesting a model of inclined vortices acted by opposing streamwise and vertical vorticity. Previous works [28] have shown that similar results, but where the discontinuity of vorticity seems to be attributed to the use of *different* Reynolds numbers. Mathematically, there is no direct constraint on the continuity of vorticity at the interface, except when the comprising fluid have the same density, as it can be shown by taking the curl of condition 2.6

$$\overline{\omega_y}_{\text{air}} = \sqrt{\frac{\rho_{\text{water}}}{\rho_{\text{air}}}} \left(\frac{\partial w_{\text{water}}}{\partial x} - \frac{\partial u_{\text{water}}}{\partial z} \right) = -\sqrt{\frac{\rho_{\text{water}}}{\rho_{\text{air}}}} \overline{\omega_y}_{\text{water}} \tag{4.2}$$

4.2.3 Higher order statistics on the shallow channel

The flatness factor of the fluctuating velocities (u', w', v') in the shallow channel are presented in Figure 4.6. The intermittency of streamwise velocity fluctuations, or kurtosis, at the interface boundary layer is lower than 3, point from which it decreases more until it arrives to a minimum at $y^+ \approx 5$ from where it starts to increase until reaching a maximum at $y^+ \approx 40$. Unlike wall bounded turbulence the peak of spanwise and vertical flatness factors are not at the boundary, and the latter shows not one but two loci of maxima. Regarding the maximum closest to the interface, the increased spanwise intermittency provided by the interface is met with increased dissipation in the near-interface region. Note that the maximum farthest from the wall roughly coincides with the height of maximum turbulent production, $y^+ \approx 10$, in wall boundary layers. In the following sections, the turbulent kinetic energy profiles will be presented which will reinforce the aforementioned notions. In the case of the wall, shown in Figure 4.6b, the profiles are qualitatively similar to those of wall-bounded channels, except

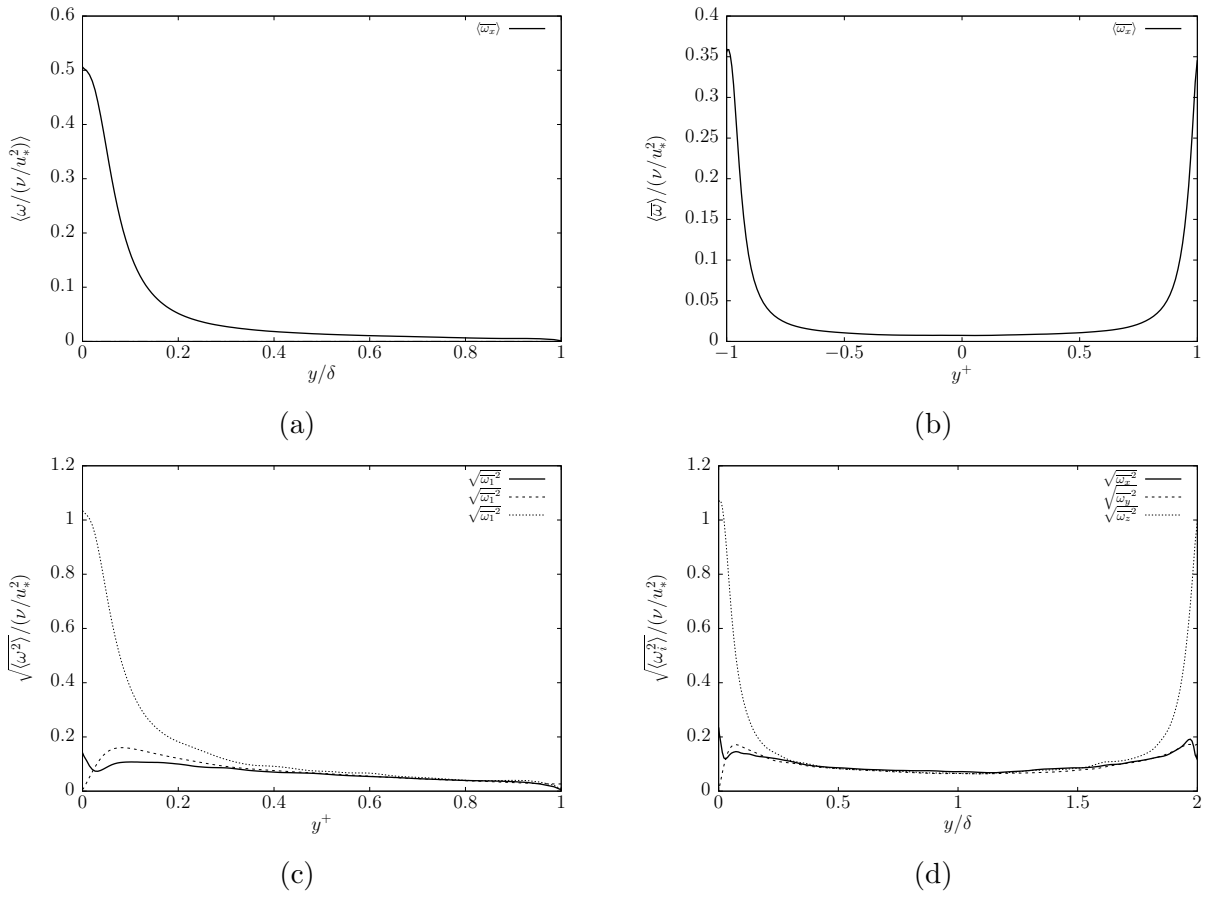

Figure 4.5: Mean vorticity vertical profile on (a) the air side, and (b) the shallow channel. Vorticity RMS profiles on (c) the air side, and (d) on the shallow channel.

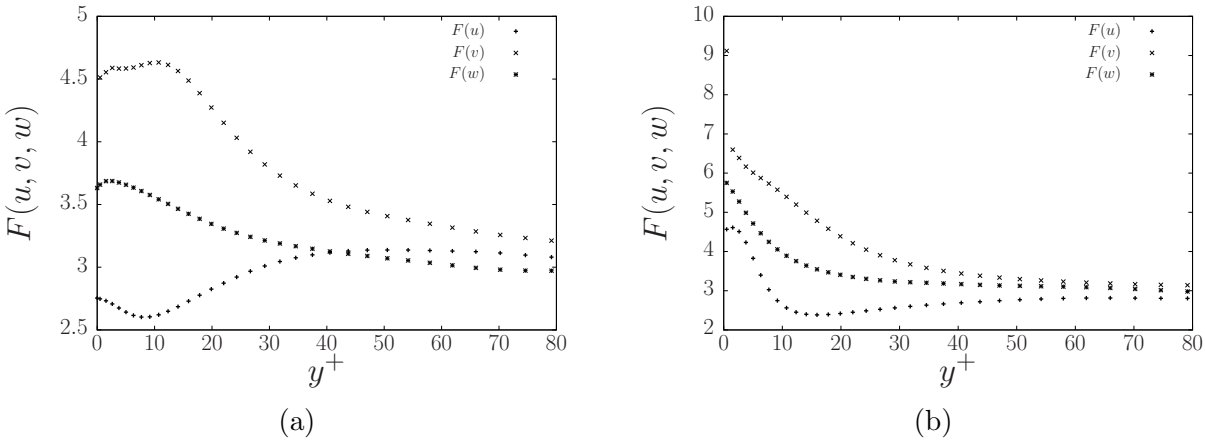

Figure 4.6: Mean vertical flatness on (a) the interface boundary layer on the shallow channel, (b) the wall boundary layer on the shallow channel.

that a higher state of streamwise and spanwise velocity fluctuations are present in the viscous region. Such increase in spanwise and vertical intermittency compared to turbulent Poiseuille

flows has been shown for Couette flows [5]. Notice that the present flow in the shallow channel is not *per se* a Couette flow, not even the skew-symmetry of the flow is conserved along the mid-plane, thus any contrast with the latter has to be assumed qualitative in nature.

4.2.4 Two-point correlations

The two-point temporal correlation coefficients of the streamwise velocity fluctuation, u, is determined using the following estimator

$$R_{uu}(\mathbf{x},t) = \frac{1}{N}\sum_{j=1}^{N} \frac{u(\mathbf{x},t)u(\mathbf{x},t+j\Delta t)}{(u_{\mathrm{rms}})^2} \tag{4.3}$$

In Figure 4.7 the two-point correlation for the sum $R_{uu} + R_{vv} + R_{ww}$ is presented for horizontal planes located at heights $y^+ = 8.65$ measured from the nearest boundary parallel to such plane. Previous works on Couette flows [5, 26] have used this technique to determine the 'marginality' of the outer spatial scales for the simulation. Such marginality was described as the possibility of obtaining two different turbulent flow realizations: 'periodic' or 'disordered', depending whether large-scale structures have 'sufficient room' to develop. In this particular work, horizontal scales were chosen to be at least double of those used in recent DNS experiments [12, 24, 28, 29]. In spite that, Figures 4.7a and 4.7b show open positive correlation contours crossing the periodic boundaries indicating the solution to be on the so-called 'periodic' state. However, notice that the length of the time-averaged correlations is larger near the interface.

4.2.5 Reynolds Stresses: Quadrant analysis

The results shown in the previous section indicate that the state of velocity fluctuations in the shallow channel is increased by the interaction of such flow with a pressure-gradient-driven air flow on the upper boundary of the channel. Such increase in horizontal mixing, passed all the way to the lower wall of the shallow channel, induce the increase in turbulent quadrant events present in the flow.

The resolved Reynolds stress quadrants in the shallow channel and air side shown in Figure 4.8 present important qualitative differences when compared to canonical results [36]. In the air side, or Figure 4.8c, the shape of the curves are very similar to wall-bounded turbulence, despite the clear difference in the actual values due to the spanwise under-resolution of the simulation. For the case of the interface boundary layer, or Figure 4.8a, the $\overline{uv}$ intensity of sweep and ejection is not as strong and the separation of the lines is reduced almost in half at $y^+ = 2$. Although gradient- and counter-gradient interaction events (Q1

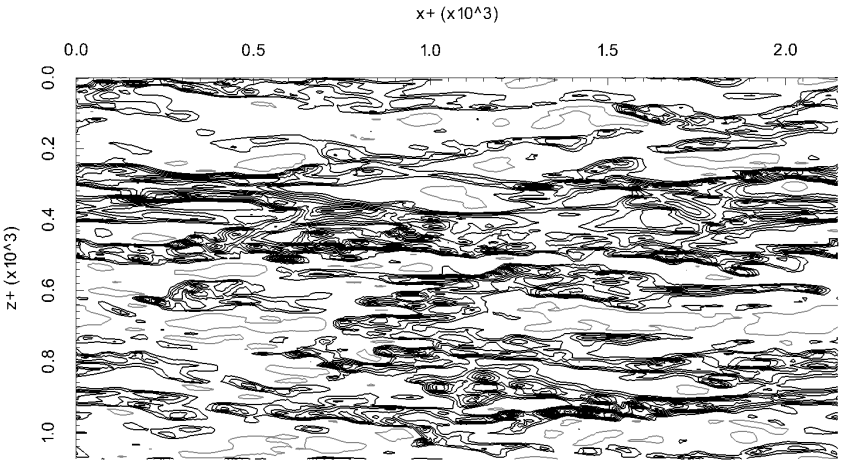

(a)

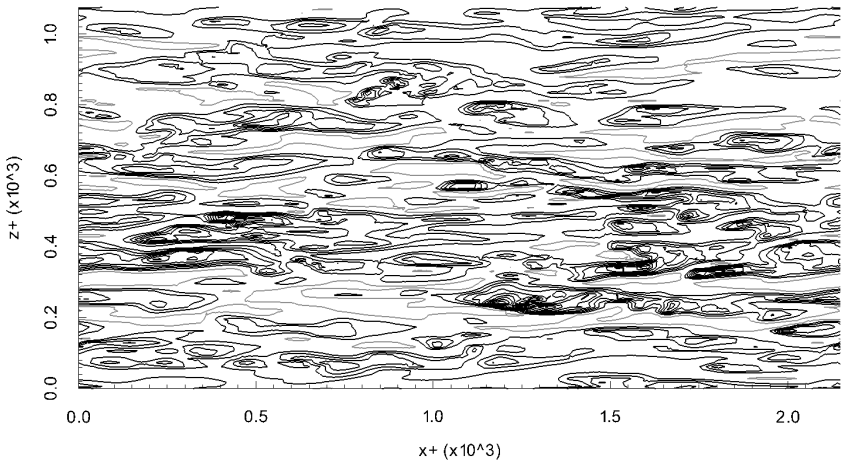

(b)

Figure 4.7: Contours, on 0.2 intervals, of two-point velocity correlation coefficient $\sum R_{uu,vv,ww}$ on the horizontal plane $y^+ = 8.65$ off (a) the interface, and off (b) the wall. The light gray contours represent negative correlation coefficients.

and Q3) are not important for turbulence, it is interesting to note that the crossing between the profiles at $y^+ \approx 2$ is not there anymore. However, the Q2-Q4 crossing at $y^+ \approx 10$ found in wall-bounded turbulent flows is also present. In the case of the shallow water wall, or Figure 4.8b, turbulent intensities are in general greater compared to the air side specially sweeps and ejections. The latter phenomenon implies that the higher mixing introduced by the presence of the interface induce to weaker ejection-sweeps on the interface boundary layer and, at the same time, lead to stronger sweep-ejections on the wall.

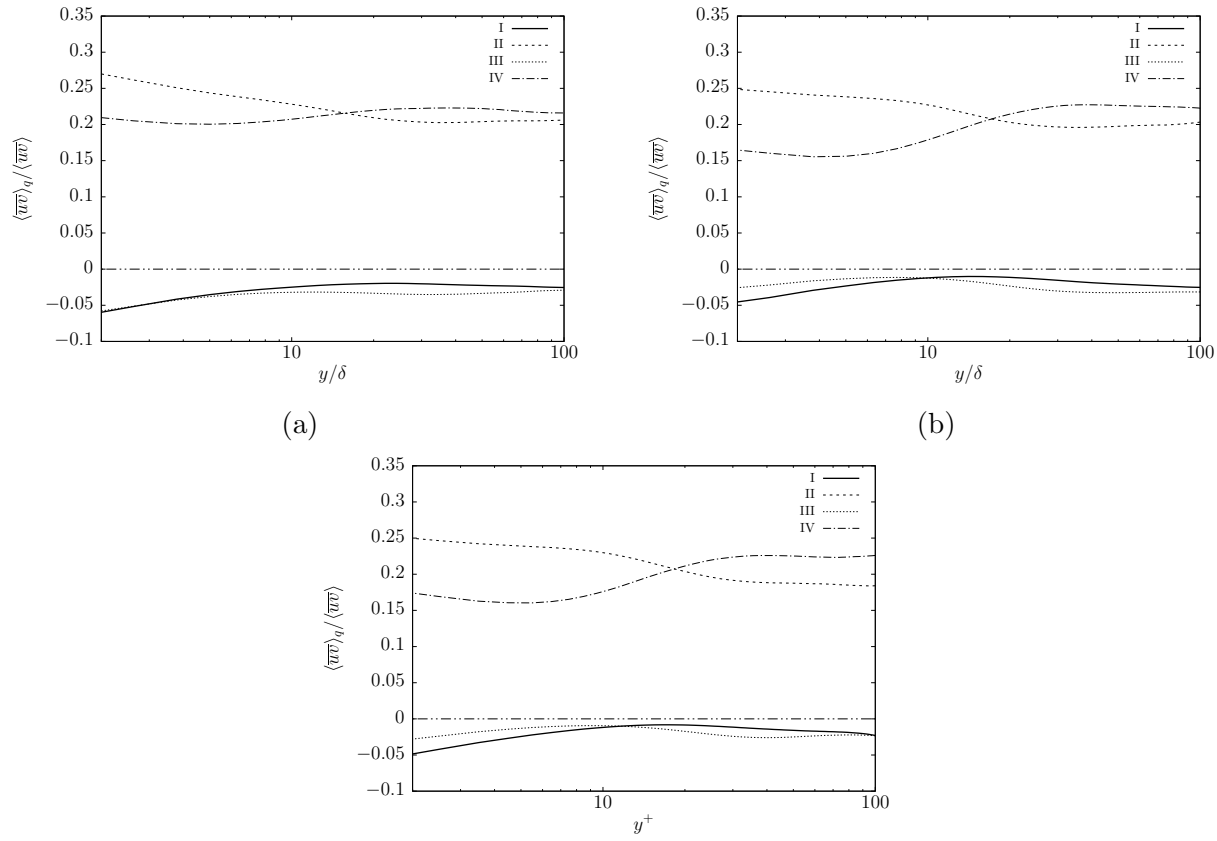

Figure 4.8: Quadrant analysis profile of $\overline{u'v'}$ events on the shallow channel for (a) interface boundary layer, (b) wall boundary layer, (c) and for the air boundary layer.

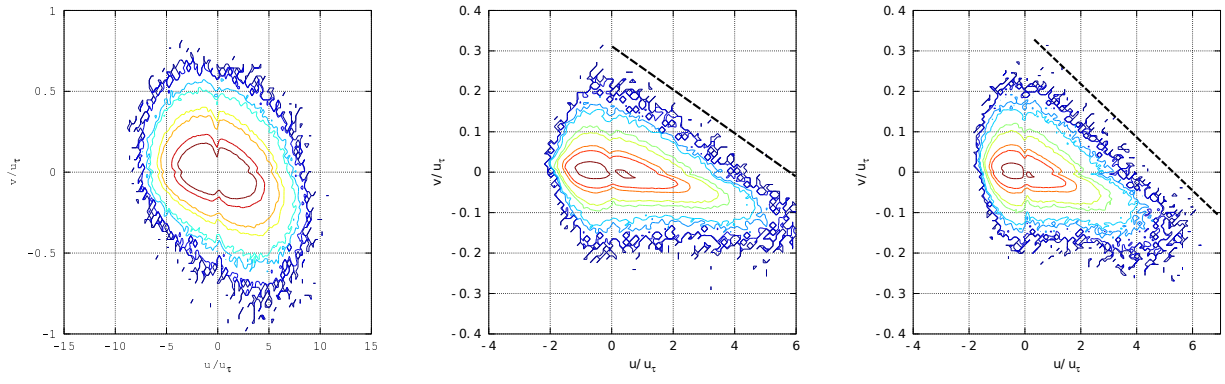

Figure 4.9: Joint probability function distribution $P(u, v)$, at height $y^+ = 2$, on the (a) air side near the interface, (b) on the shallow channel close to the interface, and (c) on the shallow channel close to the wall. The contours are log-scaled from 10^{-6} to 1.

Reynolds Stresses: Strong Quadrant Events

In the previous section, the results obtained using the quadrant analysis as proposed by Willmarth and Lu [48] hides point-by-point details lost in the averaging process. Furthermore, as indicated by Lombardi et al. [29], by selecting only signals that are considered as strong one can obtain a more precise account of the degree of Reynolds stress coupling can be studied. The exact definition of 'strong' is based on the spatial coherence of the said signal along the vertical. More importantly, the detection of such signals can be associated to the instantaneous interface shear stress, $\tau' = \nu(\partial u'/\partial y)$, where it is expected large backflow velocities to increase backflow shear stress events. Anyway, the method proposes to:

- Select three equally spaced probes on the vertical, for every (x, z) location, in the near interface region ($y+ < 5$) on either side of the interface
- Whenever the velocity fluctuations on all three probes lay on the same quadrant, record the "Strong" event, along with the fluctuating velocities on the probe farthest from the interface, and record the corresponding interface shear stress in the (x, z) location.

In this work, the heights are chosen to guarantee the detection of the strong events to be in the viscous region, that is at $y^+ = (0.5,\ 1,\ 2)$ from the interface or wall. The velocity fluctuations recorded at height $y^+ = 2$ can be used to calculate the mean Reynolds stress using the following equation

$$\langle \overline{u'v'} \rangle_{(x,z)} = \int_{-\infty}^{+\infty} u'v' P(u', v')\, du'dv' \tag{4.4}$$

Where $P(u', v')$ is the joint probability function of the fluctuating horizontal velocities. In Figure 4.9a, a weak correlation between rare negative vertical velocity events, and positive horizontal velocity events are detected on the near-interface region in the air side. The occurrence of rare splat events are indication of increased mixing and transfer across the interface.

On the other hand, the interface boundary layer on the shallow channel shows a stronger correlation of rare vertical-to-horizontal velocity fluctuating events as indicated in Figure 4.9b. A linear correlation between rare high-speed horizontal and vertical velocity events is shown by the dashed line on the aforementioned figure. The cutoff line, represented by $v' = 0.3\, u_\tau - 0.05\, u'$, shows the connection between rare splat events and rare high-speed u' fluctuations. Similarly, Figure 4.9c shows a linear correlation depicted by the dashed line $v' = 0.34\, u_\tau - 0.06\, u'$. The respective slopes of the lines just mentioned indicate the direction in which passive tracers are 'ejected' by strong rare events along the vertical plane.

Note that in the case of the interface boundary layer in the shallow channel, the angle is $\alpha_{\text{strong}} = 3°$, and for the wall boundary layer is $\alpha_{\text{strong}} = 3.5°$. Additionally, high-probability 'strong' JPDF events ($P(u', v') > 0.01$) have no slanting angle with respect to its major axis indicating that these do not contribute to the ejections of passive tracers.

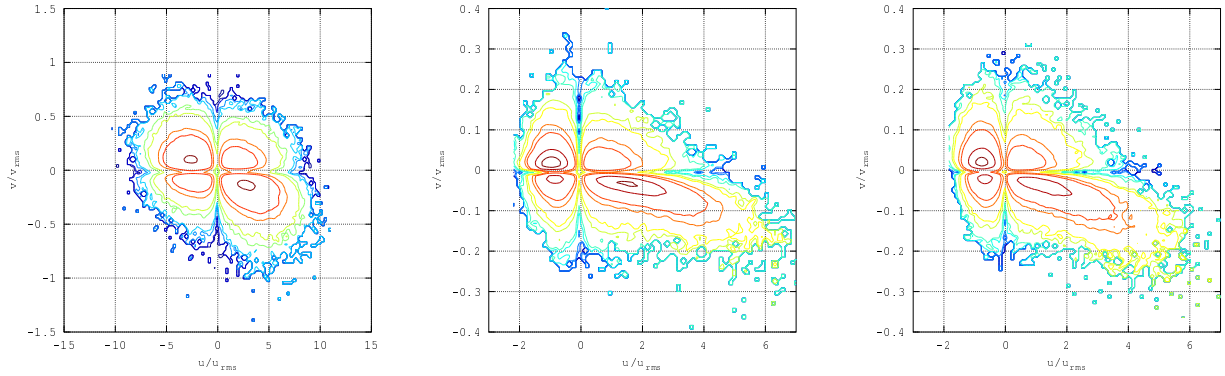

(a) (b) (c)

Figure 4.10: A covariant integrand distribution, at height $y^+ = 2$, on the (a) air side near the interface, (b) on the shallow channel close to the interface, and (c) on the shallow channel close to the wall. The contours are log-scaled from 10^{-6} to 1.

A more detailed account on the analysis of quadrant events at height $y^+ = 3.0$ can be made by plotting the so-called covariant integrand of Equation 4.4, or $u'v'P(u', v')$. In Figure 4.10a, the quadrant analysis shows that the highest probability events are 'strong' ejections and sweeps, and no particular correlation rare Reynolds stress events and velocity fluctuations is apparent. On the other hand, Figure 4.10b and 4.10c show a strong correlation between high-speed horizontal and negative vertical velocities, and rare Reynolds stress sweeps.

Finally in order to analyze the correlation between rare towards-the-wall/interface vertical velocity fluctuations and high-speed horizontal velocity fluctuations, a JPDF of pressure fluctuations versus vertical velocity fluctuations should indicate whether such phenomena is associated to splats, or intermittent near-interface or wall jets. Figure 4.11a shows that for the air side extreme rare negative velocities are associated with high, 'rapid' pressure fluctuations, typical of rare splat events. Also, for the case of the wall in the shallow channel Figure 4.11c rare splat events are present. On the contrary, the near interface region on the shallow channel shows no particular correlation between extreme positive pressure and negative vertical velocity events, as depicted in Figure 4.11b. The latter is an indication that vertical mass transfer across the interface on the water side does not have splat events as its main mechanism [17].

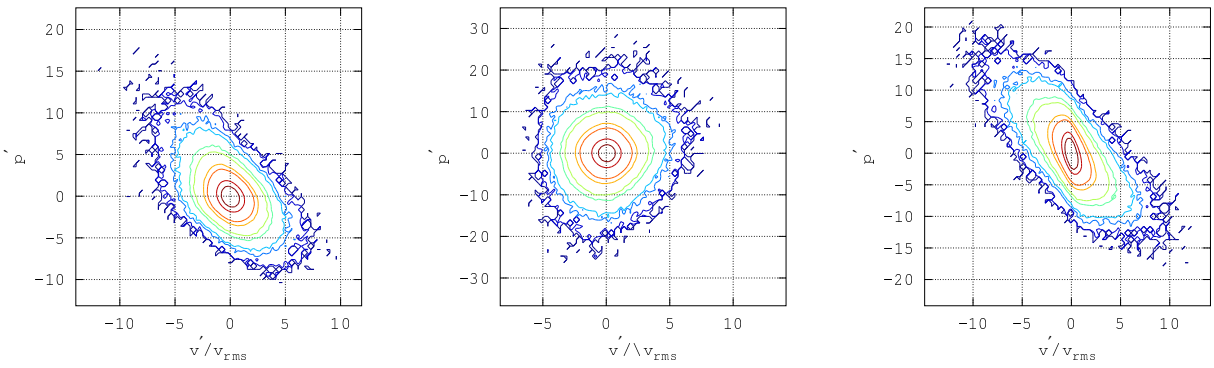

(a) (b) (c)

Figure 4.11: A JPDF of vertical velocity and pressure fluctuations, at height $y^+ = 2$, on the (a) air side near the interface, (b) on the shallow channel close to the interface, and (c) on the shallow channel close to the wall. The contours are log-scaled from 10^{-6} to 1.

Reynolds Stresses: Anisotropy Invariant Map (AIM)

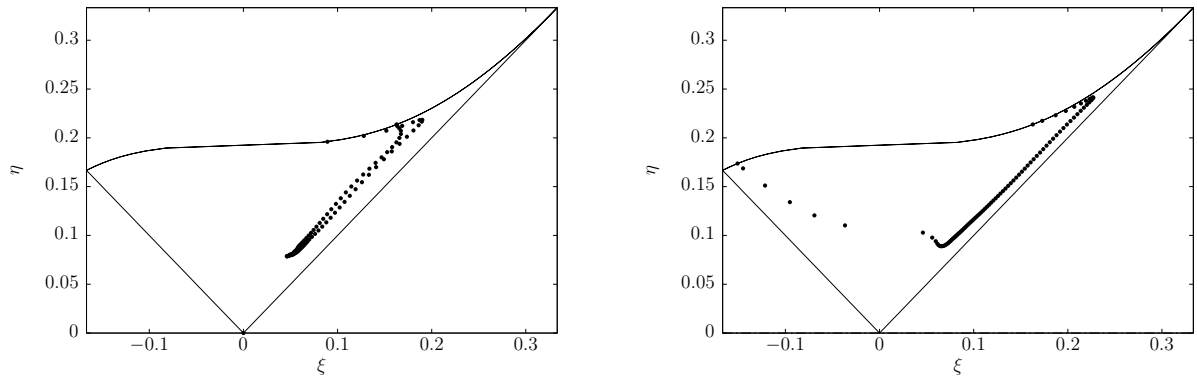

(a) (b)

Figure 4.12: Lumley triangle for the flow in (a) the shallow channel, and (b) the air side.

Figure 4.12 shows a map of the Lumley invariants for the flows on the air side and the water side. That is, the second and third invariants of the anisotropy tensor are plotted and must lie within a region (enclosed by the solid lines in the Figure) of all realizable states of the *Reynolds stress* tensor. Note that the second invariant $\eta = II^{1/2}$ is a measure of the anisotropy of the tensor, and the couple $(\eta, \xi = -III^{1/3})$ measures the shape of the tensor. From previous discussions it should be clear that on the air side it is expected a behavior similar to that of a wall-bounded boundary layer, whereas on the water side it is expected to have a Couette-type boundary layer. On the air side, the AIM map shown in Figure 4.12b indicate three basic states of the *Reynolds stress* tensor: (1) a two-component shape, where $\overline{u}\,\overline{u} \approx \overline{w}\,\overline{w} >> \overline{v}\,\overline{v}$, from the points that lie close to the wall, depicted in the

plot as those lying on the upper side of the triangle; (2) an axisymmetric shape along the streamwise direction where $\overline{u}\,\overline{u} >> \overline{w}\,\overline{w} \approx \overline{v}\,\overline{v}$, seen in the graph as the points that lie on the right side of the invariant map; and (3) an in-between disk-like shape and two-component axisymmetric shape in the spanwise direction, where the latter shape dominates as one gets closer to the free-slip boundary. These results, although not unexpected, have not been reported before, and as such enforce the idea of wall-like behavior on the air side. On the water side, things are quite different: (1) a two-component shape of the stresses where $\overline{u}\,\overline{u} \approx \overline{w}\,\overline{w} >> \overline{v}\,\overline{v}$ is detected close to the boundaries, depicted as the ends of the curve; and (2) in the middle of the channel a rod-like shape of the stresses is obtained. The one-to-last result goes in contrast with canonical results shown in literature [36]; that is, in Couette flows acted by a shear stress or a constant velocity have a state of the Reynolds stresses that lie very close to the one-component shape, on the upper right-most corner of the AIM map. This is characteristic of all wall-bounded boundary layers, where $\overline{u}\,\overline{u} >> \overline{w}\,\overline{w} \approx \overline{v}\,\overline{v}$. Thus, the $\overline{w}\,\overline{w}$ passed across the interface with the air interfere greatly with the state of the $\overline{u_i}\,\overline{u_j}$ tensor and it persist along the vertical, even in the vicinity of the lower wall.

4.2.6 Near-interface Flow Structures and Coupling

Coherent flow structures are investigated using different eductions techniques in order to get an appropriate qualitative description of these under the perspective of LES. Figure 4.13 show the streaky structures represquadrantAnalysisented by the low-speed (negative) fluctuations of velocity over different horizontal planes. As mentioned before, less elongated inclined structures produced close to the interface in the water side are responsible for enhancing mixing across the interface [22, 43], and across the water column; these structures are seen in Figure 4.13b, where these become less distinctive and chaotic compared to its wall counterpart shown in Figure 4.13c. On the air side, the low-speed streaks are more elongated and present a more organized structure when seen along with the vortex cores, as shown in Figures 4.13a. The case of the wall, presents similarities to the scenario just described, but given the apparent interaction between the boundary layers in the shallow channel one should expect the presence of inclined impinging vortical structures coming from the interface all the way through the near-wall region. It is apparent that near-interface motions on the air are dominated by the structures produced near the interface on the water side.

The streaks formed at either side of the interface are roughly of the same streamwise dimensions $x^+ \approx 800$, but its persistence along the vertical is higher on the air side. From the work of Liu et al. [28] it was concluded that, due to the use of different *Reynolds Numbers* on either sub-domain, larger structures are present on the water side. These structures,

nevertheless, pass to the air side due to the coupled interaction and seem to persist, to stretch, and strengthen along the vertical; which goes in contrast with the results obtained in the aforementioned work.

Vortex eduction

Since the density of air is much less than that of water coherent structures on the water side tend to eject at a slower pace due to its higher inertia, thus reducing the degree of coupling that might be present between the coherent structures formed in the region close to the interface on the water and on the air. A vortex eduction technique, based on the second largest eigenvalue of the tensor $\overline{\mathbf{S}} : \overline{\mathbf{S}} + \overline{\mathbf{\Omega}} : \overline{\mathbf{\Omega}}$, is used in order to observe the degree of coupling between the vortex tubes and their organization. It is observed in Figure 4.14 that instantaneous interface-connected vortex cores populate the air-water region, although isolating such structures from non-connected ones is not trivial. Nevertheless, note that the interface-attached vortex cores on the water (yellow) side tend to be more slanted with respect to its air counterparts. These interface-attached vortices have been reported to happen sporadically in simulations of this type [21, 22, 28, 29], alongside with quasi-streamwise and hairpin vortices happening on either side of the flow.

Vortex inclination on the shallow channel

As mentioned in the previous section, the combined action of the instantaneous interface stresses and velocities increases vertical vorticity which, given the higher inertia of water, is more evident in the shallow channel. The observations made regarding the inclination of the instantaneous vortex cores are confirmed by histogram statistics of vortex inclination angles, as defined by Moin and Kim [34], and measured as shown in Figure 4.1. The histograms representing the projection of the vorticity vector in the xy-plane are shown in Figure 4.15b and 4.15d show a rather disparagingly different trends near the interface and near the wall, respectively. Near the interface θ_{yx} the interface-connected vortices have ranges between $(335°, 35°)$ and $(145°, 205°)$ but no modes corresponding to quasi-streamwise vortices are detected; on the other hand the histogram distribution on the wall side have a mode in the range $(260°, 280°)$, which correspond to quasi-streamwise vortices. Previous works have shown similar results [28], although they detected quasi-streamwise vortices' modes in the near-interface θ_{yx} histogram in the water subdomain.

4.3 Rare backflow events analysis

4.3.1 Backflow velocities and interface shear stresses

In previous sections, it was shown that the JPDF of streamwise-to-vertical velocities has a linear correlation of negative events. Such relation has a negative slope and, interestingly, the correlation span both positive and negative rare events ($P(u,v) < 10^{-4}$). Previous works in wall-bounded channels and pipe flows [27, 32] have shown that intermittent and rare backflow velocity events produce small separation regions (where $\tau_{\text{wall}} < 0$) in the boundary layer, which produce rare positive spots of wall-normal vorticity. As already seen, the coupling allows for the production of vertical vorticity in the near-interface region of the flow which, as seen in Figure 4.5b, is more evident in the shallow channel.

Figure 4.16 shows the distribution of fluctuating streamwise velocity and interface shear stress, $\tau' = \nu(d\,u'/d\,y)$, events presented in log-scale. Note that the distribution of rare velocities present a more organized structure in Figure 4.16a, where local backflow velocities are more common but rare positive events span a longer range; similar results were shown by Lenaers et al. [27]. On the other hand, Figure 4.16b resembles a gaussian distribution showing the little impediment that the air phase represents for the horizontal movement of the flow in question. Also, in the latter case backflow fluctuations spans a slightly larger range compared to the air counterpart. However the differences, rare backflow stress events dominate the interface as shown in Figure 4.16c although the distribution is positively skewed but centered around zero.

4.3.2 Vertical vorticity spots detected by VISA scheme

In order to visualize the spatial structure of vertical vorticity in the near-interface and near-wall region in the shallow channel, the Variable Interval Space Averaging technique of Blackwelder and Kaplan [6] was employed with some modifications. The VISA detects an event when the local variance of a variable ϕ is higher than some value. The variance is defined as:

$$\sigma_c(\phi, x, z, y, t, L) = \frac{1}{\langle\phi^2\rangle}\left[\frac{1}{L}\int_{-L/2}^{L/2}\phi^2\,dx\,dz - \left(\frac{1}{L}\int_{-L/2}^{L/2}\phi\,dx\,dz\right)^2\right] \tag{4.5}$$

Then a conditional averaging in time is carried out, in which a detection function is used for the process, and will be denoted with the symbol $\langle(\cdot)\rangle_c$. In this case, the detection of highly variable events occuring on regions of backflow are of interest. This represents a departure from the original VITA/VISA technique, where regions of negative increments of

velocity, or $\langle u(x_0 + \Delta x) - u(x_0)\rangle$, were used as an additional criterion for the detection of spanwise coherent structures. However, an averaging window of $2\,L = (\Delta x^+, \Delta z^+) \approx 170$ is used for the calculation of the conditional variance. The detection function is a field and as such is defined as:

$$\mathcal{D}(x, z, y, t) = \begin{cases} 1 & \sigma_c \geq 1.0, \quad \frac{du}{dy} < 0.0 \\ 0 & \text{otherwise} \end{cases} \tag{4.6}$$

In Figure 4.17 a plane located at $y^+ \approx 7$ containing contours of the conditionally-averaged vertical vorticity is show. Previous observations on wall-bounded channels [27] have shown that backflow events extend up to $y^+ = 4.5$, also these regions are accompanied by oblique vortices. In Figure 4.17a, large regions of positive vertical vorticity cover the plane. In principle small regions of positive vorticity, or 'islands', inhabit the near-interface region where, due to the interface velocity, they are convected away and coalesce with other regions of positive vorticity. In the region near the wall, the near-zero convection leaves the 'islands' almost stationary and, due to the weak occurrence of backflow events, the topology and number of such islands remain more or less constant in time.

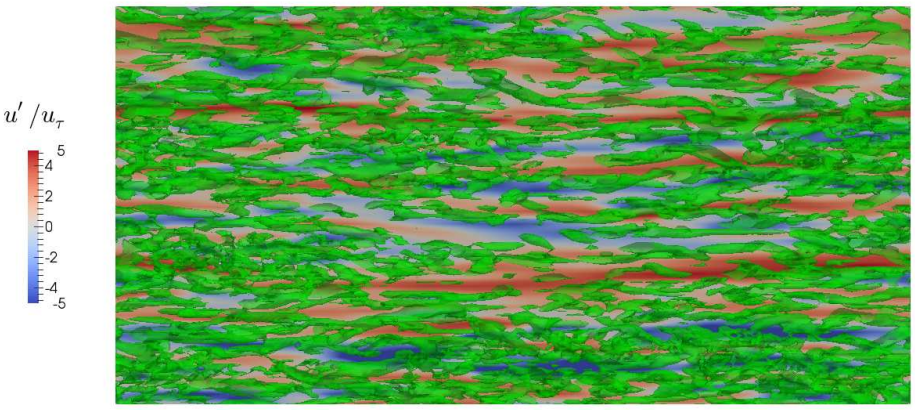

(a)

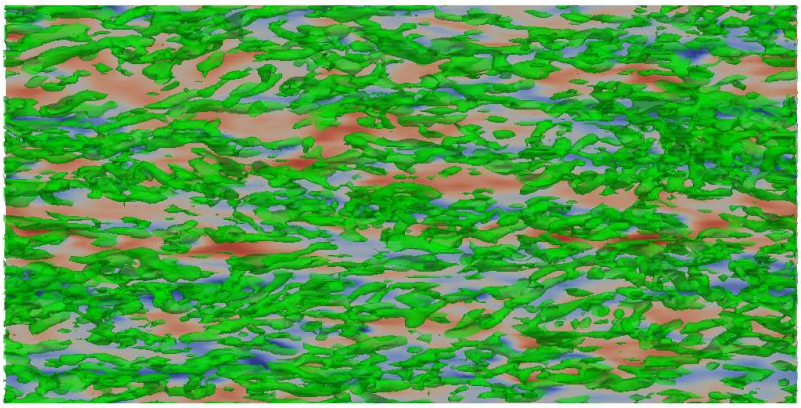

(b)

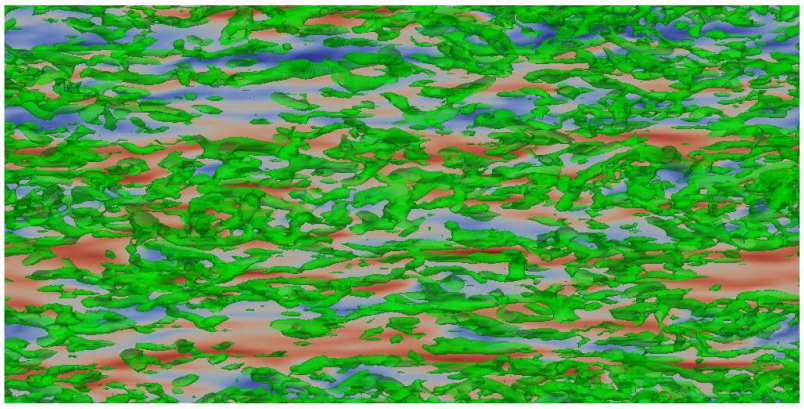

(c)

Figure 4.13: Contours of streamwise fluctuating velocities over horizontal plane taken at height $y^+ = 1.47$ off the interface/wall, and near-interface/wall coherent structures educed via λ_2 criterion. Plate (a) is taken from the air side, whereas plates (b)-(c) correspond to planes on the shallow channel taken close to the interface and to the wall, respectively.

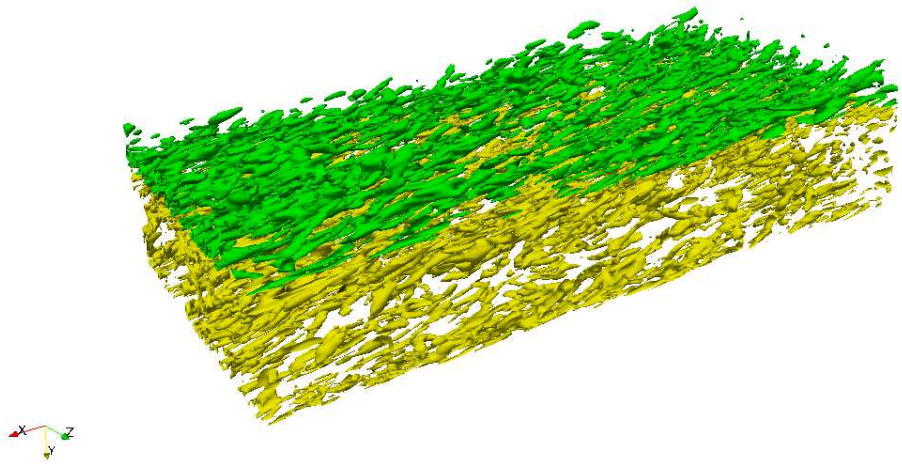

Figure 4.14: Iso-Surfaces of negative λ_2 on the system. The green colouring are from structures on the air side, whereas the yellow color are from the water side.

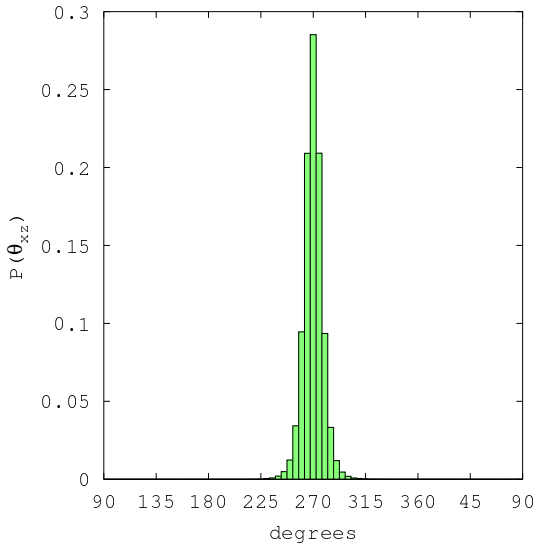

(a) Near-interface $y^+ \approx 1.47$

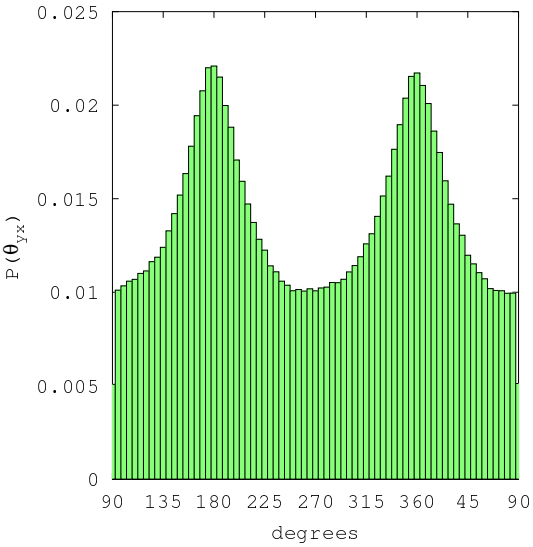

(b) Near-interface $y^+ \approx 1.47$

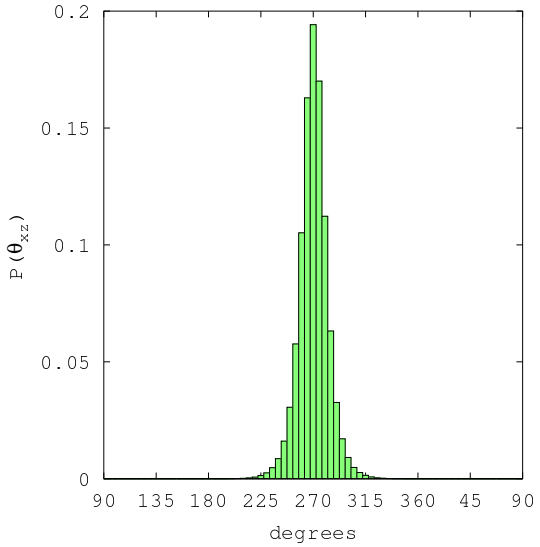

(c) Near-wall $y^+ \approx 1.47$

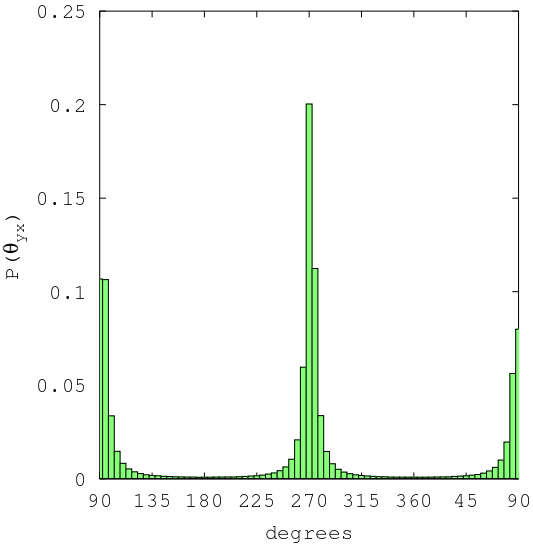

(d) Near-wall $y^+ \approx 1.47$

Figure 4.15: Histograms of near-interface two-dimensional vortex inclination angles (a)-(c) θ_{xz} and (b)-(d) θ_{yz} in the shallow channel.

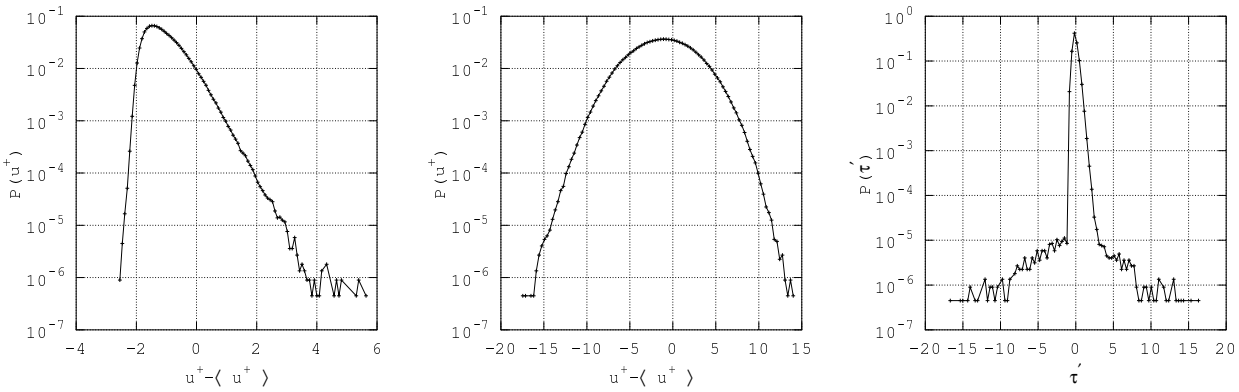

(a) (b) (c)

Figure 4.16: Distribution of streamwise velocity events at $y^+ = 1.47$ off the interface at (a) the air domain, (b) on the shallow channel, and (c) interface shear stress.

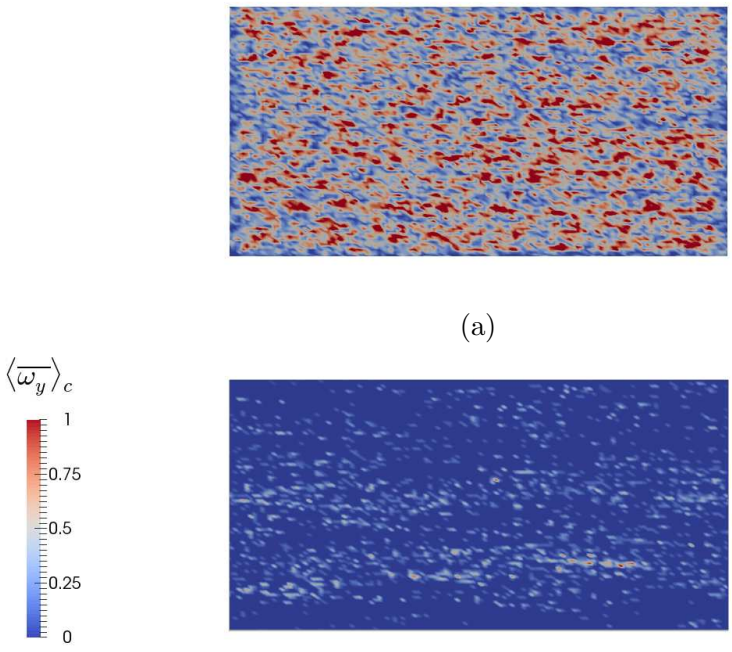

(a)

(b)

Figure 4.17: Conditional plane averaging of $\langle \overline{\omega}_y \rangle_c$ at $y^+ = 6.84$ off (a) the interface, and off (b) the wall in the shallow channel.

Chapter 5

Sheared flow around wall-mounted cylinders crossing an air-water interface: applications

In the present chapter, a LES over a surface-mounted square cylinder crossing the interface between two highly stratified fluids, like air and water, is performed. The aim of this study is then to analyze the coupling, increased shear, and overall effect that the interface has over the coherent structures and its interaction with the coherent motions due by the presence of the obstacle. It is thus expected that weak interactions between the near-interface shedding vortices on either side will couple and enhance mixing across the two fluid flows. Also, increased drag in the form of 'k'-roughness, due to to the partial-slip behaviour of the interface, and 'd'-roughness, due to the presence of the obstacle, is expected. Isolated bodies fully immersed in the inner region of a turbulent boundary layer are expected to modulate the integral length of the incoming coherent structures [35, 39, 45]. In principle, incoming vortex structures strengthens the horseshoe vortex produced by the obstacle by draining its energy, thus reducing its integral length.

The present work will attempt on elucidate the mechanisms present and estimate the deficit in statistical quantities due to both forms of roughness; that is, due to the interface and an immersed blockage. Emphasis would be given to the flow in the air side, where the obstacle is embedded only partially on the boundary layer.

In the first part of the chapter, flow around a circular cylinder completely immersed into the water subdomain, and only partially immersed on the air side, will be studied. In the air side, the obstacle rises up to the half-height of the channel, well within the outer region of the boundary layer. Special attention will be paid to the flow characteristics in the air side, where an analysis on how the anomalies caused wake generated by the obstacle extend

downstream and in the transverse. The first part concludes with a discussion about the properties of the flows with and without the presence of the cylinder in the air domain, but still with the cylinder fully immersed in the shallow channel.

The second part of the chapter flow around a square cylinder will be studied instead. Particular to this case is the height of the obstacle in the air side, which is chosen to be only 10% of the air's boundary layer. Here the obstacle is expected to behave as an isolated roughness element for the incoming boundary layer, instead as an immersed array of obstacles as it is expected from the former scenario.

5.1 Mathematical formulation of the problem

For the following simulations the incompressible, coupled, spatially filtered Navier-Stokes equations are integrated numerically as shown in Chapter 2, but for the modelling of SGS fluxes consequence of the filtering the *Dynamic Lagrangian Mixed* model [1] is used. Subsequent improvements described in [38] allow the study of flows over complex geometries by means of the *Immersed Boundary Method*, or IBM, which in the present work is used to represent the flow around the cylinders.

5.2 Incoming boundary layer: Inflow properties

For the inflow, we consider the canonical case of a turbulent Couette boundary layer (located at the liquid side) generated by the traction imposed by a Poiseuille turbulent boundary (on the gaseous side) layer at the interface between two fluids, as described in Chapter 4. Both of the simulations carried out in this chapter will be initialized and fed using instantaneous realizations of the Couette-Poiseuille flows taken from a streamwise-normal plane. A transport equation for the momentum fluxes on the outflow boundary is set in order to preserve the parabolic behaviour of the momentum equation at the outflow. Finally, the study will be limited to turbulent boundary layers with the same *Reynolds Number*, $Re_\tau = 171$, thus the results obtained in previous chapter will be used directly.

5.3 Flow around a circular cylinder: configuration and results

The geometry of the domain and the location of the cylinder is depicted on Figure 5.1, and follows that of Fröhlich and Rodi [11]. For simulation purposes, the domains are scaled

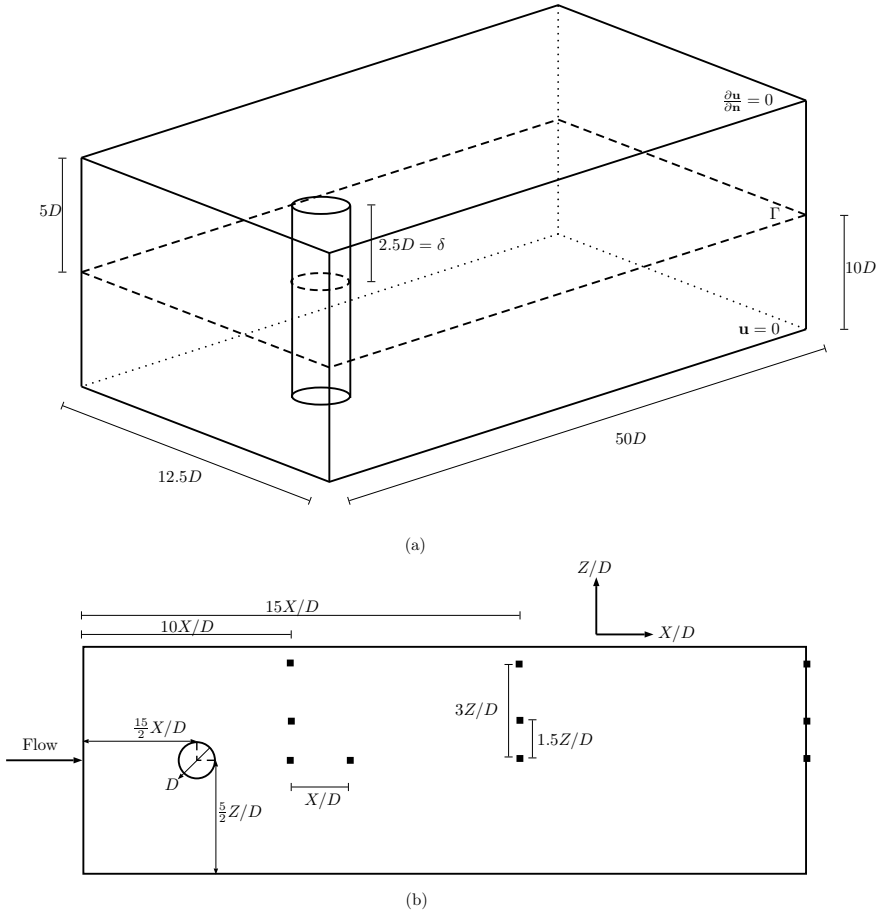

Figure 5.1: Domain sketch for the circular cylinder: (a) iso-parametric view, (b) top view.

using the half-height of the shallow water channel of the incoming flow, but for the purpose of presenting the results the data is scaled using the diameter of the cylinder. Notice that different monitor probes are immersed in the flow at the locations shown in Figure 5.1(b), where profiles for different flow quantities will be presented. The grid points used for each sub-domain (gas and liquid) were $256 \times 96 \times 96$, and apart from this the settings follow that of the input channel described previously. The height-to-diameter ratio for the cylinder in the air side is chosen to be 2.5.

Flow in the air domain

Figure 5.2 shows the structure of the recirculation zone formed behind the circular cylinder. At a first glance, three types of circulations are present: (1) a horseshoe vortex, (2) a tip vortex, (3) and a splat, where each of the aforementioned structures were labeled 'A', 'B', and 'C', respectively. The formation of the tip vortex and the splat are due to the passage of a high-velocity current at the tip of the cylinder that, due to mass conservation, washes down towards the bottom of the channel (the interface) clashing with a low-velocity

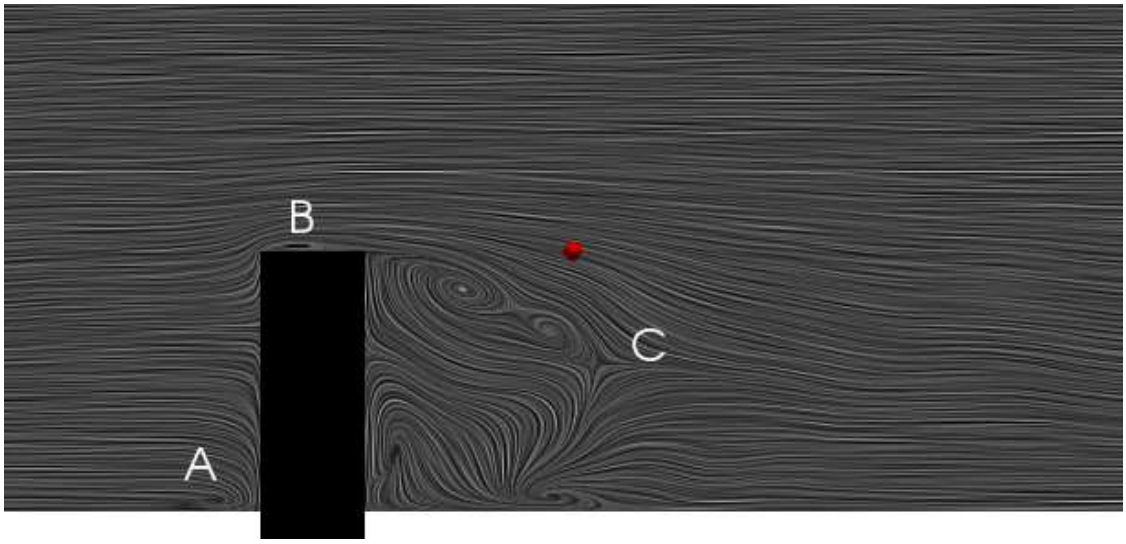

Figure 5.2: Vortex eduction via Lagrangian tracers on air side, at midplane. A: separation Vortex, B: Tip Vortex, C: Recirculacion and splat (Saddle).

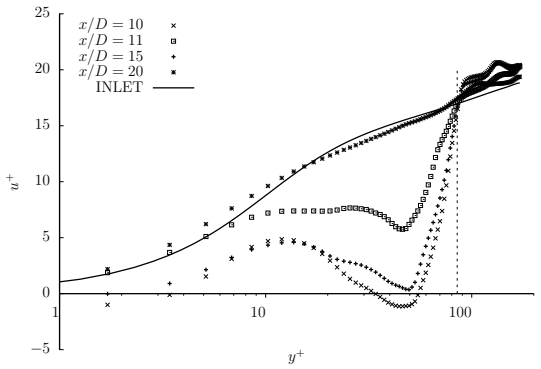

Figure 5.3: Mean velocity profiles behind the cylinder with zero offset.

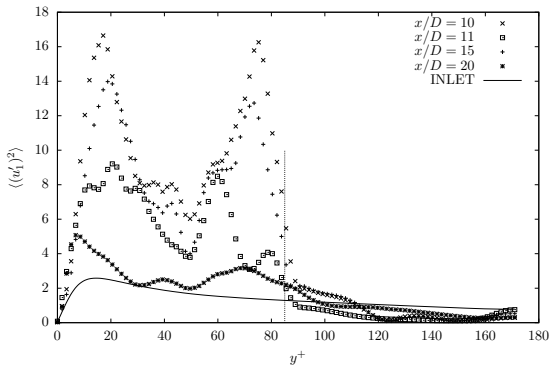

Figure 5.4: Mean u_{rms} profiles behind the cylinder with zero offset.

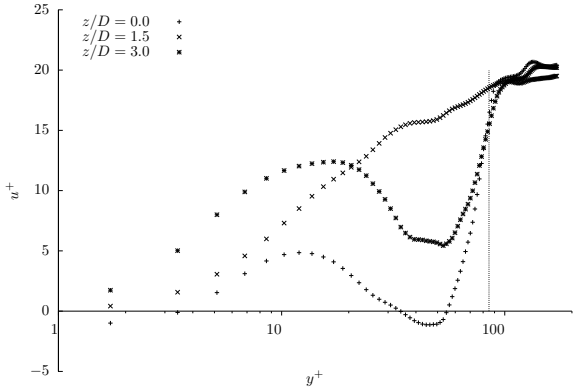

Figure 5.5: Mean velocity profiles at $X/D = 15$ and at different offsets.

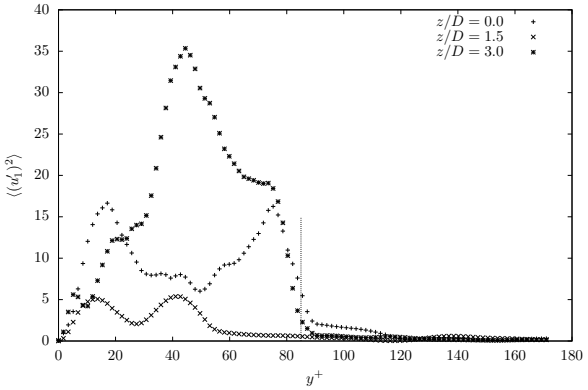

Figure 5.6: Mean u_{rms} profiles at $X/D = 15$ and at different offsets.

circulation zone forming the splat. The location of the splat is $X/D = 11$ units away from the inlet, at a height of approximately $y^+ \approx 50$. This recirculation length can be contrasted with experimental data found in Martinuzzi and Tropea [33], or earlier data-fitted equations given in Hosker [18]. The latter work proposes the following equation:

$$\frac{L}{\delta} = \frac{A(D/\delta)}{1 + B(D/\delta)}$$
$$A = -2 + 3.7(D/\delta)^{-1/3}$$
$$B = -0.15 + 0.305(D/\delta)^{-1/3}$$

Where L is the distance measured from the leeward face of the cylinder to the end of the circulation zone. The equation predicts a recirculation zone of length $L/D \approx 5$, which locates the splat at $X/D = 12.5$. A similar location is obtained using the data-fitting in Martinuzzi and Tropea [33].

On the air side, the streamwise velocity profiles shown in fig. 5.3 serve to study the extent of the anomaly caused by the cylinder in the crossflow with the incident turbulent boundary layer . This fully-submerged cylinder, for which its tip is indicated by the vertical dashed line in the aforementioned figures, causes anomalies in the velocity and RMS profiles on the incident flow that extends up to the outlet of the domain; previous studies [35, 45] reported that, for high-Re, the mean streamwise velocity deficit decays at $X/D \approx 8$, although these experiments were for much higher Re thus having the wall-mounted obstacle fully immersed in the inner region. However, similarities in the velocity fluctuations shown in figure 5.4 are present, such as the second u_{rms} peak located below the cylinder tip (around 7/8 of the cylinder height), and that the interaction of the vortices shed from the cylinder with the structures of the incoming flow suppresses the prominence of the former, as it can be seen in figure 5.2 where no dominant shedding frequency is detected after $X/D \approx 11$ as shown in Figure 5.8. The suppresion of the shedding is due to the splat-downwash generated by the high-velocity flow passing at the tip of the cylinder, confining the recirculation zone behind it to a length of $X/D = 3.5$ measured from the axis of the cylinder, depicted as region B in fig. 5.2 and detectable as the region of highest u_{rms} in figure 5.4. Finally, the interaction between wakes generated by the spanwise arrangement of finite-height cylinders are detected downstream of the splat, as depicted in Figure 5.6 where it manifests as a large peak of u_{rms} at offset $Z/D = 1.5$. Such interaction usually is detected [45] farther downstream ($X/D = 11.5$) but on a similar offset from the midplane ($Z/D = 1.3$).

It is typically accepted that for flows around finite cylinders generated by incident near-uniform flows or zero-pressure boundary layers, height-to-diameter ratios larger than 2.5, three vortex structures are generated: Kàrmàn streets, tip vortex, and horseshoe vortex; focus will be given to the horseshoe vortex. In fig. 5.9 , mean vorticity magnitude contours

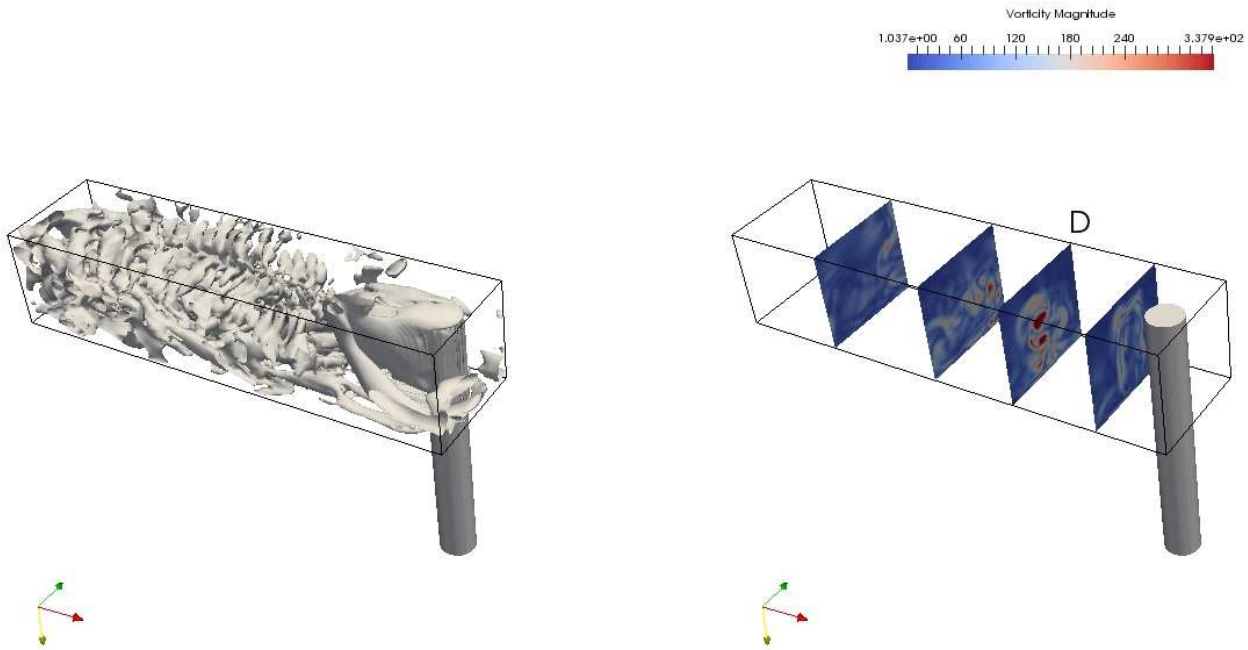

Figure 5.7: Left: iso-contours of λ_2 on the air side, right: vorticity contours at different planes

close to the interface show no distinguishable shedding behavior in the region upstream of the splat, and figure 5.7 on the left show the formation of the horseshoe vortex in front of the cylinder while on the right the mean vorticity contours show (plate D) the vortex pairing of the horseshoe's legs. Note that the legs of the horseshoe vortex lift well into the mid-channel depth. On the other hand, fig. 5.10 and 5.11 show that where the interaction with the incident structures is not as strong as it is the case close to the interface in the water side, the horseshoe vortex and vortex shedding are clearly present. In fact, although the flow velocities are much higher close to the interface that to the wall in the marine case the vortex system near the interface is more free to develop laterally compared to the obstacle-interface junction in the air side. Also, it is interesting to note that on the obstacle-wall junction no shedding can be seen in fig. 5.11, whereas on the air side is seen (see fig. 5.9) although it was shown earlier that the interface on the air side behaves much like a wall.

Flow in the shallow water channel

On the water side of the system, where the cylinder is fully immersed, more complicated flow features arise. In Figure 5.12 the mean velocity magnitude field reveals the formation of windward circulation regions on the lower junction between the circular cylinder and the wall. Such circulations rotate clockwise, by virtue of conservation of angular momentum, and go around the base of the cylinder forming a horseshoe vortex which lifts in the leeward

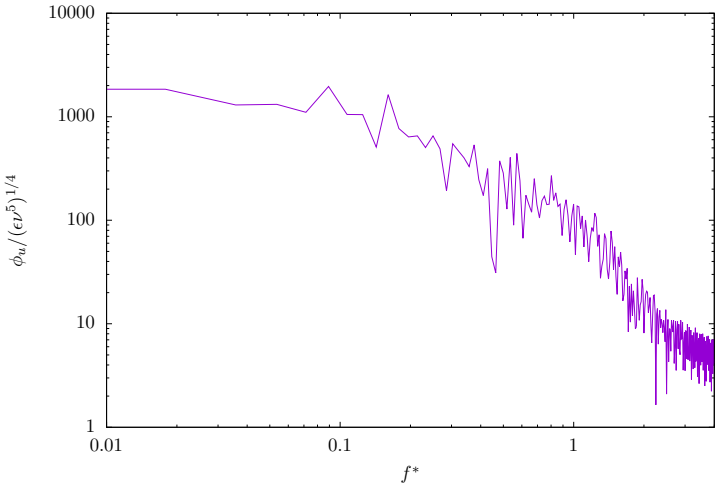

Figure 5.8: Time frequency spectra of $\overline{u_1 u_1}$ at location $X/D = 11$ in the midplane of the channel.

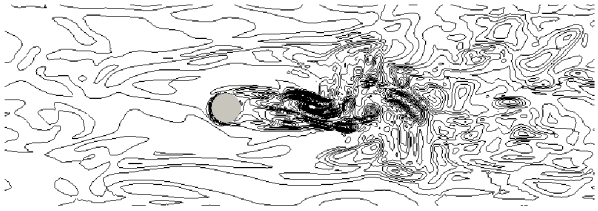

Figure 5.9: Vorticity contours in air side at cylinder base close to wall $y^+ = 17.1$.

Figure 5.10: Vorticity contours in water side at cylinder base off the interface $y^+ = 17.1$.

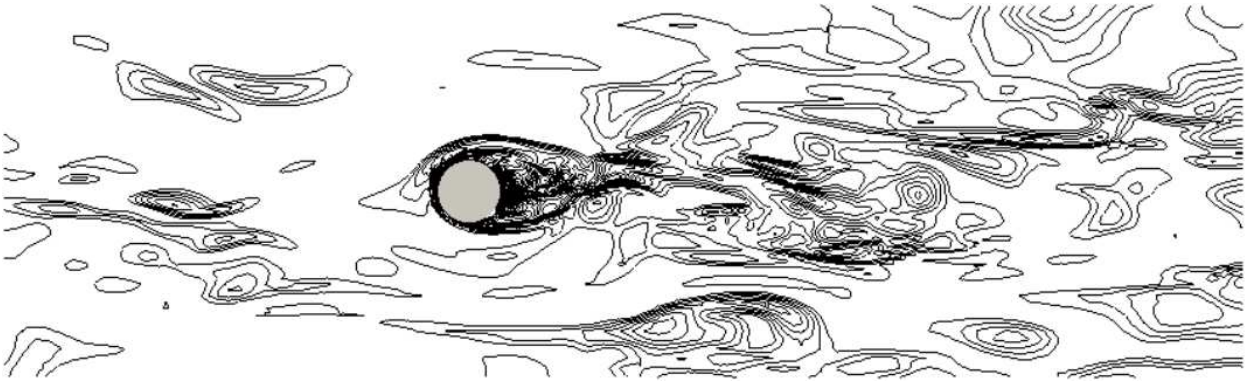

Figure 5.11: Vorticity contours in water side at cylinder base close to wall $y^+ = 17.1$.

side of the cylinder producing vertical vorticity as seen in Figure 5.13.

The sudden increase in pressure due to the blockage caused by the cylinder distributes the incoming energy towards the spanwise direction causing an increase in shear that ultimately enhances the production of Reynolds stresses in the windward section of the cylinder, as seen in Figure 5.14. Additionally the uplifting of the horseshoe vortex brings low-speed fluid flow to the core region of the channel, evidenced by the regions of low $\langle u'v \rangle$ near the base. Farther downstream, the interaction between the structures shed from the cylinder brings about a further increase in shear that ultimately translates in the production of Reynolds stresses. Finally, Figure 5.15 shows that for the windward face of the cylinder, the increase of turbulence production due to the increase in Reynolds stresses translates into higher values of k^2. A comparison between Figures 5.15 and 5.14 reveal an overlap between k^2 and $\langle u'v' \rangle$ at the wake of the cylinder which is again product of the higher shear produced by the interaction of shedding vortices.

Flow in the shallow channel without the cylinder on the air side

From previous chapters it was shown that waterside motions have negligible feedback with the interface boundary layer formed on the air side, partly due to the fact that coherent structures have much smaller "attack" angles in the air compared to its water counterparts. Given that here the scales of the structures formed in the air side are are not confined to the inner scales of the inbound boundary layer, but on the size of the cylinder, it it interesting to analyze whether these large-scales structures in the air have greater influence on the flow underneath. Figure 5.16 shows that indeed it is not the case, when comparing it with Figure 5.15. In general, the far greater inertia of water impedes that both small and large scale events in the air have influence on the dynamics of the flow on the shallow channel.

5.4 Flow around a square cylinder: configuration and results

Here, the geometry of the domain and the location of the square cylinder is depicted on Figure 5.17. Notice that some differences exist with the previous case: (1) the cylinder has a side (diameter in the previous case) equal to the height of the channel, and (2) the cylinder's height in the air domain is 1/10th of the total height of the channel. For convenience, the spatial scaling of the domains is performed taking the thickness of the inflow boundary layer, δ, as characteristic length. Each of the domains is discretized into $256 \times 96 \times 96$ hexahedra, and refinement is performed in the direction normal to the walls, the immersed boundaries,

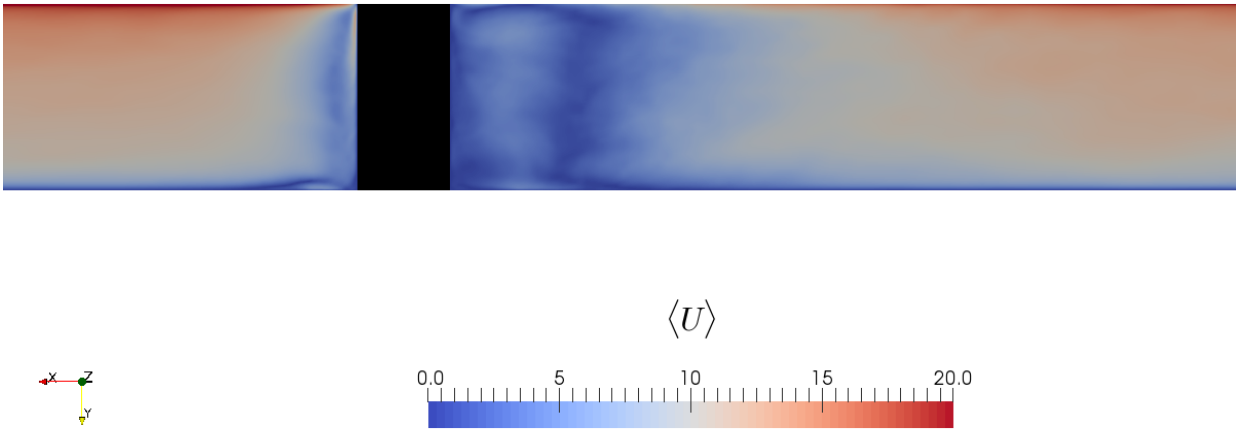

Figure 5.12: Magnitude of mean velocities at midplane of the shallow channel.

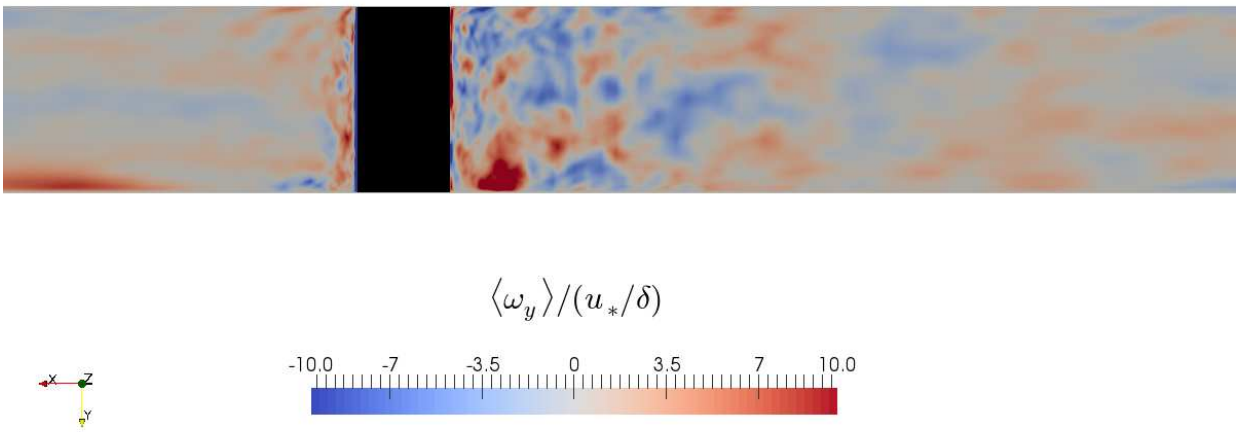

Figure 5.13: Mean vertical vorticity component at midplane of the shallow channel.

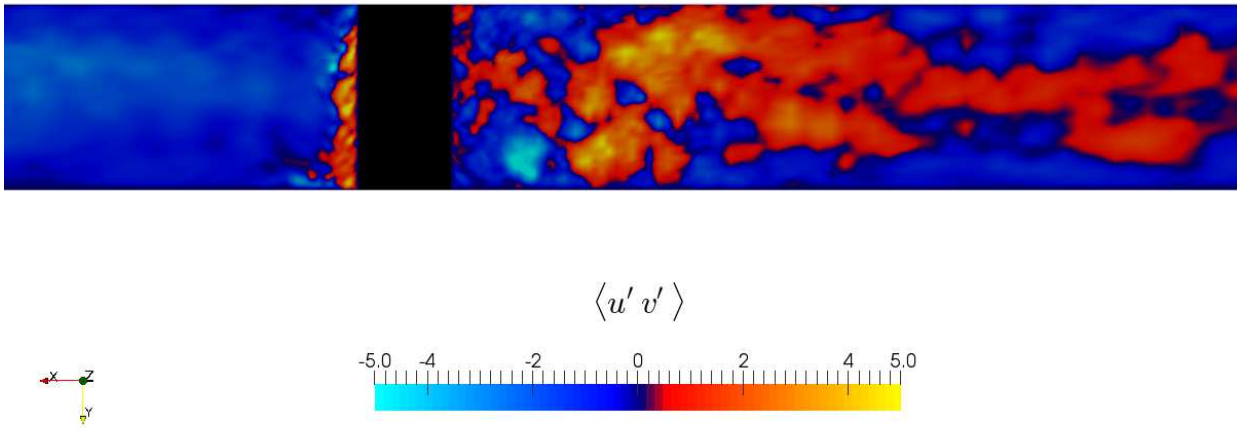

Figure 5.14: Mean Reynolds stress at midplane of the shallow channel.

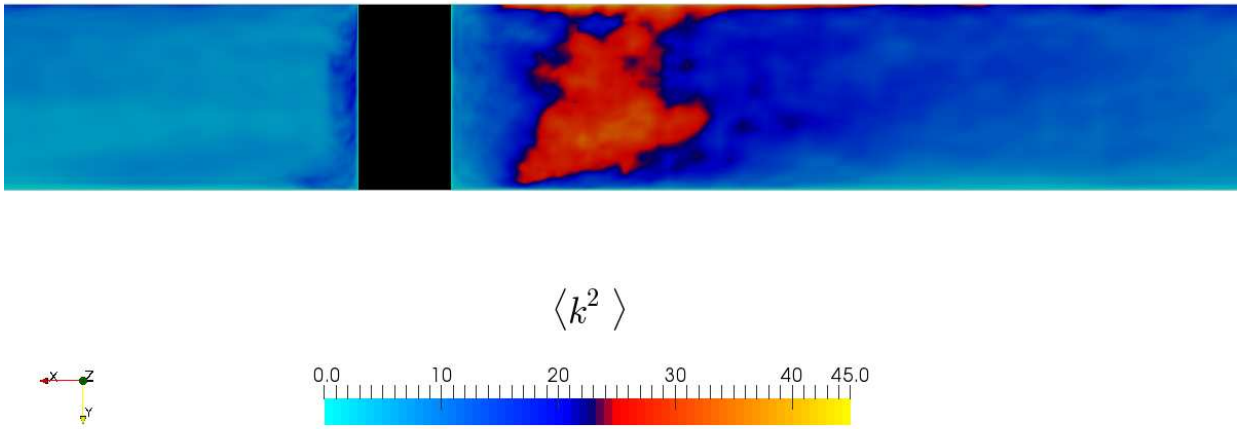

Figure 5.15: Mean turbulent kinetic energy $\langle k^2 = 0.5(u_i')^2 \rangle$ at midplane of the shallow channel.

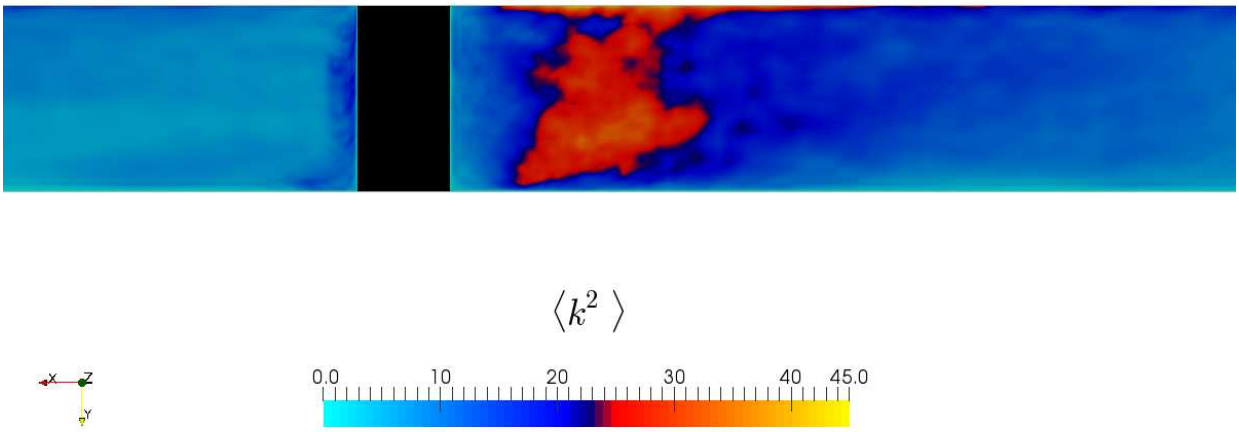

Figure 5.16: Mean turbulent kinetic energy $\langle k^2 = 0.5(u_i')^2 \rangle$ at midplane of the shallow channel, where the circular cylinder is only present.

and the interface as required to obtain a *resolved* field.

Flow in the air domain

A series of time-averaged vertical profiles of the different resolved quantities are computed at different midplane locations at the wake of the cylinder. As it was previously stated this part of the chapter will concentrate on the structure of turbulence by determining the deficits that the obstacle causes on the different flow quantities. In Figure 5.18 some results are shown, concerning the structure of the perturbed boundary layer. The mean streamwise velocity profiles show that the extent of the recirculation region arrives up to $X/D \approx 1.92$ (not shown in the plates) and that the boundary layer returns to a quasi-unperturbed state after $X/D \approx 5.6$. The vertical extent of the downwash jet from the separated layer formed at the upstream tip of the cylinder is seen from the vertical velocity profiles just presented. From the latter profiles it can be seen that the the downward gush of flow slightly penetrates below the cylinder's height into the recirculation region, in the first two probes. The downwash jet is distributed horizontally once it hit the lower impregnable boundary, or the interface in the current case, and has been completely dissipated after $X/D = 6.00$.

As it has been previously shown, the shear region product of the downwash jet and the opposing recirculation zone forms slightly below the cylinder's tip. Nevertheless, note that the $\langle u'u' \rangle$ component of the Reynolds stresses find its maximum *above* the cylinder's tip

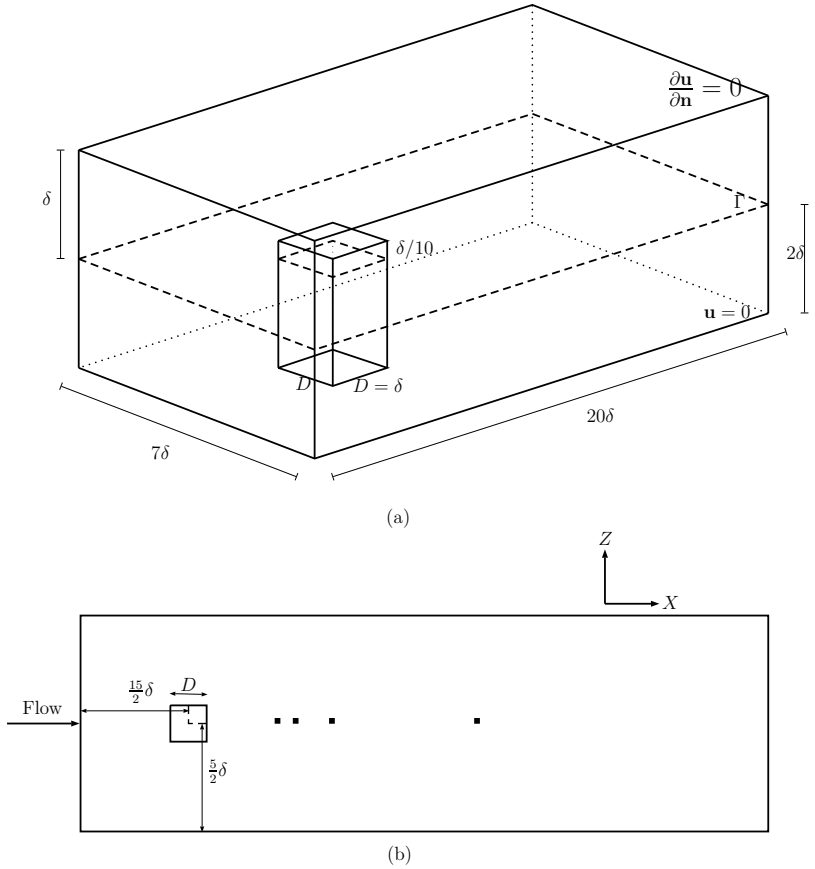

Figure 5.17: Configuration sketch for a square cylinder immersed in an air-water system. The square dots denote probes located at $X/D = 1.25, 1.50, 2.00, 6.00$ from the leeward face of the cylinder.

suggesting that such disturbance is convected down from the cylinder's top surface. Note that the loci of the said peaks are located at $y^+ - 0.1y^+ \approx 13.5$, whcih is slightly above the the height reported for canonical wall-bounded channel flows. When the $X/D = 6.00$ probe is reached, the peak has slightly descended below the $0.1y^+$ threshold. A similar analysis can be made for the $\langle u'v' \rangle$ Reynolds stresses, except for probe $X/D = 1.25$ where a second peak appears within the recirculation region. Such peak has its origins on the increase in the production of turbulence, due to dissipation, consequence of the interaction across the shear layer formed between the recirculation vortices and the gushing jet from coming from the cylinder.

In Figure 5.19 a series of time-averaged midplane vertical profiles, taken at the cylinder's roof, for different flow quantities are shown. From the streamwise velocity profiles it can be seen that, in average, the flow remains attached to the cylinder's roof thus indicating the intermittent character of the tip vortex. The vertical velocity profiles account for the inception of surface jet that will impinge the recirculation region downstream of the cylinder,

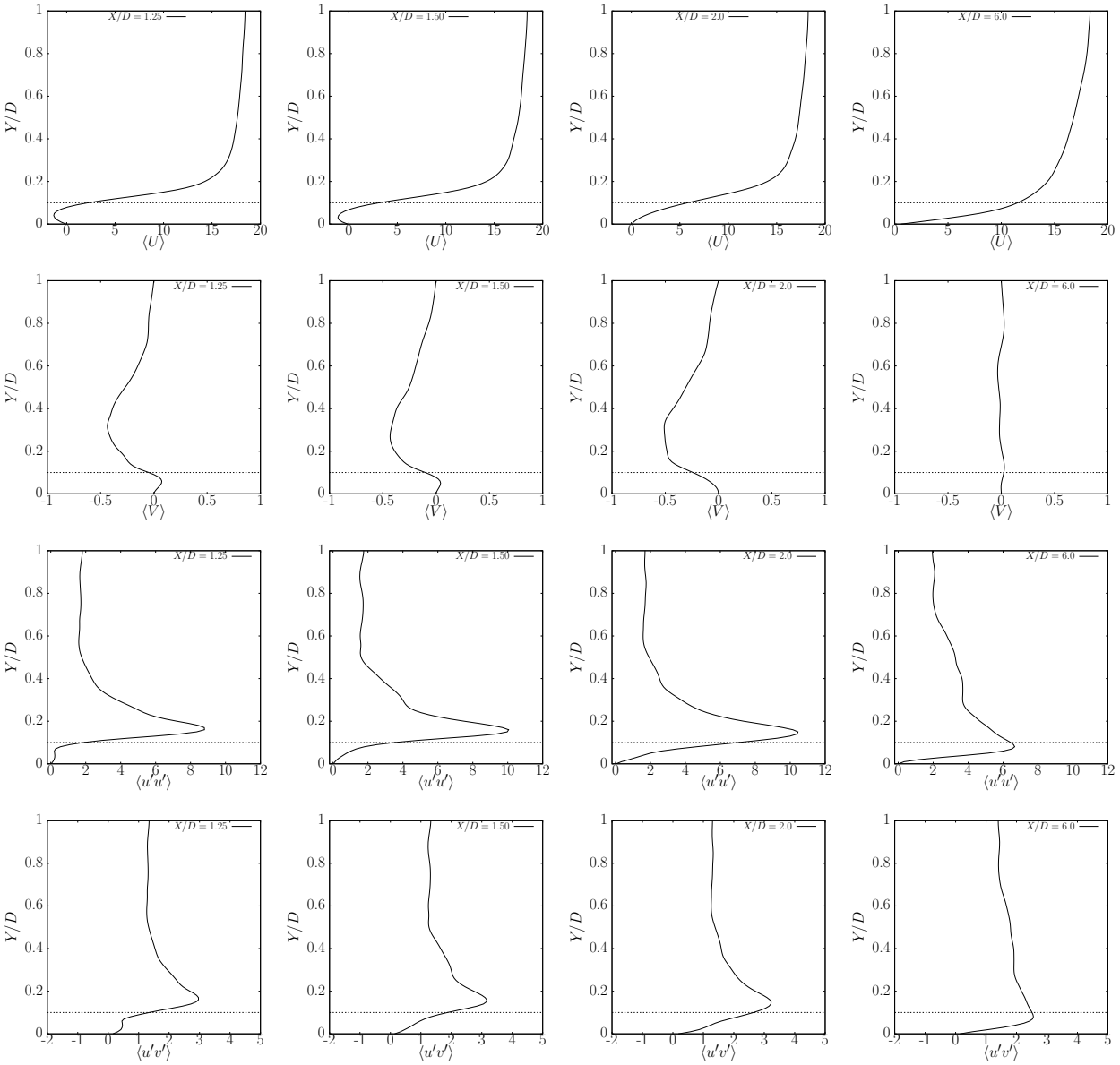

Figure 5.18: Mean vertical profiles for different flow quantities taken at the midplane of the channel, and at different locations from the leeward face of the cylinder. The dashed line depicts the tip of the obstacle.

as previously mentioned. For the case of the $\langle u'v' \rangle$ profiles, the overall behavior along the cylinder's roof remains roughly similar. On the other hand, the intermittent generation of spanwise vorticity at the upstream edge of the cylinder, where the momentum equations become singular, produces counter-gradient motions that induces negative $\langle u'v' \rangle$ Reynolds stresses so for the production of turbulence to remain positive. Additionally, the persistence of the tip vortex is not detected anymore farther downstream from the edge of the block ($X/D = 0.0$) in the $\langle u'v' \rangle$ profiles.

Flow features

The submerged obstacle in the air side boundary layer produces flow patterns that are similar to those present in canonical flows around mounted cubes. In Figure 5.20, the legs of a horseshoe vortex are shown as the strong positive/negative ω_y signals in the contour panel. The effect of such vortex structure is to pump flow into the recirculation region, as evidenced by the velocity vectors in the same Figure. Earlier it was shown that the recirculation region was confined in the vertical by a high-speed downwash jet, as a consequence of this the flow pumped into the wake region has to be convected downstream by the same vortex cores by virtue of mass conservation. The latter constraint will invariably force the horseshoe legs to come closer together as the recirculation region becomes weaker.

Figure 5.21 shows three-dimensional isosurfaces of pressure and of vortex core regions. The white surfaces represent contours of the negative second eigenvalue calculated for the pressure hessian tensor [36], where it can be seen the horseshoe vortex forming at the base of the cylinder. Note that the roll formed at the front of the cylinder encircles regions of *negative pressure*, although a great region of the flow upstream of the cylinder has positive pressure. Furthermore, the separated flow above the cylinder is embedded by a negative pressure region following the fact that separated region occur where pressure gradients follow the direction of the flow.

Oil-film visualization of the flow patterns around a wall mounted cube are shown in Figure 5.22, which were taken from the seminal work of Martinuzzi and Tropea [33]. There it was shown that two regions of separation occur in the flow incident to the square cylinder: (1) an outer separation line, denoted by A in the Figure, due to the intermittent decay and regeneration process undergone by the saddle point (the black region on the left hand side), and (2) a roughly time-average separation line, denoted by B, where the axis of the horseshoe vortex lie. A comparison of this image with Figure 5.23 reveal that no such patterns are present in a time-average sense. Note that it has been shown the (instantaneous) existence of a horseshoe vortex generated by the immersed obstacle, therefore the relatively slight submergence of the obstacle in the air side only produces short-lived structures of this kind.

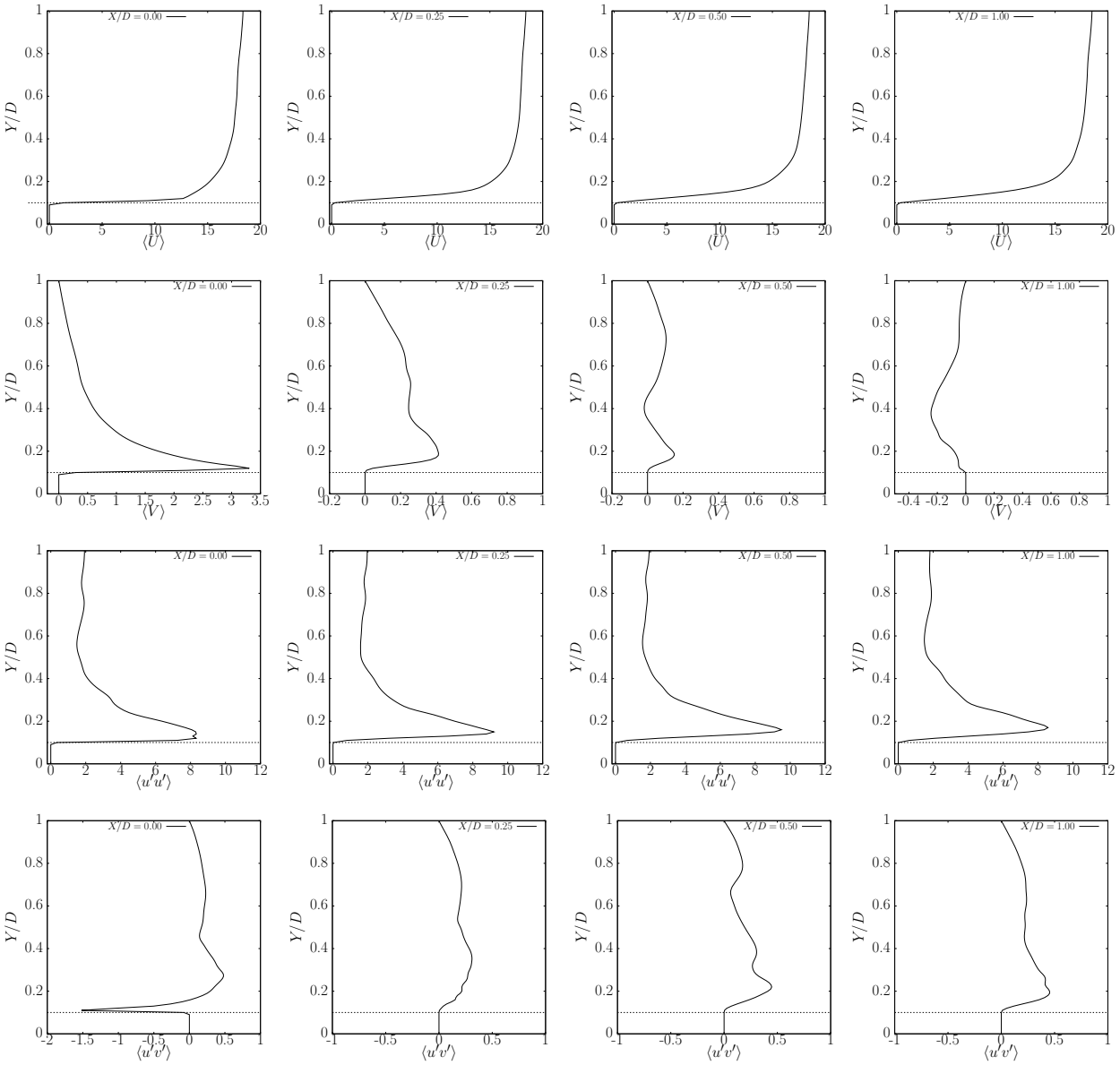

Figure 5.19: Mean vertical profiles for different flow quantities taken at the top of the square cylinder, and at different centreline locations from the windward face of the cylinder. The dashed line depicts the tip of the obstacle.

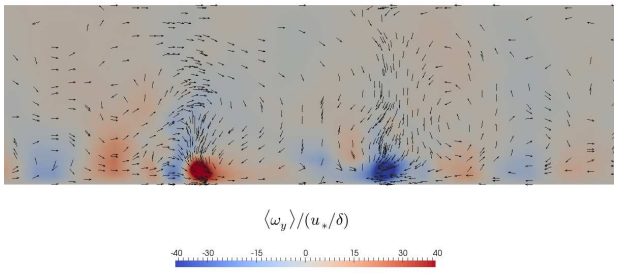

Figure 5.20: Instantaneous streamwise-normal plane of the turbulent vertical vorticity and parallel velocity verctors taken at a distance $X/D = 1.75$ from the leeward face of the cylinder.

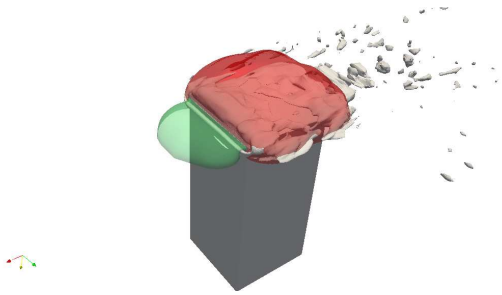

Figure 5.21: Isosurface of vortex structures around the cube educed using λ_2, and of pressure distribution. The green colors represents regions of positive pressure, whereas the red regions represent regions of negative pressure.

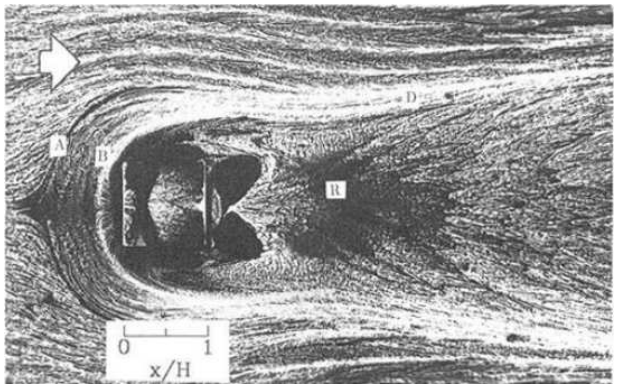

Figure 5.22: Oil film visualization of wall-surface streamlines around an immersed square obstacle, taken from [33].

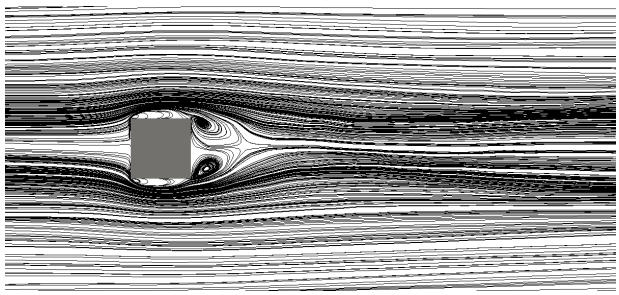

Figure 5.23: Time-Average Surface streamlines at the interface in the air subdomain.

On the wake region of the cylinder, the patterns shown in experiments are qualitatively similar to the ones obtained in the current experiments, except for the horizontal contraction (line D in the oil film visualization) of the recirculation zone which, in average, occurs earlier in the numerical simulations.

Detection of structure modulation via Proper Orthogonal decomposition (POD)

Theory

The quantification and visualization of energy-carrying structures following the eduction techniques used previously prove insufficient in determining the modulation undergone by the

quasi-streamwise structures due to the 'd'-type roughness element immersed in the channel. In particular, the λ_2 criterion does not guarantee that the regions of the flow where it is negative the velocity fluctuations are correlated. On the other hand, two-point velocity correlations do not provide any information related to the energy carried by the correlated regions.

The deficiencies of such methods can be overcome, at least partially, by applying a Proper Orthogonal Decomposition on the turbulent velocities. Basically, the method projects the velocity field into an n-dimensional ellipsoid where each of its n principal axes represent an orthonormal basis for the velocity components. Also, the magnitude of each of the axes represents the variance of the field or, simply put, the energy over each of the comprising axes. More accurately, The method consist in performing an orthogonal decomposition of each of the velocity components as follows

$$u(\mathbf{x}, t) = \sum_{n=1}^{\infty} a_n(t)\varphi_n(\mathbf{x}) \tag{5.1}$$

Where the linear span $\{\varphi_i\}_{i=1}^{\infty}$ is a set of basis functions that satisfy the following orthogonality condition

$$\int \varphi_i(\mathbf{x})\varphi_j(\mathbf{x})\, d\mathbf{x} = \delta_i^j \tag{5.2}$$

Where δ_i^j is known as the Kronecker delta operator. Notice that the coefficients a_n can be found by multiplying Equation 5.1 by φ_m and integrating, thus obtaining

$$a_m = \frac{1}{|\Omega|} \int u(\mathbf{x})\varphi_m(\mathbf{x})\, d\mathbf{x} \tag{5.3}$$

Where $|\Omega|$ is some measure for the region of integration. The basis functions can be chosen to be Fourier transforms, otherwise Chebyshev expansions, depending on the directions of periodicity and the dimensions of the input data matrix. Anyway, given that the present case has a *discrete* set of basis functions for the set of measurements (velocities) or probes in the flow, a *Singular Value Decomposition* (SVD) technique on the input measurements is sought. The method proposes to calculate the SVD of an input matrix A of dimensions $N \times m$, where N is the number of times we take measurements on the m probes in the flow. Such decomposition is written

$$A = U\Sigma V^T \tag{5.4}$$

Where Σ is a $N \times m$ diagonal matrix, U is a $N \times N$ orthogonal matrix, and V is an orthogonal $m \times m$ matrix. Note that the n positive non-zero diagonal elements of Σ, σ_i,

are unique and represent an orthonormal basis for an associated n-dimensional ellipsoid by virtue of the *Principal Axis Theorem*. It can be shown that the set $\{\sigma_r\}_{r=1}^{n}$ has dimensions $n = \min(N, m)$. Notice that the correspondence with Equation 5.1 is clear if one writes the SVD in the following manner

$$A = U\Sigma V^T = QV^T = \sum_{k=1}^{m} q_k \, v_k^T \tag{5.5}$$

Where q_k is a column matrix representing the discrete version of $a_k(t)$, and v_k^T a row matrix representing the basis $\varphi_m(\mathbf{x})$.

Computations

A POD-decomposed velocity field for the flow in the air domain is shown in Figure 5.24, for the second eigenmode corresponding to the spanwise velocities. By virtue of the SVD method the eigenmodes are given in a highest-to-lowest energy order, that is, $\sigma_1 < \sigma_2 < \sigma 3$, meaning that the POD for the spanwise velocities just presented correspond to the second-highest energetic mode. Note that for pressure-gradient driven boundary layers the most energetic mode, the one with the largest contribution to the Reynolds stress tensor, is the mode that shares the same basis as the pressure gradient, which for this case is the streamwise direction. Furthermore, in wall-bounded flows the second mode with highest energy corresponds to the vertical direction and the third mode corresponnd to the spanwise direction, as it can be seen from the velocity RMS profiles of, say, the channel flow cases shown in the Appendix. In the case of immersed obstacles in the boundary layer, the spanwise direction presents higher variability compared to the vertical direction due to the low vertical-to-spanwise aspect ratio of the embedded element.

Modulation of the incoming energetic σ_2 motions due to the presence of the obstacle is readily seen in Figure 5.24a. The incoming coherent motions, detected as the positive regions in the Figure, have a markedly higher length compared to the motions after passing the obstacles. Also, the anomalies on the spanwise fraction of the kinetic energy due presence of the obstacle, seem to extend up to 7 heights from the leeward face of the object. Moreover, spanwise interference between wakes produced by an array of obstacles (in this case, due to periodicity in the spanwise direction) is not seen in Figure 5.24b, where the plane is located at the cylinder's mid-height.

Finally, it has been mentioned previously that due to the high-aspect ratio of the blockage vortex shedding from the top and the sides of the cylinder are hindered by the highly-energetic upstream structures. Nevertheless, in previous sections it has been shown the existence of the so-called horseshoe vortex result of the backflow generated at the wind-

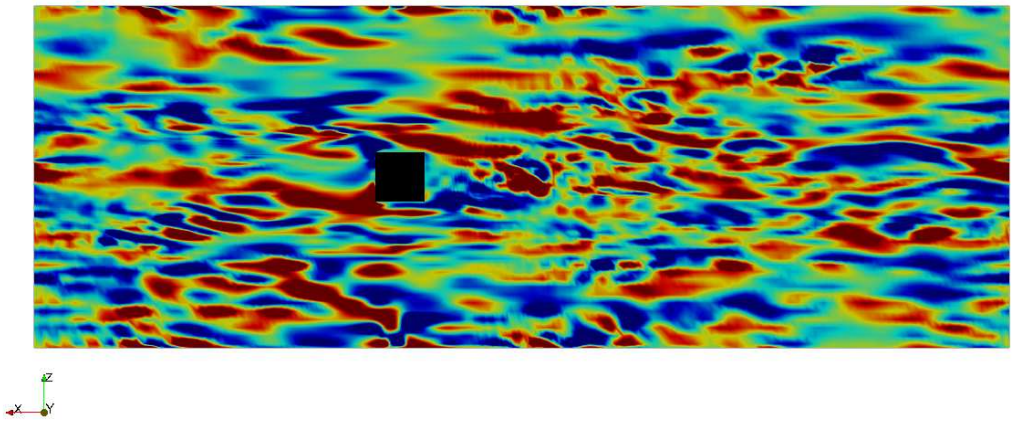

(a)

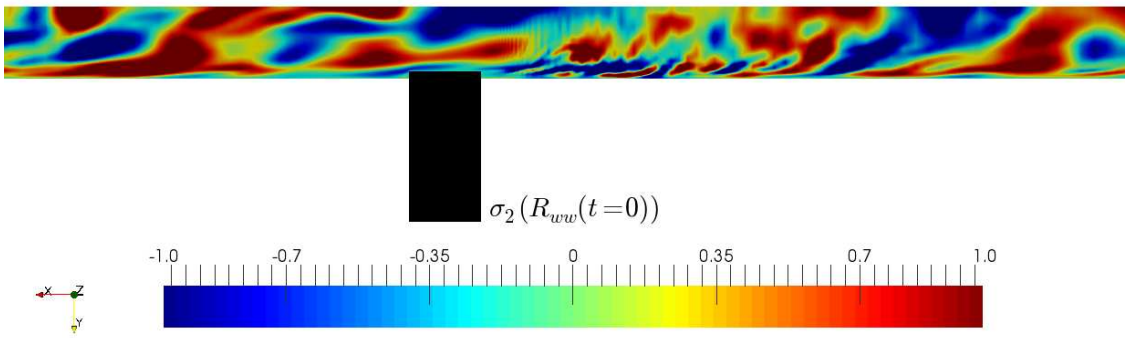

(b)

Figure 5.24: Countours of positive/negative modal spanwise velocity contained in the second POD mode for (a) a horizontal plane taken at height $y^+ = 8.55$ off the interface, and (b) for mid-channel plane.

ward corner between the solid and the interface. As shown in Figure 5.25, the horseshoe vortex carries mostly energy coming vertical motions produced by the increase in pressure fluctuations in the near obstacle region.

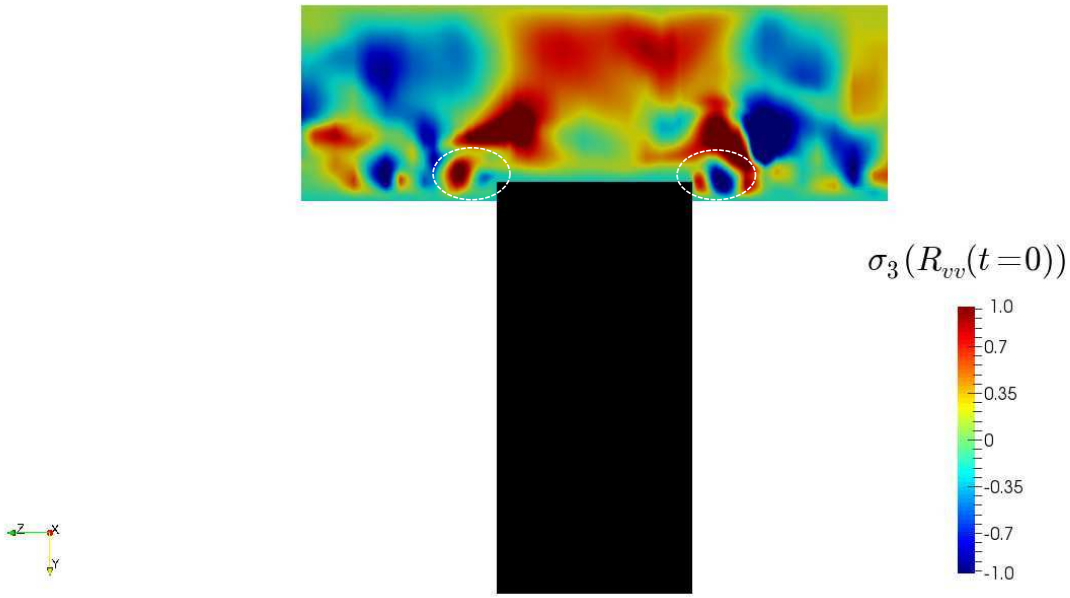

Figure 5.25: Countours of positive/negative modal vertical velocity for the third POD mode in an x-normal plane located at the axis of the cylinder. The dashes ellipses encircle the legs of a horseshoe vortex.

Chapter 6

Discussion

A coupling strategy was implemented on LESCOAST in order to superposed, immiscible flows with a infinitely thin interface. Such a coupling strategy, called non-iterative sub-structuring method, has been implemented with relative success on DNS codes to model interfacial flows [29]. An initial study of the coupling method over LESCOAST, which is a second order accurate finite difference method for the solution of the Navier-Stokes Equations in 3D, reveals a general reduction of order of the solution obtained. Furthermore, given the inexact treatment of the interface boundary, a lower CFL condition than the one imposed by the explicit treatment of viscosity ([52]) has to be used in order to achieve convergence. No explicit technique is available to determine which is the CFL condition suited for this kind of coupling strategy.

On the other hand, the implementation of the method itself is relatively simple and it guarantees to be the fastest among the sub-structuring methods since no internal iterations are needed for the coupling. Also, the reduction of the error order, and possible reduction of precision in the solution, can be overcome by using a low CFL condition which, in some cases like DNS, is necessary to use.

6.1 Couette-Couette flow

On Chapter 3, LES of a counter-current sheared interfacial flow at $Re_\tau = 171$ has been used to investigate high-order statistics, vorticity, quadrant analysis, interfacial shear stress distribution, and near-interface streamwise and wall-normal velocity events on both comprising fluids, chosen to be air and water. Non-zero vertical vorticity fluctuations on the water side ensure increased enstrophy that is reflected on the higher degree of mixing present on this boundary layer, which renders it thinner. The classic quadrant analysis show a behavior similar to that of Lombardi et al. [29], although a detailed analysis of the skewness and

flatness factors show higher intensity of negative velocity events on the near interface region for the water side. Despite of the rather high grid refinement used for this study, the SGS fluxes generated via the Dynamic Smagorinsky model offer slightly more intermittent results when compared to a no-model approach.

By extending the original approach taken by Lombardi et al. [29] for studying the degree of Reynolds stress coupling, a 'strong' quadrant analysis of the (u, v) velocities reveal existence of strong rare Q4 events on the air side while Q2-Q3 strong rare events are characteristic of water. This analysis show what intuitively was mentioned as higher mixing due to the thinning of the boundary layer on water, as these rare strong counter-gradient (Q3) events ensure increased mixing. At the same time, joint PDF of 'strong' streamwise-to-vertical velocities show a bi-modal behavior of streamwise velocities that are weakly correlated to its vertical counterparts on either side of the interface. Furthermore, rare splats over the inteface on the water side are seen as highly negative negative velocity events, and correlate with rare and intense low-speed ejections. Despite such marked differences in the distribution of horizontal fluctuating backflow velocities across the interface, the distribution of strong quadrant events on the opposite sides of the interface are qualitatively similar to each other, indicating the coupled origin of the distribution of the interface shear stress.

Eduction of vortical structures and contouring of τ' on the channels reveal that the spatial structure of the instantaneous shear stresses is streaky, and that alternating instantaneous patches of positive and negative τ' sit around the educed vortices. This goes in contrast with the canonical behavior of shear in wall-bounded channels where is shown that negative patches of shear stress are seldom detected being its spatial structure circular and being generated by oblique vortices [27]. These streaks of negative shear are consequence of the very frequent backflow velocities occuring on the water side, indicating that interfacial shear is controlled by the water side. Also, an analysis on the distribution of the vorticity angles θ_{xz} and θ_{yx} reveal the presence of streamwise and vertically inclined vortices on the water side, where the latter are more frequent. The existence of such inclined structures along with the streamwise ones explain the bimodal PDF distribution of 'strong' streamwise velocities taken at height $y^+ = 1.26$.

Coupled quadrant events are the mechanism responsible for the quite frequent backflow events seen in the distribution of instantaneous shear stresses. As expected, the high-probability coupled mechanisms involve always either strong ejections or sweeps in the near-interface region. Coupled events where sweeps happen on the water side account for the positive generation of instantaneous shear stress, and ejections on the air side account for the converse scenario. Specifically, distributions of type 2-2, 2-1, and 1-2 are negatively skewed and the mode is negative as well.

6.2 Poiseuille-Couette flow

Turbulence on coupled Couette-Poiseuille boundary layers in air-water systems is investigated using LES, and presented in Chapter 4. More precisely, the interaction between coupled Poiseuille-Couette air-water flows is studied under low Reynolds number conditions. Few numerical experiments of this type have been reported, despite its importance for the study of atmospheric and oceanic flows. In general, most of the previous studies have been focused on the study of interface scalar transfer while very few are dedicated exclusively to long-time statistics for turbulent flow quantities. Furthermore, such studies have been made for different flow configurations. However, the present work focuses on flow dynamics on the shallow water channel, or Couette, portion of the system.

The time-averaged turbulent field

The turbulent statistics for the air section of the system are quantitatively similar to turbulent Poiseuille flows. Such behaviour on the air boundary layer is expected since the higher inertia of the water limits greatly the near-interface motion, leading to a near zero convection of turbulence in the viscous region. The action of the interface on the air side provides little to the near-interface dissipation of turbulent kinetic energy, due to the sharp scaling, $\mathcal{R} \approx 29.9$, of horizontal Reynolds stresses. Furthermore, although the presence of the interface allow for non-zero production of vertical vorticity at the interface, its effects on the inclination of the near-interface vortex cores and attached structures is negligible. Also, profiles of Reynolds stress balance and Quadrant analyses show uncanny similarities with pressure-driven wall boundary layers.

In the shallow channel, first- and second-order statistical moments of velocity show that the boundary layer formed on the interface side of the channel is thinner. In principle, the thinning of the interface-bound boundary layer allow for a greater turbulent horizontal mixing as a result of the less restrictive action of the interface on the water side motions. Furthermore, the greater intermittency of velocities common in Couette flows is also present here and extends up to the opposite side, the wall side, of the channel. The balance of Reynolds stresses further confirms the fact that higher intermittency of motions are present on the interface-bound boundary layer, and marks a clear difference with classical Couette flows by moving the maximum from the centreline of the channel to the upper-half (the interface boundary layer) part of the channel. Additionally, the TKE profiles show that the interface provides for an increased dissipation that is met by the aformentioned increase in intermittency. Such increase in intermittency is also explained by the increase of turbulent transport in the water column. Notice that the pressure-velocity term in the TKE is quali-

tatively similar to wall boundary layers, where energy is drained from the streamwise to the vertical and spanwise directions. Finally, the quadrant analysis of all velocity events and of only 'strong' events show a decrease on the occurence of near-interface ejections and an increase of near-interface sweeps, compared to the wall side on the shallow channel. The latter results are also reported for classic Couette flows [5, 26], and attributed to the interaction of the outer region of the flow with the boundary layers. Note that in the aforementioned works the outer layer interaction was attributed there because of the maximum locus of $\langle u'v' \rangle$, although for the present study such location can be attributed to the buffer region of the interface-bound boundary layer.

The two-point correlation of velocities shown in section 4.2.4 indicate that the current turbulent flow realization is found on a 'periodic' state, for the case of the shallow water channel. In such chase, the influence of the so-called super-structures on the outer scales of the flow are unlikely to be present. Notice that the horizontal domain dimensions used here, $4\pi \times 2\pi \times (1,\ 2)$, are at least double than the ones used in previous studies on coupled flows.

Inclined vortex cores and VISA

The non-negligible production of vertical vorticity provided by the interface in the shallow channel opaques the presence of quasi-streamwise vortices, while it enhances a bi-modal state of inclined vortices near the interface. As shown in Figure 4.15, inclined vortices exist on a range $\pm 45°$ from the normal to the interface. The interpenetration of such structures onto the viscous sub-layer from the outer region is explained by the sudden thinning of the inner region of the boundary layer, due to the increase horizontal mixing present in the interface-bound boundary layer.

Such increase in the outer-to-inner region interaction within the interface boundary layer is supported by the conditionally-averaged vertical vorticity field shown in Figure 4.17a. There, highly intermittent ω_y events populate the viscous region of the interface-bound boundary layer. On the other hand, wall-bound events shown in Figure 4.17b are not as widely present as the interaction with the outer layer for such low Reynolds number is expected to be weak.

Backflow events and interface shear stress

Given the relaxed boundary condition that represents the interface, higher backflow events are present in the near-interface region. The separation zones result of such events result in less drag on the overall system, nevertheless extreme interface shear events are produced on either side of the flow.

Regions of highly-intermittent positive vertical vorticity cohabit with zones of backflow and separation, as shown in Figure 4.17. Such 'islands' are more common near the interface, where a higher occurrence of separation zones is possible.

6.3 Flow around immersed cylinders in air-water systems

In Chapter 5, a study of the flow features present in a cylinder fully submerged in a water shallow channel and only partially in the air side was made. Two cylinder shapes were used and different height-to-width ratios were used for the two simulations herein conducted.

Spanwise array of circular cylinders

On the first case where a spanwise array of circular cylinders with a height-to-width ratio of 2.5 was used on the air side, attention was given to the shedding behaviour for the different vortex structures with origin on the wake of the cylinder, in air and water. Previous research [11] has shown that the chosen height-to-width ratio produces shedding vortices in the wake of a circular cylinder immersed in a fluid with an uniform incident flow. The current analysis shows that for cylinders fully immersed in the air boundary layer, transient shedding is hindered by the lateral entrainment of incident elongated coherent structures as well as for the impingement of high-speed flow coming from the tip of the cylinder. Previous experiments conducted over wall mounted obstacles in high-Reynolds number boundary layers [45] have shown that wake interference between obstacle spanwise arrays, of characteristic length L, may extend downstream well beyond $10L$ downstream the blockage independent from the height-to-width ratio, in the current analysis it was found that the anomaly consequence of the blockage extends well beyond the outlet of the model located at a distance $12.5L$ from the leeward face of the circular cylinder. Furthermore, wake interference between neighboring cylinders occur at a location $7.5L$ from the leeward face of the cylinder where the wake extends $\pm 1.5L$ away from the midplane in the spanwise direction. Previous experiments [35] have reported interference locations closer to the leeward face and to the midplane, but for square cylinders immersed in very high Reynolds number ($Re_\tau > 1000$) pressure-driven boundary layers.

On the shallow water channel vortex shedding is only present close to the interface, where the highly convective interface velocity overcomes the intrusion of incident coherent structures that interfere with shedding. Finally, in order to determine the degree of interference in the water column that could be caused by the existence of large scale vortices in the air

side interacting near the interface, a third simulation is conducted without any cylinder in the air domain. It is shown that the influence of large-scale vortices has little to no effect over the distribution of turbulent kinetic energy in the water column.

Spanwise array of square cylinders

On this scenario, a square cylinder immersed in the shallow water column and only partially immersed with a height-to-width ratio of 0.2 in the air side is studied in order to determine the degree of interference that obstacles immersed in the viscous region have on the air boundary layer formed in coupled system. In general, the vortical structures found around wall mounted cubes in experiment [33] are either not present at all or have an intermittent character. The latter properties render the blockage a 'roughness element' in a time averaged sense, given the low intensity of the anomalies caused in the mean flow. Furthermore, a POD on the resolved velocity fluctuations reveal that incident structures are shortened in the streamwise direction, while the intermittent horsehoe vortices lift $\langle v'v' \rangle$ energy produced at the interface into the outer region of the flow.

6.4 Future work

The increase intensities provided by the interface in air-water systems require better spatial accuracy, specially in the convective operator of the governing equations. A more complete study of turbulence on coupled canonical flows must dispense of the dispersive errors common in second-order accurate solution algorithms. For this matter, upwind high-order pseudo-spectral finite-difference operators should be sought.

In the present framework the simulation of flows affected by rotation, stratification, and other external non-solenoidal bodyforces are easy to conduct and readily available. Thus, flows that are commonplace in geophysical fluid dynamics like Ekman boundary layers, Langmuir circulations, and salinity stratification must be a next step in the use of the present code.

Phenomena like heat and humidity interface exchange, also of interest in GFD, may require further attention due to the rather high diffusivity of the scalars object of study in air-water systems; the scalars of interest in GFD and meteorology, like CO_2, have $200 < Sc < 600$ in most cases. Results obtained by the Author on coupled scalar transfer on Poiseuille-Poiseuille flows has proven to be excessively dissipative in the near-interface region in the water sub-domain for $Sc > 10$. Note that only DNS studies on coupled fluid flows with scalar transfer exist to date, to the Author's knowledge. Specifically, attention must be paid in the calculation of the SGS fluxes for the scalars which are subjected to a much higher

backscatter compared to the fluid flow counterpart. The implementation of deconvolution methods for the SGS fluxes in the scalar equation and pseudo-spectral schemes for the diffusive/convective terms of the governing equations may prove useful in this matter.

Appendices

Appendix A

Validation of the Navier-Stokes Solver

In Chapter 2 a series of validations were performed and analyzed, mainly to check the validity of the coupling made using *Picàrd Iterations*. Nevertheless, given that the algorithm that comprises the numerical integration of the Navier-Stokes equation was also changed a validation of such algorithm must be made.

The reason for such change, the addition of the pressure gradient term in the predictor equation, is clear: it gives a mathematically consistent description of the pressure and how the boundaries of the Poisson equation should be treated. Such consistency in the treatment of the pressure lead to a higher order of convergence in the solution and, in general, to more accurate results.

Thus, this chapter will present three archetype cases that will serve as validation for the algorithm proposed: (1) lid-driven cavity flow, (2) wall-bounded channel flow at $Re_\tau = 171$ and (3) $Re_\tau = 410$. The first two cases are well documented in literature, and no attempt to describe them thoroughly will be made. Anyway, basic results obtained from the tests will be confronted with those considered "classic" in the literature. However, the results obtained should be understood under the limits imposed by low-order spatial schemes, that is, of second-order finite volume operators acting as low-pass filters in addition to the LES model. Note that for the resolution of the SGS fluxes, the *Dynamic Smagorinsky* model described in Chapter 2 is used.

A.1 Lid-Driven Cavity Flow

Two-dimensional and three-dimensional lid-driven cavity flows have served as benchmark cases for CFD algorithms since a very long time [9], due to the simplicity of the domain and boundary conditions. Unfortunately, the same cannot be said for laboratory experiments: imposing a boundary condition that resembles the numerical moving lid proves to be difficult,

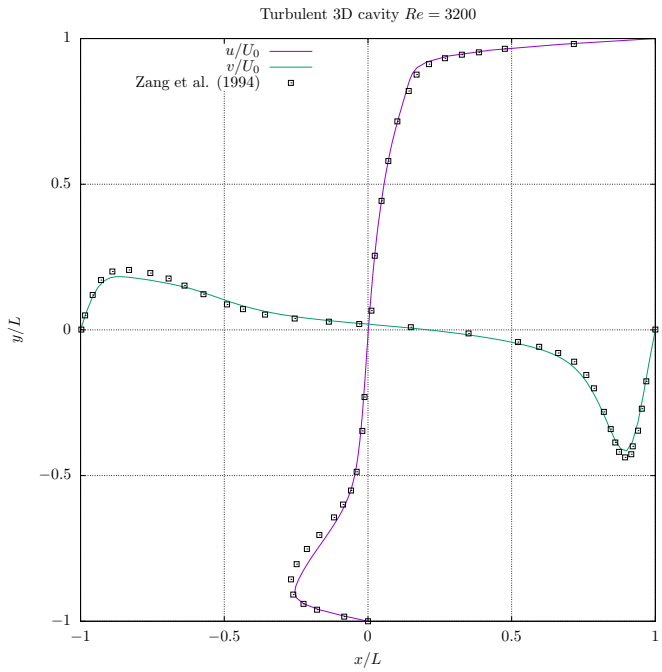

Figure A.1: Time-Averaged centerline velocity profiles on the midplane of the cavity. Solid line, present results; open symbols, taken from [52].

nevertheless experimental results exist [52].

A three-dimensional lid-driven cubic cavity of unitary dimensions is simulated, with a $Re = 3200$ in order to study the unsteady character of turbulence in such geometry. The grid is decomposed in $128 \times 128 \times 128$ degrees of freedom, and the boundaries are all walls except obviously on the direction of periodicity. In Figure A.1, the results obtained with the proposed algorithm are in good agreement with those found in Zang et al. [52]. One reason for the small differences can be due to the use of different *Smagorinsky* models: our model do not resolve the backscatter seen in the turbulent energy spectra present in cavity flows thus under-resolving the effects of near-wall instabilities present.

A.2 Wall-Bounded fully Developed Channel Flow

A large-eddy simulation of fully developed boundary layer turbulence was perfomed at a *Reynolds* number of $Re_\tau = 171$, based on viscous units. The simulation was run on a domain comprised of $80 \times 96 \times 64$ grid points in the streamwise, vertical, and spanwise directions. The size of such domain is $4\pi\delta \times \delta \times 2\pi\delta$, and the grid was stretched in the wall-normal direction with a hyperbolic tangent stretching function. Such stretching guarantees the resolution of turbulent fluctuations close to the no-slip boundaries. The results obtained and shown in Figure A.2a and A.2b are in good agreement with experimental data at least

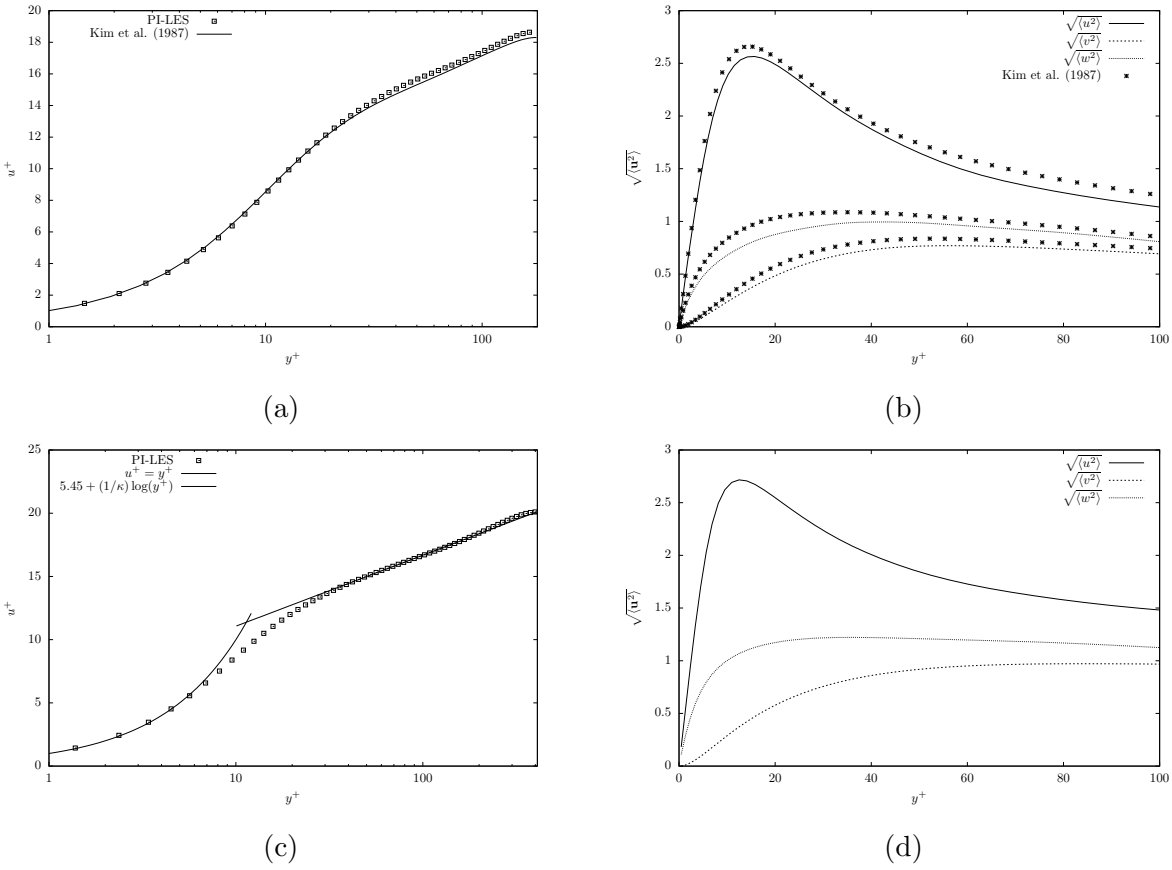

Figure A.2: Mean velocity and Reynolds shear stress profiles for (a)-(c) $Re_\tau = 180$ and (b)-(d) for $Re_\tau = 410$

for the first- and second-order statistical moments.

However, such a low *Reynolds* number does not strain much of the LES model itself since turbulent scales are small enough to make the overlap region of the boundary layer almost absent, thereby making the self-sustaining mechanisms of turbulence almost purely dissipative. By increasing the *Reynolds* number to $Re_\tau = 410$, the overlap and the wake region become apparent and the regeneration cycle responsible of generating backscatter is stronger. Anyway, results provided in Figures A.2c and A.2d fit well with empirical results.

Bibliography

[1] V. Armenio and U. Piomelli. A lagrangian mixed subgrid-scale model in generalized coordinates. *Flow, Turbulence and Combustion*, 65:51–81, 2000.

[2] V. Armenio and S. Sarkar. An investigation of stably stratified flows using large-eddy simulation. *J. Fluid Mech.*, 459:1–42, 2002.

[3] Kirk-Davidoff D. B. and Keith D. W. On the climate impact of surface roughness anomalies. *Am. Met. Soc.*, 65:2215–2235, 2008.

[4] R. J. Barthelemie, G. C. Larsen, S. T. Frandsen, L. Folkerts, K. Rados, S. C. Pryor, B. Lange, and G. Schepers. Comparison of wake model simulations with offshore wind turbine wake profiles measured by sodar. *J. Atmos. Oceanic Tech.*, 2006.

[5] K. H. Bech, N. Tillmark, P. H. Alfredsson, and H. I. Andersson. An investigation of turbulent plane couette flow at low reynolds numbers. *J. Fluid Mech.*, 286:291–325, 1995.

[6] R. F. Blackwelder and R. E. Kaplan. On the wall structure of the turbulent boundary layer. *J. Fluid Mech.*, 76, 2003.

[7] O. Botella. On the solution of the navier-stokes equations using chebyshev projection schemes with third-order accuracy in time. *Computers and Fluids*, 26:107, 1997.

[8] I. P. Castro, H. Cheng, and R. Reynolds. Turbulence over urban-type roughness: Deductions from wind-tunnel measurements. *Boundary-Layer Meteorology*, 118:109–131, 2006.

[9] A. J. Chorin. Numerical solution of the navier-stokes equations. *Math. Comp.*, 23: 341–362, 1968.

[10] A. A. Dimas and L. T. Fialkowski. Large-wave simulation (lws) of free-surface flows developing weak spilling breaking waves. *J. Comp. Phys.*, 159:172–196, 2000.

[11] J. Fröhlich and W. Rodi. Les of the flow around a circular cylinder of finite height. *Intl. J. Heat. Fluid Flow*, 25:537–548, 2004.

[12] M. Fulgosi, D. Lakehal, S. Banerjee, and V. De Angelis. Direct numerical simulation of turbulence in a sheared air-water flow with a deformable interface. *J. Fluid Mech.*, 482:319–345, 2003.

[13] V. Girault and P. A. Raviart. *Finite Element Methods for Navier-Stokes Equations. Theory and Algorithms*. Springer-Verlag, Berlin, 1986.

[14] P. M. Gresho and R. L. Sani. On pressure boundary conditions for the incompressible navier-stokes equations. *Intl. J. Num. Meth. Fluid*, 7:1111–1145, 1987.

[15] J. L. Guermond and J. Shen. Velocity-correction projection methods for incompressible flows. *SIAM J. Num. Anal.*, 41(1):112–134, 2003.

[16] X. Guo and L. Shen. Numerical study of the effect of surface waves on turbulence underneath. part 1. mean flow and turbulence vorticity. *J. Fluid Mech.*, 733:558–587, 2013.

[17] R. Higbie. The rate of absorbtion of a pure gas into a still liquid during short periods of exposure. *Trans. AIChE*, 31:365–388, 1935.

[18] R. Hosker. *Flow and diffusion near obstacles*. United States Department of Energy, 1984.

[19] J. Jeong, F. Hussain, W. Schoppa, and J. Kim. Coherent structures near the wall in a turbulent channel flow. *J. Fluid. Mech.*, 332:185–214, 1996.

[20] J. Kim, P. Moin, and R. Moser. Turbulence statistics in fully developed channel flow at low reynolds number. *J. Fluid. Mech.*, 177:133–166, 1987.

[21] R. Komori, Kurose. R., K. Iwano, T. Ukai, and N. Suzuki. Direct numerical simulation of three-dimensional open-channel flow with zero-shear gas-liquid interface. *Journal of Turbulence*, 11(32), 1996.

[22] S. Komori, R. Nagaosa, Y. Murakami, S. Chiba, I. Ishii, and K. Kuwahara. Direct numerical simulation of three-dimensional open-channel flow with zero-shear gas-liquid interface. *Phys. Fluids*, 5(115), 1993.

[23] A. G. Kravchenko, P. Moin, and R. Moser. Zonal embedded grids for numerical simulations of wall-bounded turbulent flows. *J. Comp. Phys.*, 127:412–423, 1996.

[24] R. Kurose., N. Takagaki, A. Kimura, and R. Komori. Direct numerical simulation of turbulent heat transfer across a sheared wind driven gas liquid interface. *J. Fluid Mech.*, 804:646–687, 1996.

[25] K. Lam and S. Banerjee. On the condition of streak formation in bounded turbulent flow. *Phys. Fluids*, 4(306), 1992.

[26] M. J. Lee and J. Kim. The strucuture of turbulence in a simulated plane couette flow, 1991.

[27] P. Lenaers, Q. Li, G. Brethouwer, P. Schlatter, and R. Orlu. Rare backflow and extreme wall normal velocity fluctuations in near wall turbulence. *Phys. Fluids*, 24, 2012.

[28] S. Liu, A. Kermani, L. Shen, and D. K. P. Yue. Investigation of coupled air-water turbulent boundary layers using direct numerical simulations. *Phys. Fluids*, 21, 2009.

[29] P. Lombardi, V. De Angelis, and S. Banerjee. Direct numerical simulation of near-interface turbulence in coupled gas-liquid flow. *Phys. Fluids*, 8(6):1643–1665, 1996.

[30] S. Lopez Castano, V. Armenio, and B. Geurts. An investigation of strong backflow events at the interface of air-water systems using large-eddy simulation. (to be published in J. Turbulence), 2018.

[31] R. W. MacDonald. Modelling the mean velocity profile in the urban canopy layer. *Boundary-Layer Meteorology*, 97:25–45, 2000.

[32] M. Manna and A. Vacca. Scaling properties of turbulent pipe flow at low reynolds number. *Comput. Fluids*, 30, 2001.

[33] R. Martinuzzi and C. Tropea. The flow around surface-mounted, prismatic obstacles placed in a fully developed channel flow. *J. Fluid Eng.*, 115:85–92, 1993.

[34] P. Moin and J. Kim. The structure of the vorticity field in turbulent channel flow. part 1. analysis of instantaneous fields and statistical correlations. *J. Fluid Mech.*, 286:155–, 1985.

[35] G. Pathikonda and K. T. Christiensen. Structure of turbulent channel flow perturbed by a wall-mounted cylindrical element. *AIAA Journal*, 53(5), 2015.

[36] S. B. Pope. *Turbulent Flows*. Cambridge University Press, 2000.

[37] F. Porte-Agel, H. Lu, and Y.-T. J. Wu. Interaction between large wind farms and the atmospheric boundary layer. International Congress of Theoretical and Applied Mechanics, 23th Edition, 2014.

[38] F. Roman, E. Napoli, B. Milici, and V. Armenio. An improved immersed boundary method for curvilinear grids. *Computers & fluids*, 38:1510–1527, 2009.

[39] M. D. Ryan, C. Ortiz-Dueñas, and E. K. Longmire. Effects of simple wall-mounted cylinder arrangements on a turbulent boundary layer. *AIAA Journal*, 49(10), 2011.

[40] P. Sagaut. *Large Eddy Simulation for Incompressible Flows: an Introduction*. Springer-Verlag, 2006.

[41] W. Schoppa and F. Hussain. Coherent structure dynamics in near-wall turbulence. *Fluid Dyn. Research*, 26:119–139, 2000.

[42] P.P. Sullivan, J. B. Edson, T. Hristov, and J. C. McWilliams. Large-eddy simulations and observations of atmospheric marine boundary layers above nonequilibrium surface waves. *J. Atmos. Sci.*, 65:1225–1245, 2008.

[43] N. Takagaki, R. Kurose, A. Kimura, and S. Komori. Effect of schmidt number on mass transfer across a sheared gas-liquid interface in a wind-driven turbulence. Technical report, University of Tokio, Japan, 2016.

[44] R. Temam. Une methode d'approximation de la solution des equations de navier-stokes. *Bull. Soc. Math. France*, 96:115–152, 1968.

[45] C. D. Tomkins. *The structure of Turbulence over Smooth and Rough Walls*. PhD thesis, University of Illinois at Urbana-Champaign, Urbana, IL, 2001.

[46] D. E. Turney and S. Banerjee. Air water gas transfer and near-surface motions. *J. Fluid Mech.*, 733:588–624, 2013.

[47] B. J. Vanderwende, B. Kosovic, J. K. Lundquist, and J. D. Mirocha. Simulationg effects of a wind-turbine array using les and rans. *J. Adv. Mod. Earth Sci.*, 8(3), 2016.

[48] W. W. Willmarth and S. S. Lu. Structure of the reynolds stress near the wall. *J. Fluid. Mech.*, 55(65–92), 1972.

[49] N. N. Yanenko. The method of fractional steps. the solution of problems of mathematical physics in several variables. 1966.

[50] D. Yang, C. Meneveau, and L. Shen. Large-eddy simulation of offshore wind farms. *Phys. Fluids*, 27, 2014.

[51] S. G. Yiantsios and B. G. Higgins. Linear stability of plane poiseuille flow of two superposed fluids. *Phys. Fluids*, 31(11):3225–3238, 1988.

[52] Y. Zang, R. L. Street, and J. R. Koseff. A non-staggered grid, fractional step method for time-dependent incompressible navier-stokes equations in curvilinear coordinates. *J. Comp. Phys.*, 114:18–33, 1994.